SEARCH FOR HIGH-MASS DIELECTRON RESONANCES WITH THE ATLAS DETECTOR

By

Sarah Heim

A DISSERTATION

Submitted to
Michigan State University
in partial fulfillment of the requirements
for the degree of

DOCTOR OF PHILOSOPHY

Physics

2012

ABSTRACT

SEARCH FOR HIGH-MASS DIELECTRON RESONANCES WITH THE ATLAS DETECTOR

By

Sarah Heim

This thesis describes a search for new heavy particles decaying into electron-positron pairs. The search utilizes 1.08 fb^{-1} of proton-proton collisions at a center-of-mass energy of $\sqrt{s} = 7$ TeV, produced in 2011 by the Large Hadron Collider and recorded with the ATLAS detector at the CERN laboratory in Switzerland. The reconstructed dielectron invariant mass spectrum is compared to Standard Model expectations. Since no significant excess is found, upper limits on the cross-section times branching ratio of Z' bosons and Randall-Sundrum gravitons are determined at the 95% confidence level using a Bayesian approach. These limits are combined with limits obtained by a parallel analysis in the muon channel and converted into lower limits on the masses of the Sequential Standard Model Z'_{SSM} boson (1.88 TeV), E_6 Z' bosons (1.54 - 1.68 TeV), as well as the Randall-Sundrum graviton (1.67 TeV for $k/\bar{M}_{Pl} = 0.1$).

To my parents, Gisela and Roland Heim.
And to my sister Julia.

ACKNOWLEDGMENT

First of all, I want to thank my advisor Reinhard Schwienhorst who taught me how to do high energy physics and who was always available to talk and answer questions with amazing patience.

Thanks to Wojtek Fedorko for teaching me about likelihoods, pseudo-experiments, and the proper way of searching for new physics.

Thanks to the rest of the MSU High Energy Physics group, especially to Jenny Holzbauer, her accelerator husband Jeremiah, and James Koll for sharing their graduate student wisdom with me and to Reiner Hauser whose knowledge about libraries, links and compilers saved me hours of frustration. Not to forget Yuri Ermoline for helping me fix (among other things) my bike, my laptop, and my glasses and Tom Rockwell, who kept the Tier3 alive.

Thanks to my committee, Professors Mahanti, Pope, Pratt, and Repko, for accepting this job and a big thank you to Brenda Wenzlick and Debbie Barratt for helping me through the bureaucratic jungle. I would have been quite desperate without you!

I also want to thank Bernd Stelzer and Oliver Stelzer-Chilton for sharing their statistical and Z' knowledge with me and Ashutosh Kotwal for his theory insight.

Thanks to Simon Viel for being a great co-analyzer, co-convener, and co-hiker. Also to Dan Hayden for great cooperation and the unskimmed 1 fb^{-1} cutflow.

I would also like to thank Amanda Smith for sharing her apartment, table, and cat with me and for introducing me to American life.

And, of course, much love to Aaron Adair, who I thought of while writing this thesis.

TABLE OF CONTENTS

LIST OF TABLES

LIST OF FIGURES

Chapter 1

Introduction

For a long time it has been a human endeavor to understand what the universe is made of and why it looks the way it does. Today we know that the matter we find on earth consists of atoms: nuclei of protons and neutrons surrounded by electrons. Protons and neutrons are not fundamental particles but contain quarks and gluons. The quarks and electrons that make up ordinary matter have heavier relatives which, soon after they are produced, decay into lighter particles. Elementary particles can interact with each other through exchange particles like the photon. For all particle types there exist antiparticles, with the same masses but opposite charges (some particles like the photon are their own antiparticles).

The goal of particle physics is to understand what the elementary particles are and how they interact with each other. During the 20th century, the Standard Model of Particle Physics (SM) was developed, a very successful theory describing fundamental particles and their interactions. The SM has not only been confirmed in many precision measurements, but has also been able to predict observations like the discovery of the Z boson in 1983 [1, 2]. However, the SM cannot describe the subatomic world completely and has several

shortcomings: Among other things it does not include gravitation and it cannot explain why there is more matter than antimatter in the universe.

One of the biggest quests in particle physics today is therefore to understand what lies beyond the SM. This is done experimentally by searching for particle interactions that are not predicted by the SM. As the SM has been under scrutiny for decades, the new interactions are expected to be quite rare or only possible when the particles interacting with each other have very high energies. The LHC (Large Hadron Collider) at the CERN (Conseil Européen pour la Recherche Nucléaire) laboratory in Geneva, Switzerland, collides particles with the highest energies ever achieved in a particle accelerator and offers the unique opportunity to directly search for physics inaccessible anywhere else. Large particle detectors like ATLAS (A Toroidal LHC ApparatuS) are required to detect, filter and record the outcome of these interactions. Their size is determined by the need to reconstruct the properties of the produced particles.

This thesis describes a search for a heavy (> 130 GeV), electrically neutral particle which is produced in proton-proton collisions at the LHC and decays into an electron and a positron[1]. We select collision events resulting in two electrons because such a heavy particle decays too fast to be observed and the ATLAS detector can only record its decay products. The invariant mass of the two electrons corresponds to the mass of the new particle and its unique signature is a narrow resonance peak in the dielectron mass spectrum. The position of this peak depends on the mass of the new particle, and its size on the production cross-section as well as the branching ratio with which it decays into electrons. A high-mass dielectron resonance is not predicted by the SM, but by some of its extensions like the E_6 model [3, 4],

[1]From here on, "electron" will be used representatively for both electrons and positrons.

which is one of the Grand Unified Theory models, suggesting that all fundamental forces (except for gravity) are the same at very high energies. Another example is the Randall-Sundrum model [5], which proposes the graviton as the exchange particle for gravitation, and which suggests the existence of at least one extra dimension. Finding the graviton or another new exchange particle would significantly contribute to our understanding of the fundamental forces. If we do not see a resonance, we can exclude at least parts of the proposed extensions to the SM.

Besides this thesis, this analysis is published in [6]. The thesis is organized in 8 chapters:

1. Introduction.

2. This chapter describes the SM, focusing on the electroweak interaction. Successes and shortcomings of the SM are discussed, as well as potential extensions that could produce a high-mass dielectron resonance.

3. The LHC as well as the ATLAS detector are explained, with emphasis on the parts necessary to find electron pairs: Tracks of electron candidates are recorded in the Inner Detector and their energy is measured in the electromagnetic calorimeter.

4. Dedicated triggers filter events containing electron candidates whose energy and direction need to be reconstructed. Identification cuts increase the probability of an electron candidate to be a real electron. Furthermore, the specific properties of electrons that have high energies are described.

5. This chapter lists the simulated samples for signal and background processes used to compare the data to the SM background plus potential signal, and the corrections that need to be applied to the simulation to improve the modeling.

6. The event selection and the comparison between data and SM expectations for the dielectron invariant mass distribution and other kinematic distributions are shown. The estimate of QCD multijet production, which is obtained from data, is also described.

7. This chapter outlines the search for significant excesses in the dielectron invariant mass distribution in data as compared to the SM background. Since no significant excess is found, the Bayesian procedure for setting 95% confidence level limits on the cross-section times branching ratio and the signal mass is described and the resulting limits are shown.

8. Conclusion.

Chapter 2

Standard Model of Particle Physics and beyond

In this chapter, the SM is discussed, as well as possible extensions that could result in high-mass dielectron resonances. In spite of spectacular successes describing and predicting interactions between fundamental particles, the SM in its current form is considered to be incomplete. In order to understand observations not explained by the SM, many models have been suggested, some of which predict a new heavy particle decaying into two electrons. Examples are models that allow the unification of fundamental forces at high energies as well as models predicting extra dimensions.

2.1 Standard Model of Particle Physics

The SM describes almost every phenomenon observed in the subatomic world. It contains the elementary particles of matter - quarks and leptons, which are fermions - and describes the interactions between them as exchanges of force-carrying bosons. The $W^+/W^-$and Z

bosons as well as the photon (γ) mediate the electroweak force, while gluons (g) carry the strong force. The SM also contains a Higgs field generating the masses of the fundamental particles. The corresponding Higgs boson has not been found yet.

While the SM is incomplete (compare Sec. 2.2), it fits most of the available data to very high precision and can be used to make reliable predictions. Examples of past successes of the SM are the prediction of the existence and the properties of the weak bosons $W^+/W^-$and Z. These were discovered [7, 8, 1, 2] at the Super Proton Synchroton, CERN, more than 10 years after the formulation of the electroweak theory [9, 10, 11].

In the following, the fundamental principles and building blocks of the SM are described, followed by a discussion of electroweak interactions with a focus on the Drell-Yan process (DY, $q\bar{q} \rightarrow Z/\gamma* \rightarrow e^+e^-$). Not only is the DY process the largest background in this analysis, but many proposed new interactions leading to high-mass dielectron resonances have very similar structures and could actually modify it, as shown in Sec. 2.2.3.

2.1.1 Symmetries and fields

The SM is a gauge theory in which the fundamental particles are represented by quantized fields. In gauge theories, the Lagrangian is invariant with respect to certain local transformations, i.e. changes of the participating fields that can be different at any point in space-time. In contrast to this, global transformations like translations change a field the same way at every point. Gauge theories are very powerful tools because they are renormalizable [12]. This means they provide a way to cancel divergences, infinities that may arise in the calculation of physical quantities. Furthermore, every gauge invariance leads to a conserved quantity [13] as well as a number of force carriers, called gauge bosons, which only act on fields carrying

some of the conserved charge. This can easily be seen by looking at the electromagnetic interaction, where the need to make the Lagrangian invariant with respect to phase changes of the electron field leads to the introduction of an additional vector field, the photon. This has to be massless since a photon mass term would not be gauge invariant. The conserved quantity in this example is the electromagnetic charge.

Transformation invariances can be described by symmetry groups, whose members are the generators of the transformation, e.g. unitary matrices in case of rotations. The SM is described by the following combination of gauge symmetry groups:

$$\mathrm{SU}(3)_C \times \mathrm{SU}(2)_L \times \mathrm{U}(1)_Y \tag{2.1}$$

Here, U(1) corresponds to a unitary group of degree 1. It has one generator and describes the invariance of the Lagrangian when the fields are multiplied by any given phase factor. SU(2) is a special unitary group of degree 2. It has three generators, which can be represented by 2×2 matrices whose determinant is 1. $\mathrm{SU}(2)_L \times \mathrm{U}(1)_Y$ corresponds to the electroweak interaction. According to the number of generators, $\mathrm{U}(1)_Y$ contributes one gauge boson, called B, while $\mathrm{SU}(2)_L$ has three, W^0, W^1, W^2. The conserved quantity in $\mathrm{U}(1)_Y$ is the weak hypercharge Y, in $\mathrm{SU}(2)_L$ it is the weak isospin $\vec{I}$. These quantities are not independent; their relation to the electromagnetic charge Q is $Y = Q - I^3$, where I^3 is the third component of the weak isospin [12]. The electroweak interaction is chiral, which means particles are treated differently depending on whether they are left- or right-handed: Right-handed particles and left-handed antiparticles do not interact with the $\mathrm{SU}(2)_L$ gauge bosons. Spontaneous Symmetry Breaking (SSB, see Sec 2.1.2) results in an unbroken group $\mathrm{U}(1)_Q$, whose gauge boson is a massless photon and consists of a linear combination of B

and W^0. The photon interacts with particles that have electromagnetic charge. The orthogonal linear combination of B and W^0 produces a neutral Z boson, whose mass has been measured to be 91.19 GeV [14]. The remaining force carriers of the weak interaction are the charged W^+ and W^- bosons, which correspond to linear combinations of W^1 and W^2. Their mass has been experimentally determined to be 80.40 GeV [14].

$\mathrm{SU}(3)_C$ describes the strong interaction. Its generators can be represented by 3×3 matrices and correspond to eight massless gluons. The conserved quantity is the color charge. The strong force only acts on particles carrying color; these are the gluons themselves as well as the six flavors of quarks.

Table 2.1 shows the fermion fields of the SM, including their charges. The table for the antiparticles looks identical, except for a sign-flip in the charges. Each quark can have one of three color indices. There are three generations of quarks and leptons. The right-handed fermions are $\mathrm{SU}(2)_L$ singlets, which means they do not interact with the W bosons. The leptons do not have color charge, thus they do not participate in the strong interaction. Likewise, the neutrinos are electromagnetically neutral, so they cannot interact with photons directly. Right-handed neutrinos have never been observed; however, oscillations have been detected between the three generations of neutrinos, which enforce the inclusion of right-handed neutrinos as an extension to the SM (compare Sec. 2.2.1).

2.1.2 Lagrangian

This section describes the Lagrangian density of the SM with focus on the neutral electroweak interaction, as this part could be modified by the new physics we search for in this analysis. A short description of SSB is given, and the electroweak Lagrangian is shown before and

	Generation			Charges			
	I	II	III	Color?	I^3	Y	Q
Quarks	$\begin{pmatrix} u \\ d \end{pmatrix}_L$	$\begin{pmatrix} c \\ s \end{pmatrix}_L$	$\begin{pmatrix} t \\ b \end{pmatrix}_L$	Yes	1/2	1/6	2/3
				Yes	-1/2	1/6	-1/3
	u_R	c_R	t_R	Yes	0	2/3	2/3
	d_R	s_R	b_R	Yes	0	-1/3	-1/3
Leptons	$\begin{pmatrix} \nu_e \\ e \end{pmatrix}_L$	$\begin{pmatrix} \nu_\mu \\ \mu \end{pmatrix}_L$	$\begin{pmatrix} \nu_\tau \\ \tau \end{pmatrix}_L$	No	1/2	-1/2	0
				No	-1/2	-1/2	-1
	e_R	μ_R	τ_R	No	0	-1	-1

Table 2.1: Fermion fields in the SM and their charges [14]. Each quark can have one of three color indices.

after including SSB.

The Lagrangian describes the dynamics of fields and their interactions. It is defined as

$$L = T - V, \tag{2.2}$$

where T is the kinetic energy and V is the potential energy. In field theory, the Lagrangian density $\mathcal{L}$ is used instead of the Lagrangian, with $L = \int \mathcal{L}\, \mathrm{d}^3x$. A Lagrangian in field theory can contain terms for the free propagation of particles, their masses, and their interaction with other particles as well as with themselves.

The Lagrangian density of the SM can be split into four parts [12]:

$$\mathcal{L} = \mathcal{L}_{Fermion} + \mathcal{L}_{Gauge} + \mathcal{L}_{Higgs} + \mathcal{L}_{Yukawa} \tag{2.3}$$

$\mathcal{L}_{Fermion}$ describes the kinetic energy of the fermions as well as interactions of the fermions with the gauge bosons. If the weak eigenstates of the fermions are described in 4-component vectors F, the part of the Lagrangian density that describes the free motion of the fermions

can be written as:

$$\mathcal{L}_0 = \bar{F}(x)(i\partial\!\!\!/ - m)F(x), \qquad \partial\!\!\!/ = \gamma^\mu \frac{\partial}{\partial x^\mu} = \gamma^\mu \partial_\mu, \tag{2.4}$$

where γ^μ is the set of Dirac matrices and the Dirac adjoint is defined as $\bar{F} = F^\dagger \gamma^0$. If the fermion field F is written as $F = F_L + F_R$, where $F_{L(R)}$ corresponds to left-(right-)handed fermions, $F_L = F\ (1\ -\ \gamma^5)/2$ and $F_R = F\ (1\ +\ \gamma^5)/2$, it becomes clear that only mass terms survive that contain a left- and a right-handed field, since $\bar{F}_L F_L = \bar{F}_R F_R = 0$.

The Lagrangian density for the electroweak sector, $\mathcal{L}_{EW}$, can be written as:

$$\mathcal{L}_{EW} = \sum_f \bar{F}_{Lf} i D\!\!\!/ F_{Lf} + \bar{F}_{Rf} i D\!\!\!/ F_{Rf}. \tag{2.5}$$

D is the derivative in the free Lagrangian density, which is made gauge invariant with respect to $\mathrm{SU(2)}_L$ and $\mathrm{U(1)}_Y$ by adding the fields W^i_μ and B_μ:

$$\begin{aligned} D_\mu F_{Lf} &= (\partial_\mu + ig\vec{I}\cdot\vec{W}_\mu + ig' Y_{Lf} B_\mu) F_{Lf} \\ D_\mu F_{Rf} &= (\partial_\mu + ig' Y_{Rf} B_\mu) F_{Rf}. \end{aligned} \tag{2.6}$$

Here, g and g' are the gauge coupling constants for $\mathrm{SU(2)}_L$ and $\mathrm{U(1)}_Y$ respectively. $\vec{I}$ corresponds to the weak isospin, while Y is the weak hypercharge. There is no mass term since a term mixing left- and right-handed fields would break the gauge symmetry.

$\mathcal{L}_{Gauge}$ contains the kinetic terms of the gauge bosons B, W^i and g as well as the self-interaction terms for all gauge bosons but B, which does not self-interact. The Lagrangian density for the Higgs field $\mathcal{L}_{Higgs}$ (Eq. 2.7) consists of the kinetic energy and the self-

interaction of the Higgs boson as well as terms for interactions between the Higgs and the gauge bosons. The Yukawa term $\mathcal{L}_{Yukawa}$ describes the couplings between the Higgs boson and the fermions, giving the latter their masses.

Like for fermions, explicit mass terms for gauge bosons violate the gauge invariance. However, we know that the weak gauge bosons have mass, thus the gauge symmetry of the electroweak interaction must be broken. In the SM, this happens through SSB. Charges are still conserved, since SSB does not introduce any explicit symmetry breaking. The Lagrangian density of the Higgs field ϕ preserves the gauge symmetry:

$$\mathcal{L}_{Higgs} = (D^{\mu}\phi)^{\dagger}(D_{\mu}\phi) - V(\phi), \tag{2.7}$$

where ϕ is the complex scalar Higgs field, and

$$D_{\mu}\phi = (\partial_{\mu} + ig\vec{I}\cdot\vec{W}_{\mu} + \frac{ig'}{2}B\mu)\phi. \tag{2.8}$$

$V(\phi)$ needs to be gauge invariant with respect to $\mathrm{SU}(2)_L \times \mathrm{U}(1)_Y$ as well, and has the form

$$V(\phi) = \mu^2\phi^{\dagger}\phi + \lambda(\phi^{\dagger}\phi)^2. \tag{2.9}$$

The ground state of ϕ can be found by looking for the minimum of $V(\phi)$, and can be written as $\phi_0 = \binom{0}{v}$, where $v = \sqrt{-\mu^2/\lambda}$. If $\mu^2 < 0$, ϕ has a non-zero vacuum expectation value and ϕ can be written as $\phi = \phi_0 + \phi'$, where ϕ' is a field with a zero vacuum expectation value. In terms of ϕ', the $\mathrm{SU}(2)_L \times \mathrm{U}(1)_Y$ symmetry in Eq. 2.7 is broken and mass terms for the weak bosons emerge. These are now a mixture of the original gauge bosons. The

electroweak mixing angle θ_W is defined as

$$\tan\theta_W = \frac{g'}{g}. \tag{2.10}$$

The Z boson can be expressed in terms of this angle and the gauge bosons B and W^3:

$$Z_\mu = -B_\mu \cos\theta_W + W^3_\mu \sin\theta_W. \tag{2.11}$$

The photon is the orthogonal linear combination:

$$A_\mu = B_\mu \cos\theta_W + W^3_\mu \sin\theta_W. \tag{2.12}$$

The couplings g and g' are not independent, instead they are related to the electromagnetic coupling e and the neutral weak coupling g_Z by

$$e = g\ \sin\theta_W, \quad g_Z = \frac{g}{\cos\theta_W} = \frac{g'}{\sin\theta_W} = \frac{e}{\sin\theta_W \cos\theta_W}. \tag{2.13}$$

Now the Lagrangian density for the neutral electroweak interaction of fermions can be written down. It can be obtained by replacing B_μ and W^3_μ with A_μ and Z_μ according to Eq. 2.11 and 2.12 in Eq. 2.5:

$$\begin{aligned}\mathcal{L}_{EW,n} = &-e\sum_f \bar{\psi}_f \gamma^\mu Q_f \psi_f A_\mu \\ &- g_Z \sum_f [\bar{\psi}_{Lf}\gamma^\mu (I^3_f - Q_f \sin^2\theta_W)\psi_{Lf} Z_\mu + \bar{\psi}_{Rf}\gamma^\mu(-Q_f \sin^2\theta_W)\psi_{Rf} Z_\mu].\end{aligned} \tag{2.14}$$

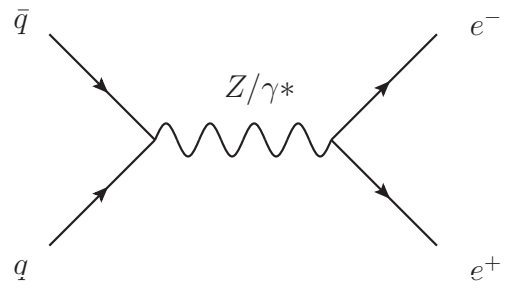

Figure 2.1: Feynman diagram of the DY process.

The first line describes the electromagnetic interaction. Its strength is independent of the chirality of the leptons and depends on the coupling constant e and the fermion charge Q_f. This part of the electroweak Lagrangian can also be derived directly from the requirement of gauge invariance of the Lagrangian with respect to phase changes in the electron fields. The second line describes the neutral weak interaction, which is chiral, having a different strength for left- and right-handed fermions. The Lagrangian density is now written in terms of mass eigenstates ψ, instead of weak eigenstates F.

Sec. 2.2 shows how the electroweak Lagrangian is modified by additional neutral Z' gauge bosons.

2.1.3 Feynman diagrams and cross-section calculations

Feynman diagrams simplify the calculation of the probability that particles interact with each other in a certain way. The diagrams help visualize the initial, intermediate, and final states, and they help determine the importance of different sub-processes.

The Feynman diagram in Fig. 2.1 shows two of the possible ways in which two quarks can annihilate: The production of a Z boson or a photon and the subsequent decays of the intermediate particle into two electrons. In this process, countless additional interactions are possible, for example radiation of gluons and photons as well as particle loops. These sub-

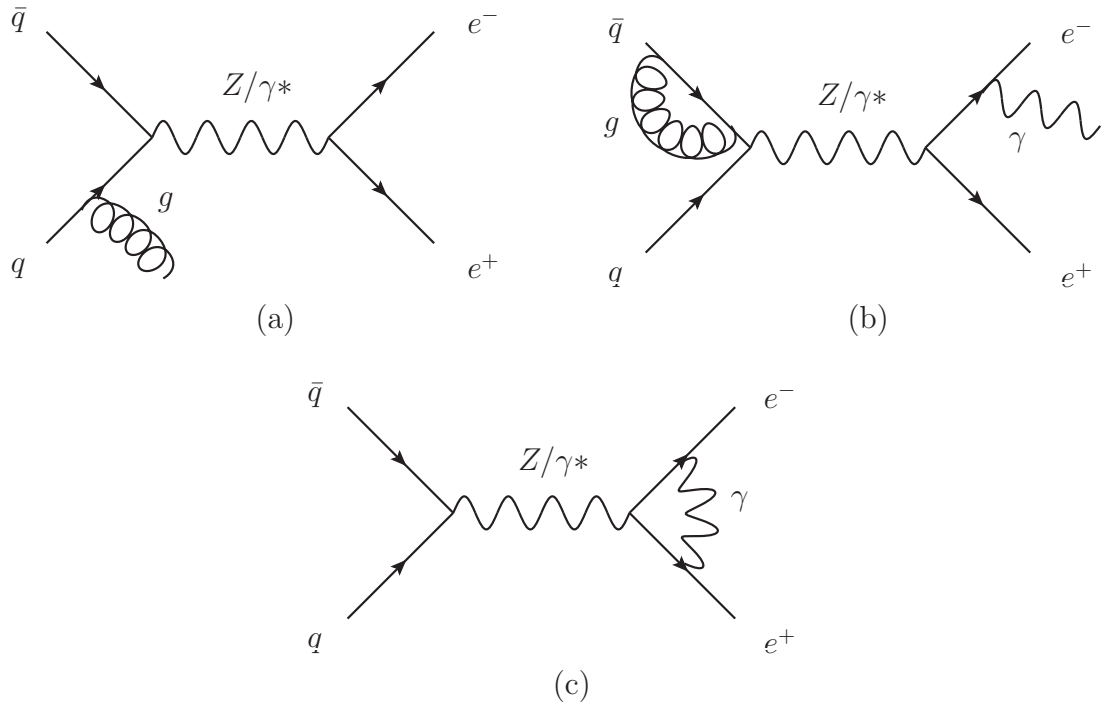

Figure 2.2: Strong and electroweak higher order contributions to the DY process: Radiation of a gluon in the initial state (a), a gluon loop in the initial state and the emittance of a photon in the final state (b), and a photon loop in the final state (c).

processes can be illustrated in different Feynman diagrams (see Fig. 2.2 for a few examples).

Since the probability amplitude of every particle interaction is proportional to the coupling constant, the less particle-particle vertices a Feynman diagram for a given sub-process has, the more likely it is. Furthermore, higher order contributions involving gluons are larger than those involving photons because the strong interaction has larger couplings than the EW interaction. The Feynman diagram in Fig. 2.1 illustrates the dominant, leading order (LO) contribution to the $q\bar{q} \to e^+e^-X$ process (X denotes additional radiation). In this sense, Feynman diagrams are tools of perturbation theory; they allow to split up the infinite number of possible interactions in a process into different orders of probability.

Using the corresponding diagrams, one can in principle calculate cross-sections up to a required precision, however, for higher order processes it is necessary to introduce normaliza-

tion and factorization scales. These are artificial cut-offs removing infinities which can occur if not all orders of the perturbation series are taken into account. Furthermore, perturbation theory can only be applied as long as the coupling constants are small. This is the case for electroweak interactions, but not necessarily for interactions involving the strong force. Since we are looking at dielectron final states, strong interactions can only happen in the initial state. The factorization theorem [15] states that perturbation theory still applies for the hard scattering process itself, because the quarks are asymptotically free at high energies.

The Feynman rules give a prescription on how to turn Feynman diagrams into matrix elements, which correspond to probability amplitudes of the interactions. These rules are obtained from the Lagrangian [16]. In order to calculate the matrix element, the 4-momenta of the incoming and outcoming particles must be known. If they are defined for the incoming particles, the inclusive cross-section is proportional to the absolute square of the matrix element, integrated over all possible momenta of the final state particles. However, at hadron colliders like the LHC which collides protons, the reacting quarks carry an unknown fraction of the proton momenta. In order to calculate cross-sections, one usually integrates over all possible incoming quark momenta, using probability functions for the momentum fraction of the quarks (parton distribution functions, PDFs) which are obtained from fits to data [17, 18, 19]. Since the quarks in the protons are bound by the strong interaction, the PDFs include non-perturbative effects, and can account for higher order QCD corrections in the initial state.

2.1.4 Drell-Yan process

In the DY process, a quark and an antiquark produce a photon or a Z boson, which then decays into quarks or leptons. The final state considered in this analysis is the dielectron decay ($q\bar{q} \to Z/\gamma* \to e^+e^-$). Figure 2.1 shows the Feynman diagram of the LO DY process.

The DY process is the most important SM background to the search for new physics with dielectron final states. Its electroweak structure serves as a model for interactions with new heavy neutral gauge bosons. The inclusion of new gauge bosons in the electroweak Lagrangian does not necessarily lead to a simple cross-section addition of the different processes, but can cause shifts in the peak mass of the Z boson and its couplings to the fermions (mass mixing, [20]) as well as cross-section enhancement/suppression due to positive/negative interference. Neglecting mass mixing, we write down the electroweak Lagrangian and the matrix element of the DY and the new Z' boson in Sec. 2.2 (Eq. 2.22, 2.23). In this section, the components of the pure DY matrix element are explained.

In order to write down the LO equation for the DY matrix element [21], the following 4-momenta (p, k) and helicities (σ, τ) are assigned to the incoming and outgoing particles:

$$q(p_1, \sigma_1) + \bar{q}(p_2, \sigma_2) \to e^-(k_1, \tau_1) + e^+(k_2, \tau_2). \tag{2.15}$$

The Mandelstam variables are defined as

$$\hat{s} = (p_1 + p_2)^2,\ \hat{t} = (p_1 - k_1)^2,\ \hat{u} = (p_1 - k_2)^2. \tag{2.16}$$

Here, $\hat{s}$ corresponds to the center-of-mass (CM) energy of the collision and is, at LO, equal to the invariant mass of the two outgoing electrons $(k_1 + k_2)^2$.

Applying the Feynman rules [16], one can write down the chirality dependent matrix element for the full DY process at LO as [21]:

$$\mathcal{M}^{\sigma,\tau}(\hat{s},\hat{t},\hat{u}) = \frac{e}{\hat{s}} \sum_{V=\gamma,Z} c^{\sigma}_{qqV}\ c^{\tau}_{eeV}\ P_V(\hat{s})\ M^{\sigma\tau}. \tag{2.17}$$

For the weak interaction, the couplings between fermions f and exchange bosons depend on the chiralities $\sigma = \sigma_1 = -\sigma_2$ and $\tau = \tau_1 = -\tau_2$. The couplings c are taken directly from the electroweak Lagrangian (Eq. 2.14) and can be written as:

$$c^{L/R}_{ff\gamma} = -eQ_f, \quad c^{L}_{ffZ} = e\frac{I^3_f - \sin^2\theta_W Q_f}{\sin\theta_W \cos\theta_W}, \quad c^{R}_{ffZ} = -eQ_f\frac{\sin\theta_W}{\cos\theta_W}. \tag{2.18}$$

The propagators for the two exchange particles are:

$$P_\gamma = 1, \quad P_Z = \frac{\hat{s}}{(\hat{s} - M^2_Z + i\hat{s}\Gamma_Z/M_Z)}. \tag{2.19}$$

Since the Z boson is not a stable particle, its width Γ_Z is inserted into the Z boson propagator. This is done in the "running width" scheme, which illustrates the change of the width with different CM energies.

The "standard" matrix element $M^{\sigma\tau}$ depends on the polarization of the incoming and outgoing fermions. Two different chirality combinations are allowed,

$$M^{LL} = M^{RR} = 2\hat{u}, \quad M^{LR} = M^{RL} = 2\hat{t}. \tag{2.20}$$

2.2 Beyond the Standard Model

The SM is quite successful in describing the interactions of fundamental particles throughout the experimentally available energy range. However, there are many missing pieces, observations not explained by the SM or even contradicting its predictions. Furthermore, there are theoretical concerns and arguments which suggest that the SM can only be part of a larger theoretical framework.

2.2.1 Limitations of the Standard Model

Some observations not covered by the SM are the matter-antimatter asymmetry in the universe without which there would be no stable matter, as well as the existence of dark matter. The SM predicts neutrinos to be massless, but the observation of neutrino oscillations requires neutrinos to have mass [22, 23, 24, 25]. The latter is fortunately quite easy to incorporate in the SM by adding right-handed neutrinos. The largest discrepancy between theory and observation can be found in the value of the cosmological constant, usually considered to describe the energy density of the vacuum [26]. Astronomers have measured the rate with which the universe expands and have found this expansion to be accelerating, leading, in the framework of general relativity, to a very small, positive cosmological constant [27, 28]. However, the SM as a quantum field theory predicts a value orders of magnitudes above the one suggested by astronomical measurements.

Theoretical concerns include the $\sim$20 parameters of the SM, like the number of generations and masses of the fermions, which cannot be derived, but have to be experimentally determined. Furthermore, no explanation is given why the electric charges of electrons and protons cancel each other. Another important issue is gravity, which is the only one of the

four fundamental forces which the SM does not describe. But even assuming some underlying gravitational theory, the SM cannot explain why gravitation is so weak compared to the other forces. This is known as the "hierarchy problem", and is closely related to the "fine tuning problem": The Higgs field is constrained by the known masses of the W and Z bosons, and cancellations of the order of 10^{16} times the Higgs boson mass are required in order to reconcile its value with the huge quantum corrections from fermion and gauge boson loops predicted by the SM. Another point is the observation that the coupling constants depend on the energy of the particles involved in the interaction, and that in the SM these coupling constants almost but not fully coincide when extrapolated to high energies.

2.2.2 Models predicting a dilepton resonance

Historically, dilepton resonances have been a window to a better understanding of fundamental particles and forces. Figure 2.3 shows the reconstructed invariant mass distribution of ATLAS electron candidate pairs passing a Tight set of identification cuts (see Sec. 4.4). The resonance peak of the J/ψ meson, which is a $c\bar{c}$ bound state, was found at a mass of $\sim$3.1 GeV. The discovery of the J/ψ resonance in 1974 [29, 30] is called November Revolution, since it confirmed, together with subsequent discoveries of charmed baryons and mesons [31, 32, 33], the existence of a fourth quark and showed that the electroweak theory can be applied to hadrons. The resonance peak of the Z boson was discovered at a mass of 91.2 GeV in 1983 [1, 2]. Together with the charged gauge bosons W^+ and W^-, it was predicted by the electroweak theory (see Sec. 2.1) and helped to firmly establish the latter as part of the SM. The discovery of a dilepton resonance beyond the peak of the Z boson could have a similar effect on currently postulated extensions to the SM.

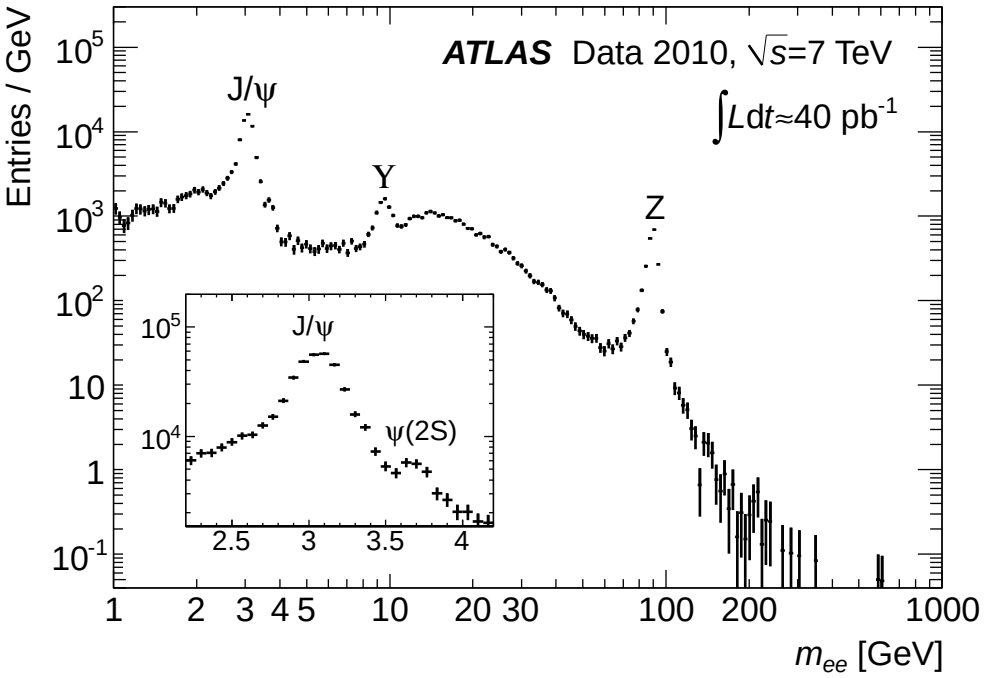

Figure 2.3: Reconstructed dielectron invariant mass distribution of electron candidate pairs passing the Tight identification cuts for events selected by low E_T threshold dielectron triggers [34]. The number of events is normalised by the bin width. Errors are statistical only.

There are several models that predict a resonance beyond the Z boson peak. Many of them try to solve specific problems of the SM, others use theoretical arguments like the unification of forces to motivate extensions to the SM.

Supersymmetric (SUSY) models [35, 36, 37] solve the hierarchy problem by assigning every SM particle a supersymmetric partner, canceling its loop contribution to the Higgs field. Since SUSY must be broken, one of the heavier superpartners of the SM particles could be discovered as a high-mass dilepton resonance.

Technicolor theories [38, 39, 40], inspired by how the strong interaction is modeled, avoid the hierarchy problem completely by proposing an alternative way of SSB which does not require a Higgs boson. Like QCD, technicolor models predict a zoo of composite particles,

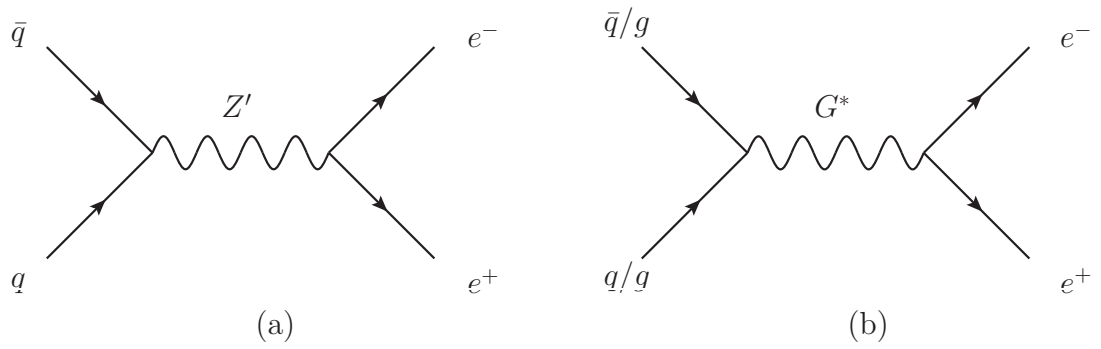

Figure 2.4: Feynman diagrams for Z' boson (a) and graviton (G*) (b) exchange.

which could be visible as dilepton resonances.

Additional U(1) symmetries lead to the emergence of new neutral gauge bosons, called Z' bosons, which might be heavy and observable as resonances in the dielectron spectrum (see Sec. 2.2.3 and Fig. 2.4(a)). Examples are the Sequential Standard Model, which is described in Sec. 2.2.4, the little Higgs models [41] and the higgsless Stueckelberg model [42]. The new U(1) symmetries could be due to Grand Unified Theories (GUTs). GUTs try to unify all three SM forces at high energies within large symmetry groups, which break at lower energies into the SM group and other symmetry factors. Suggested GUT models (among others) are the E_6 model, which is discussed in detail in Sec. 2.2.5, and the left-right symmetric models [43, 44, 45].

Extra dimensions might be the explanation for the extreme differences between the strengths of the fundamental forces. By allowing the graviton, the postulated exchange boson of gravitation, to propagate into extra dimensions, only a fraction of its strength might be visible in the standard 4-dimensional space-time. The Randall-Sundrum (RS) model of extra dimensions is discussed in Sec. 2.2.6. Its force carrier, the RS graviton, obtains mass through Kaluza-Klein excitations and decays into two electrons (compare Fig. 2.4(b)), hence it could be discovered in a dilepton search.

2.2.3 Additional U(1) symmetries

A large number of models predict the SM symmetry (Eq. 2.1) to be extended by at least one additional U(1)$'$ group:

$$\mathrm{SU}(3)_C \times \mathrm{SU}(2)_L \times \mathrm{U}(1)_Y \times \mathrm{U}'(1). \tag{2.21}$$

If this symmetry is broken, e.g. by the Higgs mechanism, a massive, neutral gauge Z' boson with spin-1 emerges. The addition to the electroweak Lagrangian density (Eq. 2.14) can be written as

$$\mathcal{L}_{EW,n+U(1)'} = \mathcal{L}_{EW,n} - g_{Z'} \sum_f [\bar{\psi}_{Lf} \gamma^\mu Q'_{Lf} \psi_{Lf} Z'_\mu + \bar{\psi}_{Rf} \gamma^\mu Q'_{Rf} \psi_{Rf} Z'_\mu]. \tag{2.22}$$

The structure of the additional term in the Lagrangian density is the same as the term describing the exchange of a SM Z boson (compare the second line in Eq. 2.14). The coupling $g_{Z'}$, the charges Q'_{Lf} and Q'_{Rf}, and the mass of the additional boson depend on the model which predicts the additional symmetry. In addition, couplings to exotic new fermions could be possible, and are even required in some models, in order to cancel anomalies (triangle Feynman diagrams in which the gauge symmetry would not be conserved).

Here, mass mixing between the Z and the Z' boson is neglected. Mass mixing can happen if there are mixed Z/Z' terms in the kinetic part of the Higgs Lagrangian, where the masses of the bosons are generated. Diagonalizing the resulting mass matrix shows the Z and Z' bosons as linear combinations of mass eigenstates Z_1 and Z_2. Precision measurements at the Z boson mass peak have put stringent limits on such a mixing, and it can be safely ignored here [20].

The matrix element of the DY process in Eq. 2.17 can now be extended to also include a term for the Z' boson:

$$\mathcal{M}^{\sigma,\tau}(\hat{s},\hat{t},\hat{u}) = \frac{e^2}{\hat{s}} \sum_{V=\gamma,Z,Z'} c^{\sigma}_{qqV}\; c^{\tau}_{eeV}\; P_V(\hat{s})\; M^{\sigma\tau}. \tag{2.23}$$

The couplings $c^{\sigma}_{ffZ'}$ are model dependent, the propagator however is assumed to be the same as for the Z boson (Eq. 2.19), with the exception of the width, which might differ because of new couplings, possible decays into exotic fermions, as well as the inclusion of the $t\bar{t}$ decay channel for Z' bosons with masses larger than twice the top quark mass.

The addition of the Z' boson as an exchange particle in the DY process happens in the matrix element. Therefore the total cross-section, which is proportional to $|\mathcal{M}|^2$, will not just be the sum of the cross-sections of DY and the new process. Instead there will be model-dependent interference effects.

2.2.4 Sequential Standard Model

In this analysis, the Sequential Standard Model (SSM) Z' boson [4] is used as a reference model. The Z'_{SSM} boson has the same couplings to the SM fermions as the Z boson (Eq. 2.18), but differs in mass and width ($\Gamma_{Z'} \propto M_{Z'}$). It can only exist if it couples to additional exotic fermions or as an excited state of the Z boson in the context of extra dimensions [47], but it is a very useful baseline model to make comparisons between the reach of different experiments.

The mass peak of the Z'_{SSM} is shown in Fig. 2.5, assuming a pole mass of 1500 GeV. The distributions in this figure are produced using the Pythia [46] generator (compare Sec. 5.2.1,

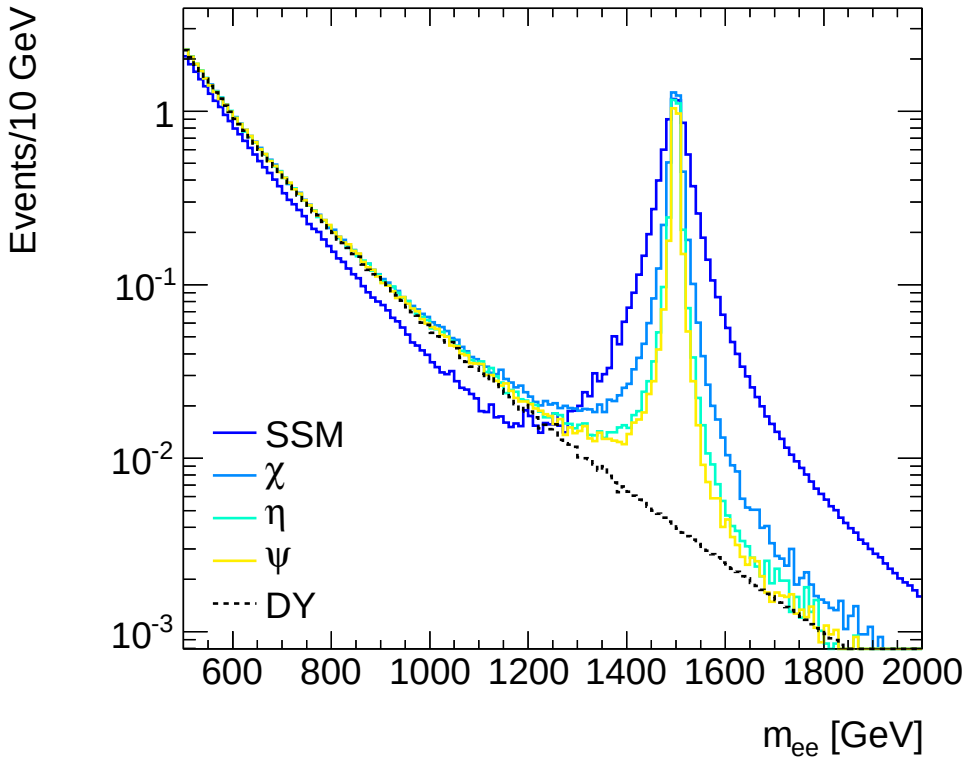

Figure 2.5: Mass peaks of the Z'_{SSM} and several E_6 bosons, assuming a pole mass of 1500 GeV. The distributions are produced with the PYTHIA [46] generator; their normalization corresponds to 1 fb^{-1} of pp collison data at a CM energy of 7 TeV. For interpretation of the references to color in this and all other figures, the reader is referred to the electronic version of this dissertation.

detector effects like resolution are not included) and correspond to 1 fb^{-1} of data. It can be seen that below the mass peak, the differential cross-section for the DY process alone is larger than the combined cross-section for DY and Z'_{SSM} due to destructive interference. However, the additional cross-section at the peak dominates the shape, therefore interference effects are neglected in this analysis.

2.2.5 E_6 model

GUTs are interesting because they unify electroweak and strong forces by postulating one single gauge symmetry at a very high energy (referred to as the GUT scale). This can help

to explain relations between quarks and leptons, since both can be part of the same group representation. The GUT considered in this analysis is a model based on the symmetry group E_6 [3, 4], which can be derived from superstring theories. At the GUT scale, the E_6 symmetry successively breaks into weaker symmetries,

$$E_6 \rightarrow \mathrm{SO}(10) \times \mathrm{U}(1)_\psi \rightarrow \mathrm{SU}(5) \times \mathrm{U}(1)_\chi \times \mathrm{U}(1)_\psi, \tag{2.24}$$

where SU(5) breaks into the SM symmetry (Eq. 2.1). The model suggests that a linear combination of the two additional U(1) gauge groups is broken at the electroweak scale (about 1 TeV), producing one additional gauge boson whose charges depend on the fermions f, their chiralities σ and the mixing angle θ_{E_6}:

$$Q'^{\sigma}_f(\theta_{E_6}) = Q^{\sigma}_{f\chi}\cos\theta_{E_6} + Q^{\sigma}_{f\psi}\sin\theta_{E_6}, \quad 0 \leq \theta_{E_6} < \pi. \tag{2.25}$$

The coupling in the matrix element (Eq. 2.23) can be written as:

$$c^{\sigma}_{ffZ'} = \sqrt{\frac{5}{3}}\frac{e}{\cos\theta_W} Q'^{\sigma}_f(\theta_{E_6}), \tag{2.26}$$

where the factor $\sqrt{\frac{5}{3}}\frac{e}{\cos\theta_W}$ corresponds to the $U(1)_Y$ coupling g' (see Eq. 2.13), with an additional normalization factor to unify the SM gauge groups into an SU(5) group at GUT energies.

Table 2.2 lists the names of models for several choices of θ_{E_6} [3, 4], which can be derived from different GUT scenarios and could be detectable at the LHC. As mentioned above, the charges $Q^{\sigma}_{f\chi}$ and $Q^{\sigma}_{f\psi}$ depend on the type of fermion and the helicity. They are listed

Model	Z'_χ	Z'_ψ	Z'_η	Z'_I	Z'_{N}	Z'_{S}
θ_{E_6}	0	$\pi/2$	$-\arctan\sqrt{5/3}$	$\pi+\arctan\sqrt{3/5}$	$\arctan\sqrt{15}$	$\arctan\sqrt{15}/9$

Table 2.2: Several motivated choices of θ_{E_6} and the corresponding models [3, 4].

	u_L, d_L	u_R, e_R	d_R	e_L
$2\sqrt{10}\,Q_\chi$	-1	1	-3	3
$2\sqrt{6}\,Q_\psi$	1	-1	-1	1

Table 2.3: Charges of SM fermions in the E_6 model [3, 4].

in Table 2.3 for the first fermion generation, but are the same for the other generations. According to the underlying larger symmetries, some of the quarks and leptons share the same charges.

All of the E_6 models predict right-handed neutrinos, and most need the addition of exotic fermions in order to cancel anomalies [20]. Right-handed neutrinos and exotic fermions are assumed to be too heavy to participate in the Z' decay.

Figure 2.5 shows the dielectron invariant mass peaks of the Z'_χ, Z'_η and Z'_ψ bosons, produced by the Pythia [46] event generator assuming a pole mass of 1500 GeV.

2.2.6 Randall-Sundrum graviton

As a gauge theory (see Sec. 2.1.1), the SM predicts exchange bosons for the electromagnetic, strong and weak forces. Since gravitation is also a force, the graviton has been postulated as its exchange boson. Its spin would be 2, because of the mathematical structure of the interaction. However, no viable quantum field theory of gravitation has been developed yet, due to infinities arising in the calculations. The "classical limit" of such a theory would be

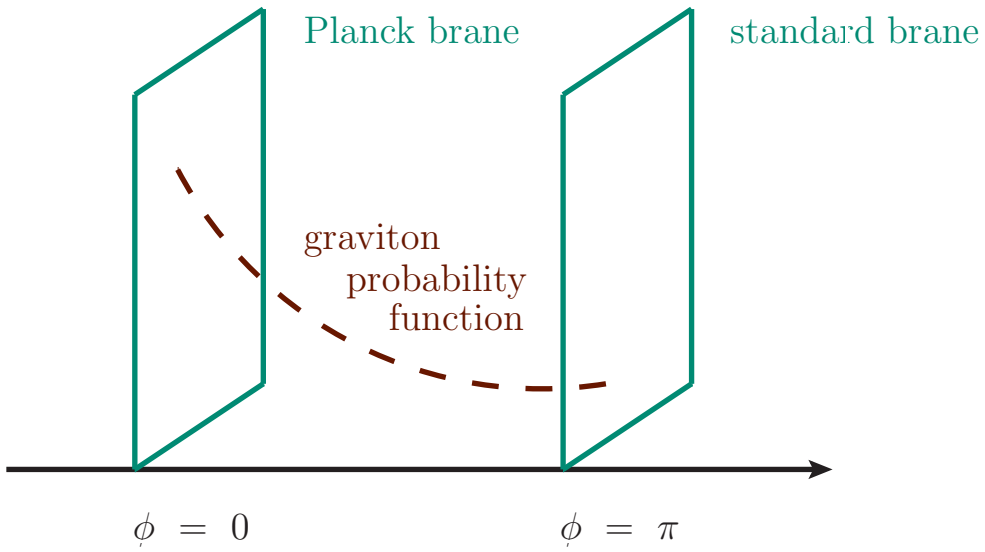

Figure 2.6: Suppression of the graviton wave function at the standard brane.

the theory of general relativity [48]. In this limit, it is possible to look at different space-time scenarios and their effects on SM interactions, the gravitational force and its hypothetical exchange particle, the graviton.

In the last few decades, models with extra dimensions have been proposed to explain why gravity is so much weaker than the other fundamental forces, or, formulated differently, why the Planck scale ($M_{Pl} \approx 10^{16}$ TeV) is so much higher than the electroweak scale ($M_{EW} \approx 1$ TeV). While the model of Large Extra Dimensions [49] leads to a new hierarchy, the Randall-Sundrum (RS) model [5] manages to remove the hierarchy problem completely.

In its minimal form, the RS model introduces one extra dimension ϕ which is considered to be finite, forming a circle with radius r_c at every point in the standard 4-dimensional space-time. Two 4-dimensional subspaces, called branes, are suggested to be located at angles $\phi = 0$ and $\phi = \pi$ of this circle: the standard space-time brane at $\phi = \pi$ and a Planck brane at $\phi = 0$ (see Fig. 2.6). All SM particles are confined to the standard brane; only the graviton field extends into the extra dimension. In the framework of general relativity,

this extra dimension results in a 5-dimensional space-time metric with a "warping" factor in front of the standard 4-dimensional metric:

$$ds^2 = e^{-2kr_C\phi} g_{\mu\nu} dx^\mu dx^\nu + r_C^2 d\phi^2, \tag{2.27}$$

where x^μ, x^ν are the standard 4-dimensional coordinates, ϕ is the extra dimension, and k is a scale of the order of the reduced Planck scale $\bar{M}_{Pl} = M_{Pl}/\sqrt{8\pi} \approx 2\ 10^{-18}$. As a result of the warping factor $e^{-2kr_C\phi}$, the graviton probability functions are exponentially suppressed away from the Planck brane, as illustrated in Fig. 2.6. This reduces the real masses m_0 of particles in the standard brane to an apparent mass m:

$$m = e^{-kr_C\pi} m_0. \tag{2.28}$$

If $kr_C \approx 12$, the electroweak scale is $M_{EW} \approx e^{-12\pi} M_{Pl}$, solving the hierarchy problem.

As the graviton field propagates through finite extra dimensions, it can undergo Kaluza-Klein excitations, which can be compared to excited states of a quantum harmonic oscillator. Just like the excited oscillator states have higher energies than the ground state, the graviton can obtain a mass, which depends on the order of the excitation n [50]:

$$m_n = k x_n e^{-kr_C\pi}. \tag{2.29}$$

Here, x_n is the n^{th} root of the Bessel function j_1. If the mass of a certain order as well as the scale k are known, the couplings and width of the excited graviton states can be derived.

In this analysis, we set limits on the first excitation of the graviton, whose mass is

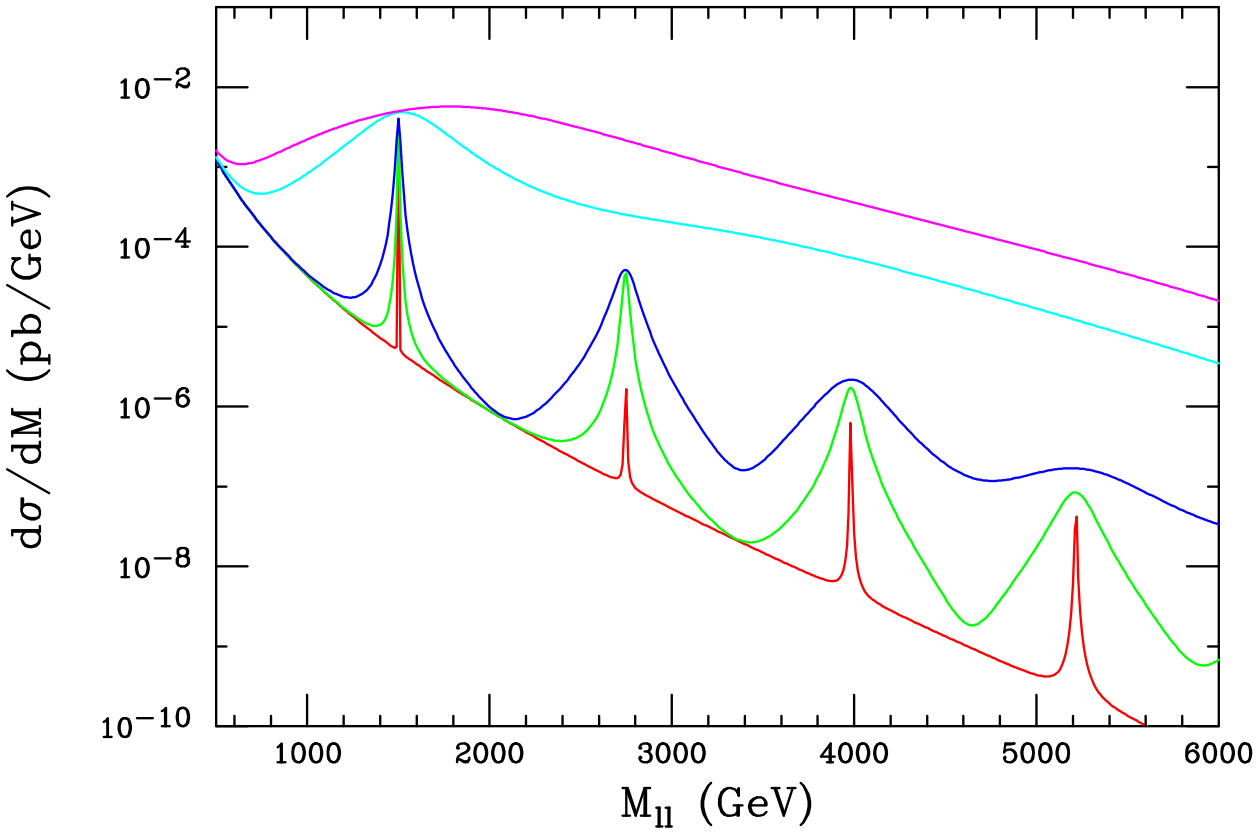

Figure 2.7: Line shapes of Kaluza-Klein resonance peaks of a 1500 GeV RS graviton, as they might be produced at the LHC. From top to bottom, the curves are for $k/\bar{M}_{Pl} = 1$, 0.5, 0.1, 0.05, and 0.01, respectively [52].

expected to be at the TeV scale. Instead of k, the normalized scale $k/\bar{M}_{Pl}$ is used as the input parameter. If the RS model solves the hierarchy problem, a small $k/\bar{M}_{Pl}$ implies a large radius r_C. This restricts the allowed values of $k/\bar{M}_{Pl}$, since large extra dimensions are easier to observe. On the other hand, if r_C is too small, the theory becomes non-perturbative [51]. Values considered in this analysis are $0.01 \leq k/\bar{M}_{Pl} \leq 0.1$.

Among other channels, the graviton is predicted to decay into two electrons and, depending on its cross-section and width, its first excitation could be visible as a resonance in the dielectron invariant mass spectrum. The shape (height and width) of the resonance peak depends on $k/\bar{M}_{Pl}$ as mentioned above and is illustrated in Fig. 2.7. Different from the Z' bosons, the graviton is a spin-2 particle, and its production does not interfere with the DY

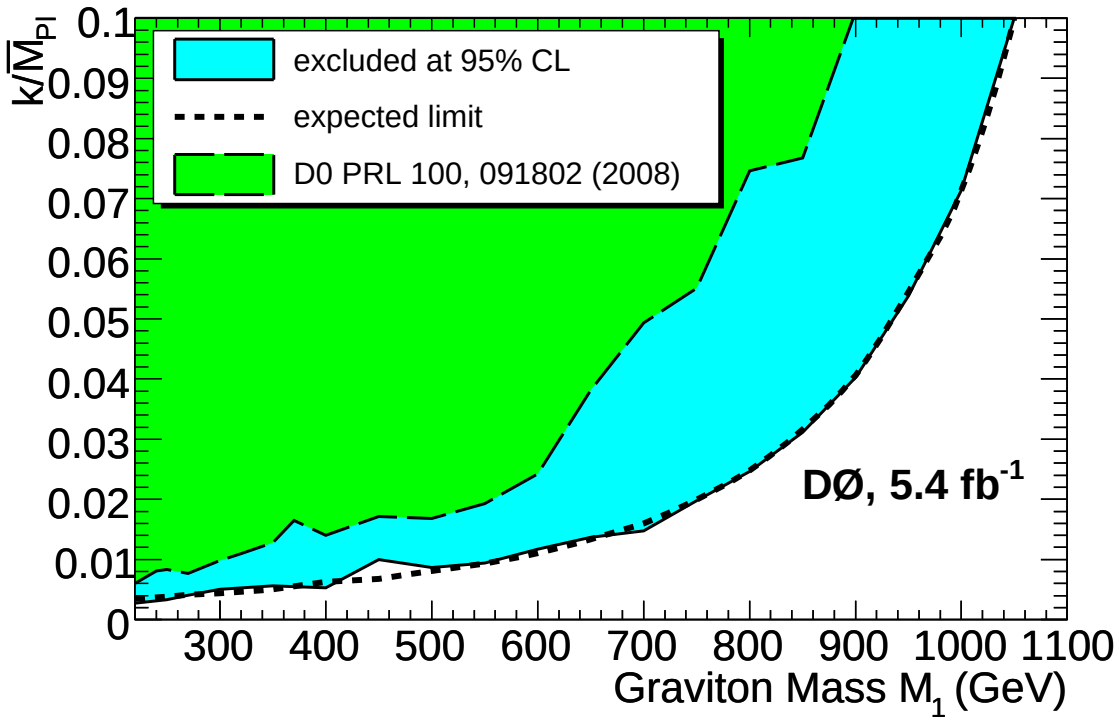

Figure 2.8: Excluded regions in the space spanned by $k/\bar{M}_{Pl}$ and the graviton mass measured at the 95% C.L. by the DØ collaboration [53].

process. Furthermore, it can be produced in gluon-gluon annihilation and decay into two photons, which is not possible for the resonance in the other models.

2.2.7 Previous limits

Before summer 2011, the strongest constraints for a Z'_{SSM} boson came from precision measurements of the Z boson peak at the Large Electron Positron collider (LEP), CERN. A potential Z' boson would change the shape of the Z boson mass peak by mixing (compare Sec. 2.2.3). The combination of the indirect measurements [54, 55, 56, 57] excludes a Z'_{SSM} boson with a mass below 1.787 TeV at the 95% confidence level (C.L.) [58].

Direct experimental limits are determined at hadron colliders by searching for resonances in the dielectron, dimuon and, in the case of the RS graviton, diphoton invariant mass

spectra. The Tevatron collider at Fermilab, Batavia, USA, was shut down in fall 2011. Until then it collided protons and antiprotons with $\sqrt{s} = 1.96$ TeV, while the LHC data used in this analysis are produced by proton-proton (pp) collisons at $\sqrt{s} = 7$ TeV. Higher collision energies increase the accessible search region in the invariant mass spectrum, allowing the ATLAS and CMS collaborations at the LHC to obtain mass limits higher than the Tevatron collaborations (CDF and DØ), with only a fraction of the number of recorded collisions.

Limits obtained by the ATLAS, CMS and Tevatron collaborations for the Z'_{SSM} before summer 2011 were all of the order of 1 TeV [59, 60, 61, 62], the highest being the limit by CMS with 40 pb^{-1} of data, which excluded the Z'_{SSM} boson at the 95% C.L. for masses below 1.140 TeV [60]. It was a combination of the measurements in the dielectron and dimuon channel. Limits for the E_6 Z' bosons were also determined by several collaborations [59, 60, 61, 63]. Table 2.4 shows the 95% C.L. mass limits for different E_6 models obtained with 40 pb^{-1} of ATLAS dimuon and dielectron data [59].

Model	Z'_ψ	Z'_{N}	Z'_η	Z'_I	Z'_{S}	Z'_χ
Mass limit [TeV]	0.738	0.763	0.771	0.842	0.871	0.900

Table 2.4: Combined mass limits at the 95% C.L. on the E_6-motivated Z' models using 40 pb^{-1} of ATLAS dimuon and dielectron data [59].

Direct mass limits for the RS graviton with a coupling parameter $k/\bar{M}_{Pl} = 0.1$ were obtained by the CMS and Tevatron collaborations, and were of order 1 TeV, the highest being 1.079 TeV by the CMS collaboration with 40 pb^{-1} of combined dimuon and dielectron data [60]. Figure 2.8 shows the excluded regions in the space spanned by $k/\bar{M}_{Pl}$ and the graviton mass, measured at the 95% C.L. by the DØ collaboration using 5.4 fb^{-1} of Tevatron data and combining the dielectron and diphoton decay channels.

Chapter 3

Experimental setup

The LHC is a circular collider at CERN in Geneva, Switzerland. This chapter gives an overview over the technologies and strategies that allow the LHC to achieve record collision energies at very high rates. As the data analyzed in this thesis were recorded with the ATLAS detector, one of the four large detectors along the LHC ring, the second part of this chapter describes its design, focusing on the components that are relevant for the detection and reconstruction of electrons.

3.1 Large Hadron Collider

The most powerful accelerator ever built, the LHC [64, 65] was designed to collide two proton beams 40 million times per second at a CM energy of 14 TeV (7 TeV per proton) with an instantaneous luminosity of up to $L = 10^{34}$ cm^{-2}s^{-1}. The instantaneous luminosity measures the actual pp collision rate, which does not only depend on the frequency of the beam crossings, but also on the density of the protons in the beam and the area in which the two beams overlap. The LHC also has the functionality to collide heavy ions (e.g. lead)

and has done so successfully already. On a ring with a circumference of 27 km, the beams are crossed at four interaction points, where the four large LHC experiments are located: ATLAS, ALICE, CMS and LHCb. ATLAS and CMS are both general purpose detectors, while LHCb was built for analyzing flavor physics and ALICE primarily for detecting heavy ion collisions.

3.1.1 Accelerator chain

The LHC ring is the last link of the CERN accelerator chain [66] (see Fig. 3.1). A number of accelerators are used to bring the protons successively to higher energies and to split the beam into bunches. With the exception of the newly built LHC, the accelerators in the chain are older machines. Updated to serve as preaccelerators for the LHC, they were originally built for previous experiments, like the Super Proton Synchrotron (SPS), where the W and Z bosons were discovered. Every component of the accelerator chain is optimized for a certain energy range. It was decided to fill the LHC with protons only instead of protons and antiprotons, because the production of the latter limits the collision rates that can be achieved.

The chain starts with a bottle of pure hydrogen gas, which lasts for about a year of LHC running [67]. The hydrogen is ionized in a duoplasmatron, which uses a cathode to emit electrons. The electrons are focused and hit the hydrogen molecules, splitting and ionizing them to produce bare protons, which are then extracted and accelerated by an electric field.

The next station for the protons is a 1 m long radiofrequency quadrupole, which consists of sinusoidal electrodes. The proton beam is accelerated to 750 keV, as well as focused and divided longitudinally into bunches.

The protons receive an energy of 50 MeV (which already gives them 30% of the speed of light) in a linear accelerator called LINAC 2. This accelerator is 30 m long and consists of three tanks; each of the tanks contains a line of drift tubes in an alternating electric field. The frequency of the electric field is such that the protons are shielded within the tubes when the field points in the wrong (decelerating) direction, so that they always gain energy as they pass from tube to tube.

The protons are next accelerated in a series of synchrotrons where magnets are used to bend the protons' path to form a closed loop. The strength of the magnetic fields is regulated and depends on the speed of the particles in order to keep the radius of the beam trajectory constant. The energy that protons can reach in a synchrotron is usually limited by the maximum strength of its bending magnets. To achieve further acceleration, the protons must be transferred into another ring with larger radius and/or more powerful magnets. All the synchrotrons in the LHC chain use resonating cavities, in which the electric field forms a standing wave whose frequency and phase are timed to accelerate the protons.

The first circular accelerator in the chain is the Proton Synchrotron Booster (PSB). It actually consists of four circular beam lines, stacked on top of each other, with a circumference of 157 m. The protons leave the PSB with an energy of 1.4 GeV (corresponding to 91% of the speed of light) and are fed into the next machine as six bunches.

The Proton Synchrotron (PS) is the oldest machine in the chain, built in 1959. On a circle of 682 m, it accelerates the protons to 25 GeV. Furthermore, it splits the six bunches into up to 72, which circulate closely together in a so-called bunch train. The concept of bunch trains is important, because each injection takes time. Bunch trains allow the injection of several bunches into an accelerator at once, making it possible to fit more bunches into the

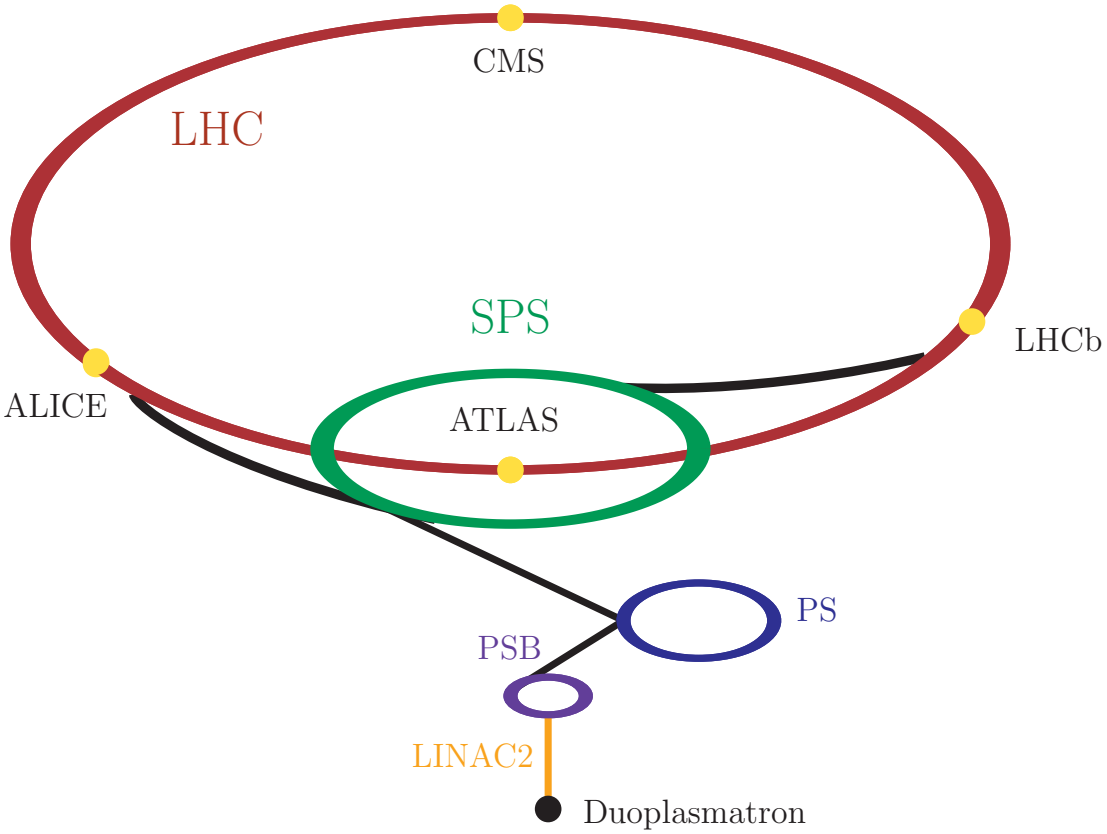

Figure 3.1: CERN accelerator complex.

ring.

The last accelerator before the LHC is the SPS, which has a circumference of 7 km. There are two transfer lines to the LHC so that proton beams can be injected into the LHC ring in both directions. The protons leave the SPS with an energy of 450 GeV as bunch trains consisting of up to $4 \cdot 72$ bunches. A nominal LHC fill contains 2808 bunches in each direction, produced in 12 SPS cycles, each cycle consisting of 3-4 PS fills.

3.1.2 LHC design

The LHC is a synchrotron located 50-175 m underground, in a tunnel with a circumference of 27 km. It consists of two beam lines, in which two proton beams complete around 11,000

turns per second in opposite directions to be collided at four interaction points. An ultra-high vacuum (10^{-10} Torr, corresponding to three million molecules per cm^3) is necessary in the beam lines to avoid deflecting protons on gas molecules.

To accelerate the protons, the LHC uses eight superconducting cavities per beam. The superconducting material makes it possible to store large amounts of energy. This allows for fast acceleration, while only tiny fractions of the field energy are given to the beam when it passes, making the cavity fields quite insensitive to small variations in the beam current. As protons lose little energy due to synchrotron radiation after the acceleration phase, the cavities' main task is to keep the bunches of protons longitudinally focused. This happens because the cavities form so-called radiofrequency buckets, in which the synchronous protons (the ones right in the middle of the bucket) are optimally accelerated, while the other protons oscillate around these central protons, getting too much or too little acceleration. Since the cavities need to be cooled down to 4.5 K to maintain their superconducting properties, they are grouped as four within a cryostat.

In order to keep protons at energies of 7 TeV in a circular orbit, magnets with very large fields (up to 8 T) are needed. For the wires of the magnet coils, a superconducting material, niobium-titanium, is used. This allows for the creation of large fields and is important to save energy, since the currents needed to produce such magnetic fields are huge ($\sim$12 kAmp). For bending the proton orbits, the LHC uses 1232 dipole magnets of 15 m length. Quadrupole and sextupole magnets are used for transverse beam focusing. Additional magnets correct errors and improve the beam quality. For the metal to be superconducting and able to transport large currents in the presence of a strong magnetic field, the magnets have to be cooled down to 1.9 K.

Because the LHC uses so much superconducting technology, a very powerful cooling system is required. 10,000 tons of liquid nitrogen are used to bring the temperature of around 100 tons of helium down to 80 K. Refrigeration units achieve further cooling. Below 2 K, liquid helium is superfluid, which means it has excellent heat transfer properties and can propagate into tiny cracks in the magnet coils to absorb heat.

This design enables the LHC to achieve unprecedented collision rates at record CM energies. The strength of the dipole magnets and the design of the cavities allow for protons with very high energies. In addition, the accelerators further up the chain were upgraded to accelerate large numbers of protons and divide them into many bunches. The higher-order magnets (quadrupoles, sextupoles etc.) increase the density of the proton bunches, by squeezing them transversally. The cavities keep the bunches compressed longitudinally. The colliding frequency is further enhanced by using bunch trains, with very few and short gaps between the bunches, so that more bunches per turn can be brought to collide at a given interaction point. Finally, the beams are aligned to cross with a large overlap.

3.1.3 LHC status 2011

The LHC started colliding protons with protons in November 2009 and reached a CM energy of 7 TeV (3.5 TeV per beam) in March 2010. Collisions at 8 TeV are foreseen in 2012. The design CM energy of 14 TeV is expected to be achieved in 2014 after an extended technical stop. The lower energy also limits the luminosity. While the LHC is planned to eventually run with 2808 bunches per beam and an instantaneous luminosity of $L = 10^{34}$ cm^{-2}s^{-1}, in 2011, the maximum number of bunches per beam were 1380 and the maximum instantaneous luminosity $L = 3.65 \cdot 10^{33}$ cm^{-2}s^{-1}.

3.2 ATLAS detector

ATLAS [68] is a general purpose detector, built to detect, filter and record high energy pp and heavy ion collisions produced by the LHC. It was designed for precision measurements of SM parameters as well as the search for a wide variety of possible new physics phenomena. The detector is located 92.5 m underground at one of the LHC collision points. It is constructed cylindrically around the beamline, weighs 7000 tons and is 44 m long. The ATLAS collaboration was formed in 1992. Today it consists of ∼3000 physicists from 38 countries. The detector was constructed between 2003 and 2008.

3.2.1 Coordinate system

The coordinate system of the ATLAS detector is illustrated in Fig. 3.2. The origin is set at the nominal interaction point in the center of the detector. The positive x-axis points to the center of the ring, the positive y-axis upwards. The z-axis follows the beam line. The angle ϕ is defined with respect to the positive x-axis and wraps around the beam axis, while the angle θ is defined with respect to the positive y-axis.

The pseudo-rapidity is defined as $\eta = -\ln\tan(\theta/2) = 1/2\ln\frac{|\vec{p}|+p_z}{|\vec{p}|-p_z}$. For relativistic objects ($|\vec{p}| \approx E$), the pseudo-rapidity corresponds to the rapidity $y = 1/2\ln\frac{E+p_z}{E-p_z}$. The transverse momentum p_{T}, transverse energy E_{T}, and missing transverse energy $E_{\mathrm{T}}^{\mathrm{miss}}$ are defined in the x-y plane. Furthermore, the distance ΔR in the pseudorapidity-azimuthal space is defined as $\Delta R = \sqrt{\Delta\eta^2 + \Delta\phi^2}$.

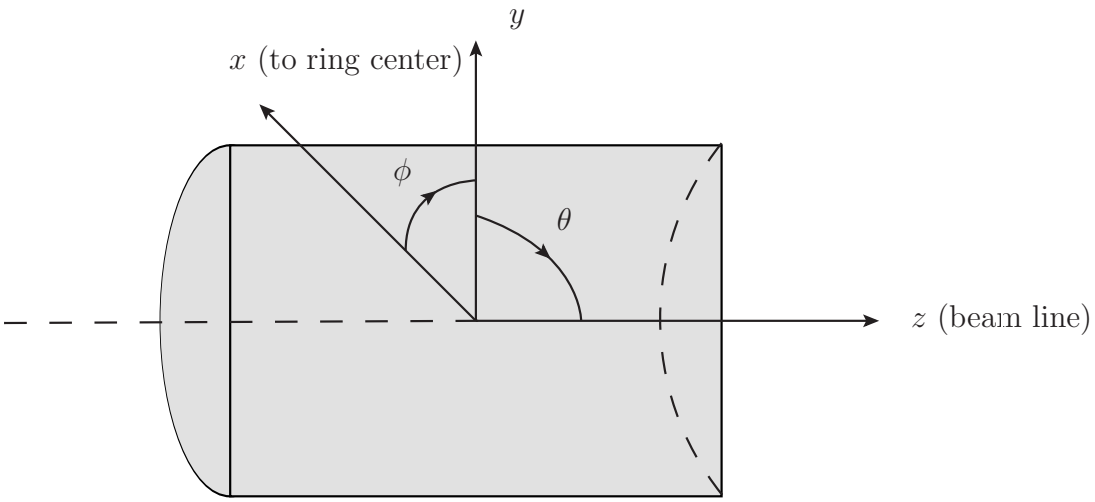

Figure 3.2: Coordinate system of the ATLAS detector.

3.2.2 Design

As a general purpose detector, ATLAS needs to be able to discover a wide range of new physics phenomena. Thanks to the record high CM energy of the LHC, we can search for heavier particles than ever before. In order to be able to detect and reconstruct possible decay products up to very high energies, ATLAS has to be as hermetical as possible and cover a large η range. In order to identify electrons in the presence of the large QCD multijet background produced in pp collisions, calorimetric resolution as well as tracking capabilities must be excellent. Subdetectors with high resolution close to the beam line are needed to find jets produced by b-quarks, which, due to their lifetime, can be tagged by looking for a small distance (a couple of mm) between the primary and secondary interaction vertices. Furthermore, new physics is rare. In order to find it, the design number of pp collisions at the LHC is 40 million times per second, which requires very fast detection and efficient filtering at a very early stage in the data flow.

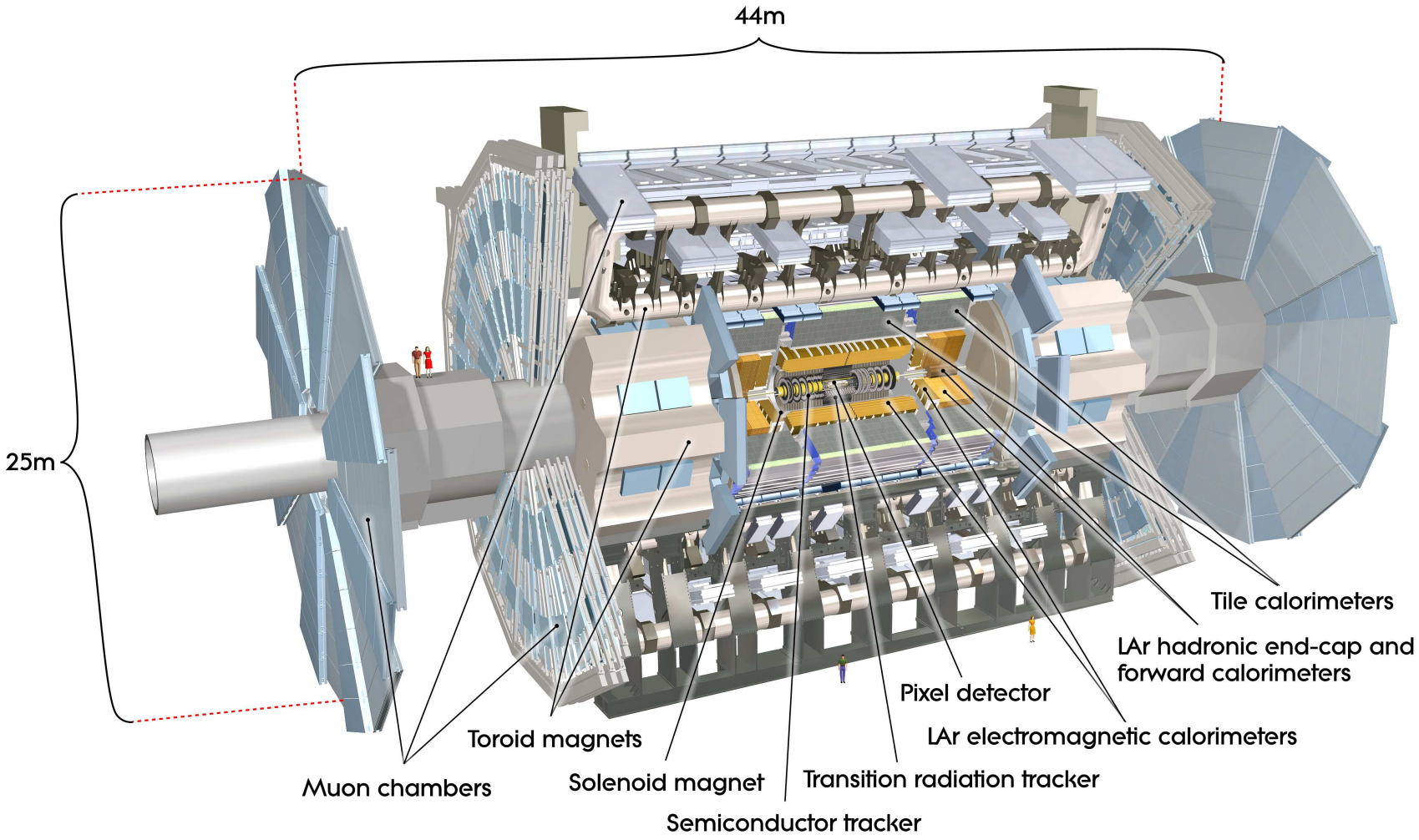

Figure 3.3: Schematic view of the ATLAS detector [69].

The ATLAS detector is built like an onion around the beam line (see Fig. 3.3). From the inside out, it consists of an inner detector for tracking, a calorimeter system for particle identification and measuring the energy of electrons, photons and quark/gluon jets, as well as a muon spectrometer. There are two magnet systems, a solenoid around the inner detector and a large toroid for the muon system. The magnets bend the tracks of charged particles and allow for charge/momentum determination.

The ATLAS Inner Detector consists of three subdetectors submerged in a solenoidal magnetic field (2 T). It records the tracks of charged particles. Pattern recognition allows the determination of the interaction vertex as well as of additional vertices from particles with a long life-time, like B-mesons.

Located outside the Inner Detector's solenoid are the electromagnetic (EM) and hadronic calorimeters. They use a sampling technique, which means they consist of alternating layers of absorbing and ionizable material. The EM calorimeter uses lead as the absorber and liquid argon (LArg) as the active layer. The hadronic calorimeter is constructed using steel and scintillating tiles in the barrel and copper (as well as tungsten in some parts) with LArg in the forward regions.

Muon momenta are measured in the muon spectrometer, consisting of three layers of high precision tracking chambers. Most of these chambers are drift tubes, filled with gas that can be ionized by a traversing muon. The alignment of the chambers has to be done very carefully to achieve good momentum resolution, especially for particles with high p_{T} (the design resolution is 10% for muons with $p_{\mathrm{T}} = 1$ TeV). The chambers are surrounded by an air core toroid system. Of course, charged particles other than muons, which traverse the calorimeters, could be detected by the system as well.

At nominal luminosity, the ATLAS trigger system needs to filter 200 interesting events per second out of 40 million others. It consists of three stages, Level 1 (L1), Level 2 (L2) and the Event Filter (EF). L1 is hardware based, and uses a reduced granularity in the calorimeters as well as specialized, fast muon chambers to trigger on high transverse energy/momentum objects, $E_{\mathrm{T}}^{\mathrm{miss}}$ and large total transverse energies. L1 chooses regions of interest (ROI), which are picked up by L2 and analyzed with dedicated software algorithms on the full detector granularity. The EF employs offline analysis algorithms to pick interesting events. A menu of different cut combinations exists at all stages and it is possible to set prescales to record only a fraction of the events triggered by a certain menu item.

A fast, efficient data acquisition system (DAQ) is needed to cope with the large amounts of data. The data have to be channeled from the electronic read-outs of the different detector systems to the storage disks. Event fragments from the different subdetectors are buffered while the L1 trigger makes its decision. The requested ROI information is transferred to the L2 trigger. Once L2 accepts an event, the full event information is assembled by the Event Builder, so that the event can be analyzed by the EF. Accepted events are then moved to the storage disk. The amount of data written to disk is still enormous; around 1000 million events are recorded per year with a typical event in 2011 having a size of 1.1 MB [70].

Both the Inner Detector and the EM calorimeter need to be understood very well to allow for the reconstruction of electrons and are therefore discussed in more detail in Sec. 3.2.3 and Sec. 3.2.4. Electron triggers are discussed in Sec. 4.2.

3.2.3 Inner Detector

In order to provide high momentum and vertex resolution as well as good tracking abilities, the ATLAS Inner Detector [68] consists of three subdetectors, which are submerged into a solenoidal magnetic field (see Fig. 3.4). The inner layers, the Pixel detector and the Semiconductor Tracker (SCT), have very high granularities and typically provide three (Pixel detector) and eight (SCT) hits per track, while the outermost detector, the Transition Radiation Tracker (TRT), offers around 36 hits per track with less precision but over a larger volume, thus contributing significantly to the momentum reconstruction.

The Pixel detector and the SCT cover a pseudo-rapidity range up to $|\eta| < 2.5$. They consist of semiconducting silicon elements with an applied electric field ($\sim$150 V). Charged particles passing through the semiconducting material set charge carriers free that accumulate at the electrodes. This results in a charge difference which is turned into a signal current. Both detectors are exposed to immense amounts of radiation from the proton beams. The innermost Pixel layer is as close as 5 cm to the beam line and will have to be replaced after three years of running at design luminosity. Both detectors are cooled to reduce the leakage current, which increases with irradiation.

The Pixel detector consists of 80 million silicon pixels (each with a size of 50 by 400 μm). It has three barrels around the beam line and three disks at each side, covering radii between 5 and 15 cm. The SCT, covering radii up to 52 cm, contains silicon microstrips, measuring 80 μm by 12.6 cm. The microstrips are arranged in double layers, each layer with two sets of strips at a small angle to each other, in order to obtain a 3D measurement.

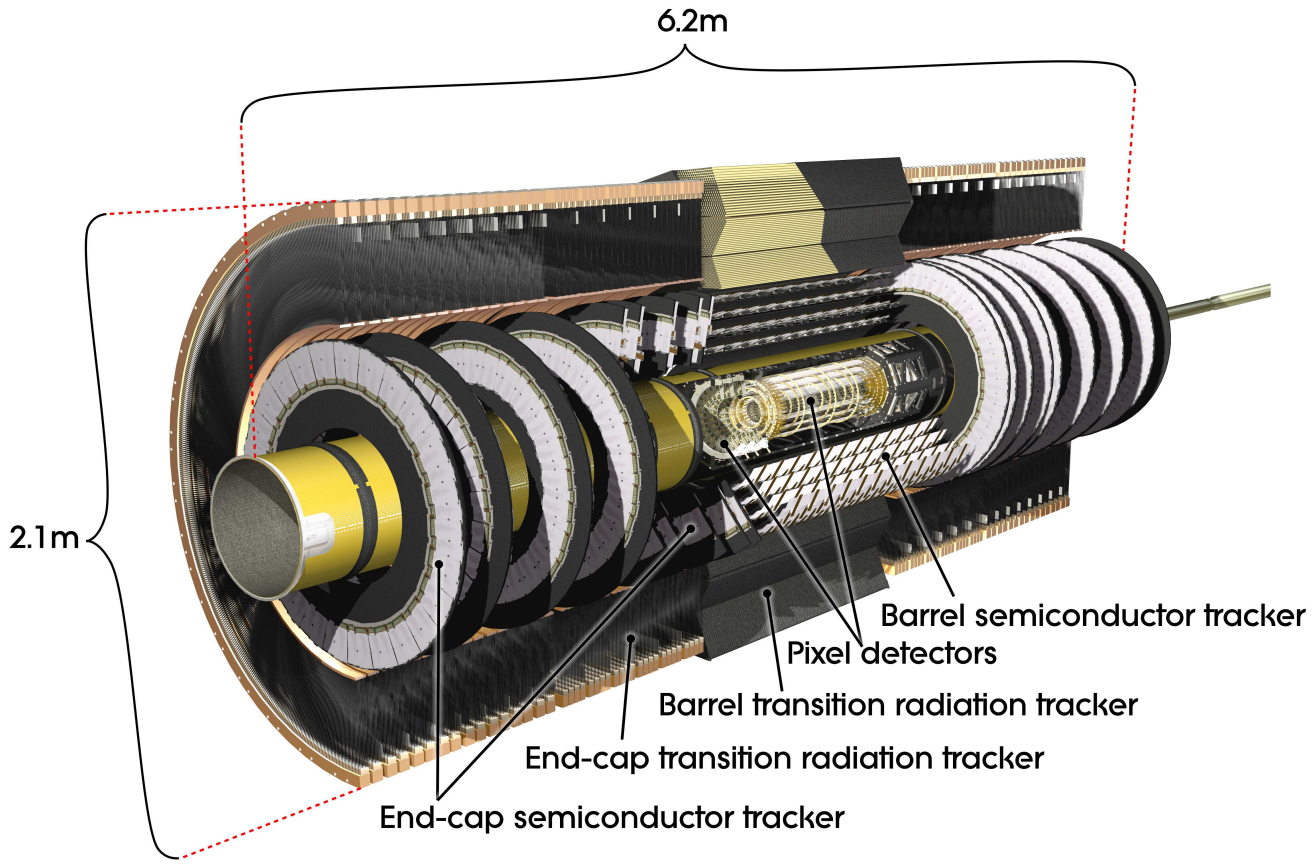

Figure 3.4: Schematic view of the ATLAS Inner Detector [69].

The TRT is a drift tube system, extending to $|\eta| < 2$. It consists of straw tubes that are 4 mm wide and up to 1.44 m long and are filled with a Xe/CO2/O2 gas mixture. Within the tubes are gold-plated tungsten wires, serving as anodes, kept at ground potential, while the tubes themselves are used as cathodes, with a potential of -1530 V. Charged objects ionize the gas and the resulting ions travel to the electrodes. The drift time (max. 45 ns) allows for a determination of the objects' crossing R, ϕ coordinates with a resolution of 170 μm. The TRT does not provide information about the z-coordinate. In addition to its tracking capabilities, the TRT can contribute to particle identification. The straws are surrounded by polypropylene, which produces transition radiation (photon emission if a relativistic particle crosses the boundary of two materials). The xenon gas reacts with the photons, causing a larger signal than the passing charged particles. A two-threshold system makes it possible to distinguish between tracking and transition radiation signals. Since electrons are lighter than hadrons, the necessary E_{T} for an electron to cause transition radiation is $\mathcal{O}(1$ GeV), while for pions, which are almost 300 times heavier, the necessary E_{T} is $\mathcal{O}(100$ GeV). Of course, this discrimination breaks down for particles with very high E_{T}.

3.2.4 Electromagnetic calorimeter

The EM calorimeter [68] has alternating layers of absorbing lead and LArg, which serves as the active medium. Submerged into the LArg are electrodes creating electric fields. Charged particles traversing the lead interact with it through bremsstrahlung and produce secondary particles, which can interact with the material themselves, thus creating tertiary particles (see Fig. 3.5). This showering can also be initiated by a photon converting into an electron pair and continues until all the energy is absorbed [71]. When the shower particles travel

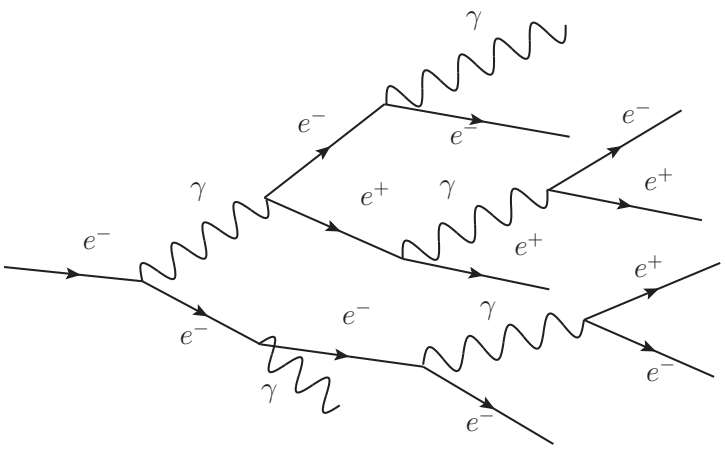

Figure 3.5: Schematical illustration of an electron shower in the EM calorimeter.

through the LArg, they ionize the liquid. The ions travel to the electrodes, where they produce a current proportional to the applied voltage and the energy deposited in the LArg.

The coverage of the EM calorimeter is up to $|\eta| < 3.2$ overall, and up to $|\eta| < 2.5$ with fine granularity, matching the Inner Detector. It consists of a barrel and two endcap wheels (see Fig. 3.6). The barrel ($|\eta| < 1.475$) is constructed of two halves, separated by a small gap (4 mm) at z = 0. The endcap wheels are each divided into an inner and an outer wheel.

In order to achieve uniformity in ϕ, to avoid azimuthal cracks, and to allow for very fast read-out, the EM calorimeter is constructed like an accordion. Lead absorbers, LArg, and electrodes are folded following a zig-zag pattern (see Fig. 3.7). In the barrel, the folds are parallel to the beam line, and the angle is varied with the radius to keep the width of the LArg gap constant. For the endcaps, the geometry is more complicated. Here, the accordion folds are perpendicular to the beam line and the angle and amplitude of the folding vary with the radius. The width of the LArg gap therefore varies, which is accounted for by changing the applied voltages with η.

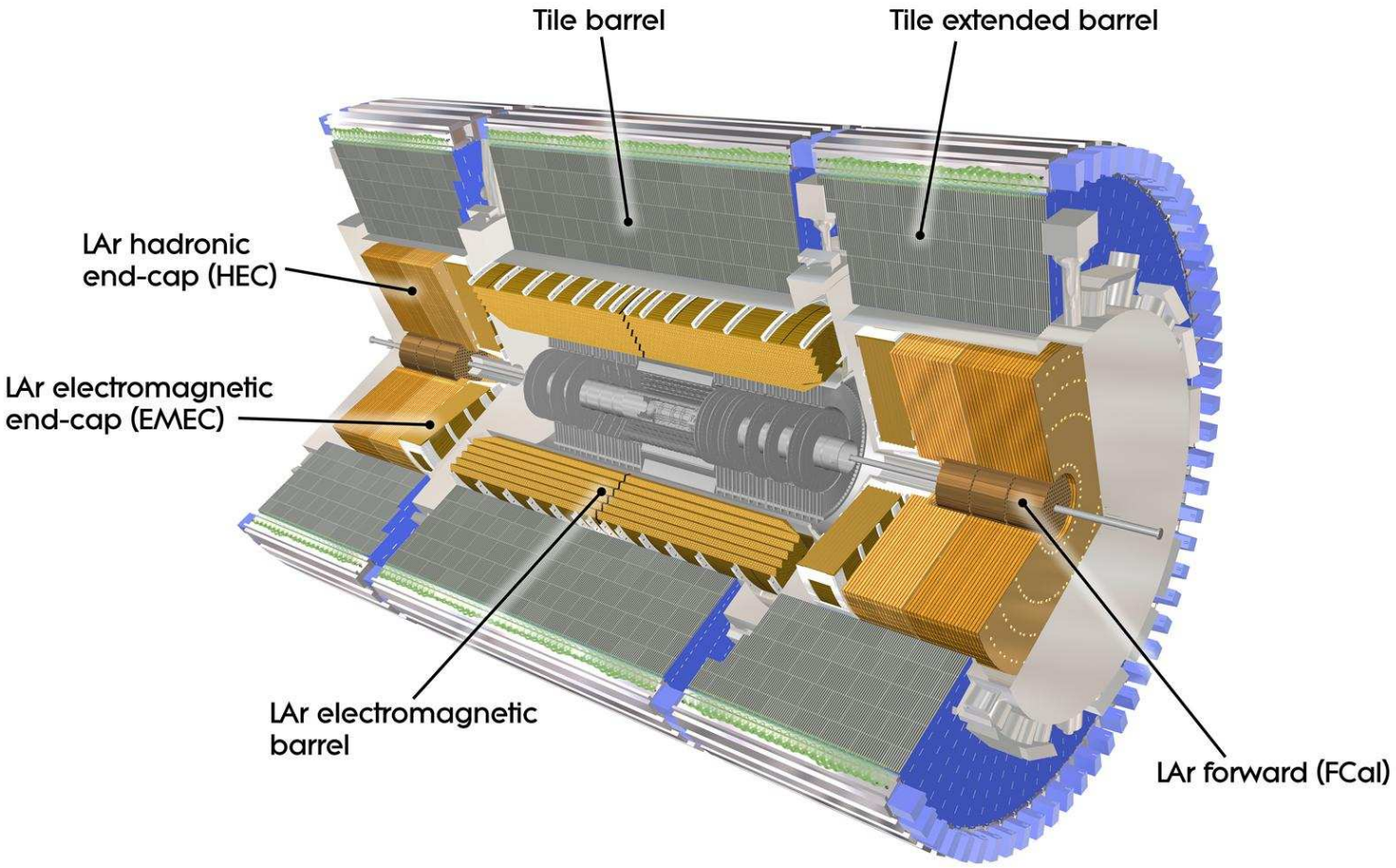

Figure 3.6: Schematic view of the ATLAS calorimeters [69]. The outer radius is about 4 m, while the extension along the beamline is 12 m.

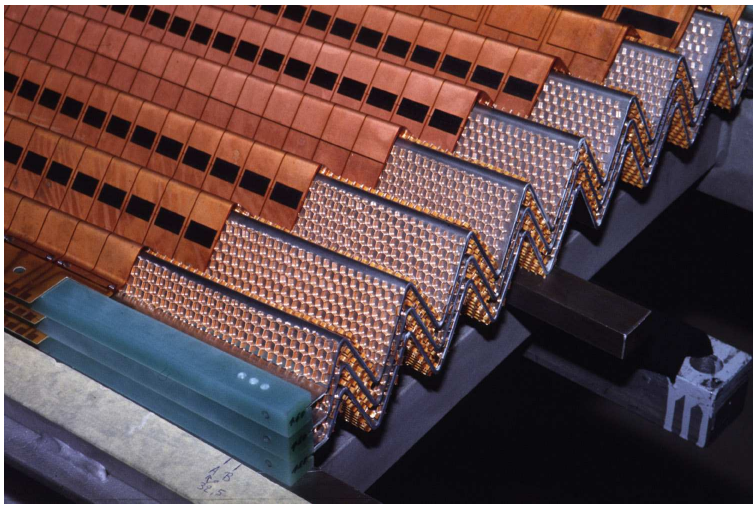

Figure 3.7: Accordion structure of the EM calorimeter [69].

The precision region is made up of three layers with different granularities in η and ϕ [72] (see Fig. 3.8). In η and depth the partition is achieved by etching the electrodes, in ϕ by bundling electrodes. The first layer consists of narrow strips, used for position measurements, that are very important e.g. for the determination of photon directions. Most of the energy is collected in the second layer, which is the deepest. The third layer has a very coarse granularity and is installed to absorb objects with very high energies. Underneath the three layers, for $|\eta| < 1.8$, a presampler, consisting of a thin layer of LArg, is used to estimate the energy lost in the Inner Detector. In order to keep the argon liquid, the barrel and the two endcaps are surrounded by cryostats, which cool the material down to 88 K.

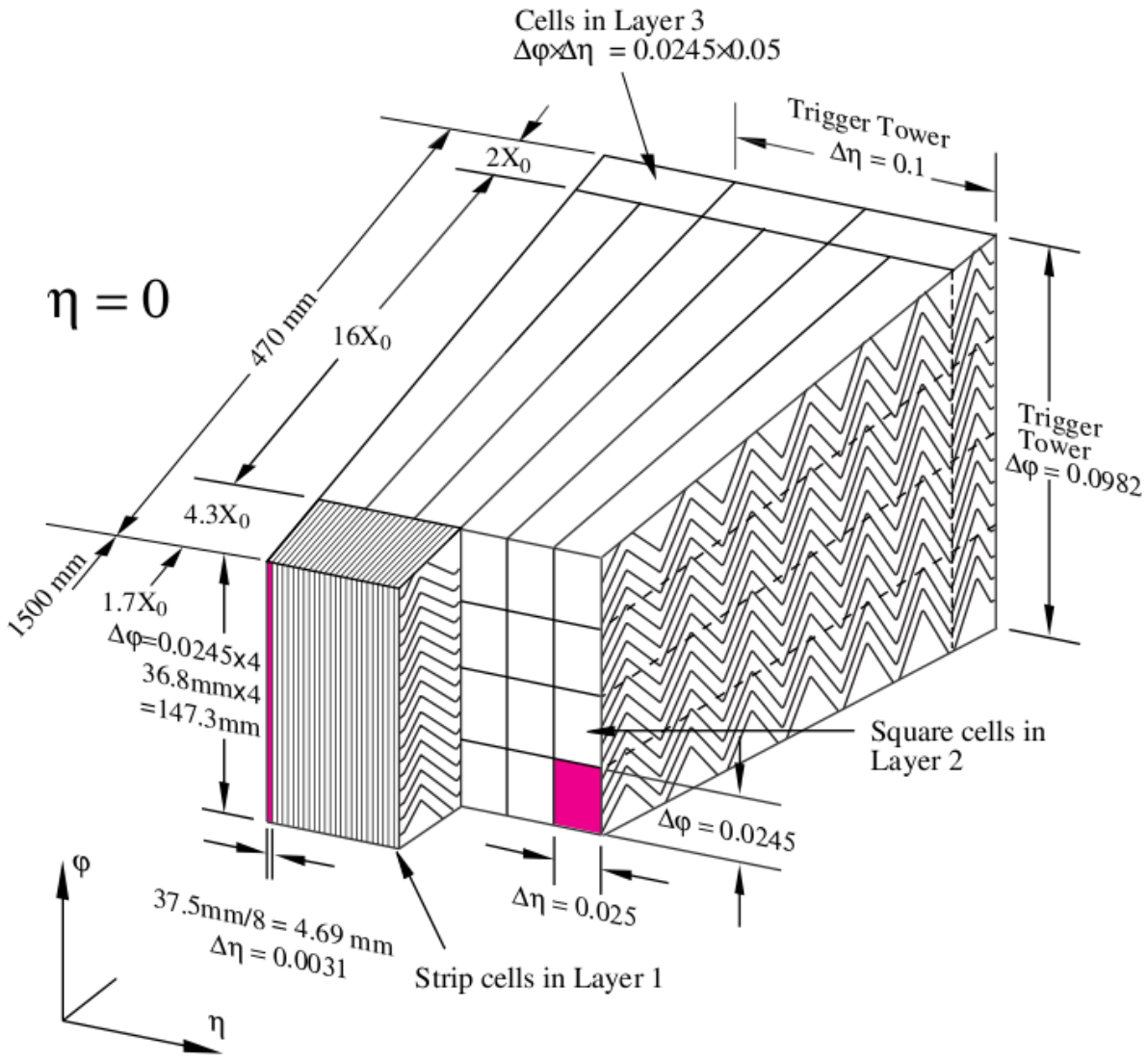

Figure 3.8: Barrel module, showing the different layers of the EM calorimeter [68]. X_0 describes the radiation length, which is the travel distance for a relativistic electron during which it loses all but $\sim 1/e$ of its original energy.

Chapter 4

Electrons in the ATLAS detector

In order to search for high-mass dielectron resonances, we look for central, highly energetic electrons, produced in pp collisions at the center of the ATLAS detector. Since electrons are charged, they leave a track in the Inner Detector (see Sec. 3.2.3 and 4.1). Furthermore, they deposit their energy across several cells in the EM calorimeter (compare Sec. 3.2.4 and 4.1). Since no interesting events should be missed, the electron trigger, reconstruction and identification efficiencies in ATLAS need to be high. On the other hand, many pp collisions contain hadronic jets, which can fake electron signatures in the detector and during reconstruction. These need to be rejected to reduce backgrounds and, in the case of the trigger, to decrease the amount of data to be processed and stored. This chapter describes how electrons in the ATLAS detector are triggered, reconstructed and identified.

4.1 $Z \to ee$ event display

Figure 4.1 illustrates the signature of a $Z \to ee$ event in the ATLAS detector [69]. Two different perspectives of the detector are shown, as well as a lego plot, which illustrates the

energy deposited in the EM calorimeter. The numbers denote various detector components:

1. Pixel detector
2. SCT
3. TRT
4. EM calorimeter
5. Hadronic calorimeter

The two electrons are depicted by the yellow pattern. The letters correspond to parts of the electron signature in the detector:

a) Tracking hits in the Inner Detector

b) TRT high threshold hits

c) Energy cluster in the EM calorimeter

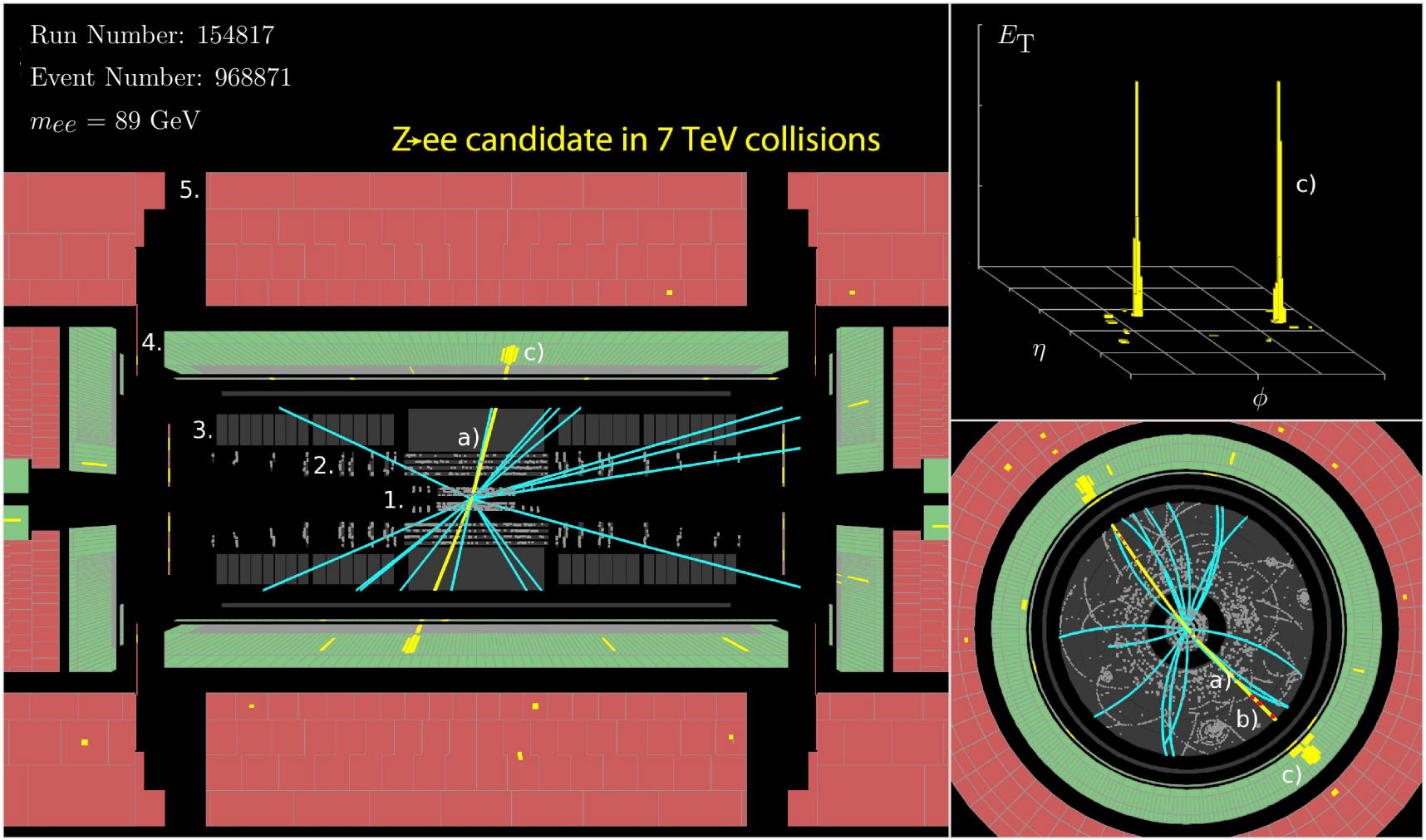

Figure 4.1: Event display of a $Z \to ee$ event [69]. Two different perspectives of the detector are shown (left, bottom right), as well as a lego plot (top right), which illustrates the energy deposited in the EM calorimeter.

4.2 Electron trigger

The purpose of the ATLAS trigger system is to filter 200 interesting events out of the 40 million pp collisions happening per second in the ATLAS detector (see Sec. 3.2.2). The trigger also does a first categorization, separating events with electrons and photons from events with muons or jets only.

The ATLAS trigger is an event selection system, consisting of three stages, L1, which reduces event rates of 40 MHz to 75 kHz, L2 (reduction to 3.5 kHz) and EF (reduction to 200 Hz). The triggers used in physics analyses are actually trigger chains, with one link for each trigger level. A menu of different cuts, called trigger items, exists at every stage. Here, only functionalities of the triggers that are used to select electron events are described. These triggers cover a range of $|\eta| < 2.5$.

4.2.1 Level 1 Calorimeter trigger

The first step in triggering electrons is the hardware-based Level 1 Calorimeter (L1Calo) trigger [73]. Since the time between two pp collisions is too short for a complete trigger decision, the data are pipelined, which makes it possible to have a trigger decision for every collision, albeit with a small latency (< 2.5 μs). To save processing time, the L1Calo trigger does not use the full granularity of the EM calorimeter. Instead, it performs analog sums over the three vertical layers and the cells, resulting in 3500 trigger towers with a dimension of $\Delta\eta \times \Delta\phi = 0.1 \times 0.1$ in the barrel middle layer (illustrated in Fig. 3.8). For every trigger tower, the recorded analog pulse is associated with a bunch-crossing of the LHC, corrections are applied and it is digitized, i.e. translated into an energy measurement. An L1 EM trigger item with a simple energy threshold is passed if there are two neighboring trigger

towers whose energies sum up to a value larger than the threshold. If the central 2×2 window passes at least one of the L1 trigger items, the 4×4 window around it is called the Region of Interest (ROI) and its coordinates are sent to the next level, the L2 trigger. Events without a region that passes any item of the L1 trigger menu are discarded.

4.2.2 High Level Trigger

The High Level Trigger (HLT) [74] is software-based and consists of L2 and EF. Since the time constraints are less stringent than at L1, the full granularity of the EM and hadronic calorimeters, as well as information from the Inner Detector can be used. Both levels employ a number of selection algorithms on the reconstructed energy clusters and tracks, similar to the offline identification cuts (see Sec. 4.4). For electrons, three baseline selections with increasing jet rejection capabilities (and decreasing efficiencies) are chosen: Loose, Medium, and Tight.

The L2 trigger receives the coordinates of the ROIs defined by L1. Using the full calorimeter granularity and starting from the cell with the highest energy in the ROI, it reconstructs the energy clusters. This reconstruction includes potential energy deposits in the hadronic calorimeter. The values of several variables describing the shape of the energy showers are determined, since these shower shapes differ for electrons and jets and can therefore serve as discriminants. Depending on the L2 trigger item, a number of cuts are applied on the shower shape variables. For reconstructing tracks as fast as possible, the IDScan algorithm first determines the z coordinate of the interaction vertex. Only tracks are reconstructed that point to the interaction vertex. Finally clusters and tracks are matched to each other to build L2 electron objects, and cuts can be applied on variables describing the quality of

the matching.

If at least one ROI passes the L2 trigger, the corresponding event is fully assembled using all available information from the different subdetectors. Thus the EF has access to the complete event, but usually only uses the ROIs provided by L2. Cluster and track reconstruction are the same as in the offline case (see Sec. 4.3). The situation is similar for the identification cuts (Sec. 4.4), however, unlike the offline cuts, the EF cuts are not E_{T} dependent.

4.3 Electron reconstruction

Central electrons ($|\eta| < 2.5$) are reconstructed by the standard e/gamma algorithm [75], which matches energy clusters in the EM calorimeter to tracks in the Inner Detector.

Electrons usually leave their energy in more than one calorimeter cell. The appropriate cell energies have to be combined into energy clusters [76]. The first part of the algorithm looks for seed clusters. The energies in the layers of the EM calorimeter are summed into towers of size 0.025×0.025 in η, ϕ (in the second layer) and a 3×5 window slides over these towers to find local energy maxima above a certain energy threshold. Using a smaller window, the position of the seed cluster is determined by finding the energy weighted center. If two clusters are too close to each other, only the one with the larger energy is kept.

Track reconstruction in ATLAS [77] is challenging due to the large amount of QCD multijet production in pp collisions. Two complementary tracking algorithms are used: The main algorithm starts with finding track seeds in the Pixel and SCT parts of the Inner Detector (see Sec. 3.2.3). A combination of global and local pattern recognition is applied and the tracks are extended to the TRT. For tracks without or with only a few hits in the

Pixel detector/SCT, a track finding algorithm starting from the TRT is used.

Tracks and energy clusters are matched to each other by extrapolating from the last track measurement point to the second layer of the EM calorimeter and then comparing the η, ϕ coordinates of this extrapolation with the coordinates of the seed clusters. If $\Delta\eta < 0.05$ (this cut is only applied to tracks with hits in the Pixel detector/SCT) and $\Delta\phi < 0.05$, a track is matched to a cluster. Possible bremsstrahlung (electrons radiating photons while accelerating, losing energy and therefore being bent more by the magnetic field), which might affect the quality of the extrapolation, is accounted for by allowing $\Delta\phi < 0.1$ in the direction where the track is bent. If more than one track is matched to a given cluster, all matched tracks are kept, and the one with the smallest ΔR is considered the best match. Tracks with silicon hits are preferred over tracks without, since the latter are more likely to come from photon conversions (photons converting into an electron-positron pair).

Energy clusters with matched tracks are considered electron candidates. For each candidate, the cluster is recomputed with an optimized cluster size, separately for each layer, starting with the coordinates of the seed cluster [77]. All cells in a 3×7 window (in middle layer cell units) are considered part of the cluster. Energy corrections are applied. The electron candidate's 4-momentum is calculated by taking the energy from the cluster and its direction from the best matched track, if this track contains hits in the Pixel detector/SCT. If not, the η, ϕ coordinates of the cluster are used.

4.4 Electron identification

Among the reconstructed electron candidates are not only electrons from the processes we are interested in, but also jets, electrons from conversions, and electrons from pion decays,

which can all leave tracks in the Inner Detector and energy clusters in the calorimeters. Additional algorithms are needed to reduce this background.

Electron identification [75, 34] in ATLAS is done by applying a number of cuts on the shapes of the showers in the EM calorimeter, on the tracks in the Inner Detector and on the matching between clusters and tracks. This is effective, since jets tend to have wider showers than electrons, as well as more tracks. Conversions and electrons from pion decays are usually produced a bit off the center of the detector, and therefore can miss the first layers of the Inner Detector. The TRT can help with particle identification by measuring the transition radiation of relativistic particles (see Sec. 3.2.3).

The identification cuts have been optimized to allow for the best possible electron efficiencies while maintaining high rejection rates for QCD jets. As part of the optimization, the cuts are binned in η and E_{T} of the electron candidates. The cuts are binned in E_{T} because the showers for both jets and electrons are narrower at higher energies. Both shower shapes and tracks in the Inner Detector depend on the amount of material the electrons have to traverse, which makes binning in η necessary. Harmonized with the triggers, three reference cut sets are defined, Loose, Medium, Tight, with increasing jet rejection from Loose to Tight.

The Loose cut set relies on cuts on shower shape variables in the middle layer of the EM calorimeter and on a cut on the energy leakage into the hadronic calorimeter. On top of that, the Medium set includes cuts on the shower shapes in the first layer of the EM calorimeter, as well as track quality cuts and cuts on the track matching. The Tight set applies more stringent cuts on the track matching and on the track quality; furthermore cuts on the TRT hits are added, including cuts on the high threshold hits, which come from transition radiation.

An overview of the different cuts used for electron identification in ATLAS is given in Table 4.1 [75, 34].

Type of cut	Description
Loose	
Middle layer of EM calorimeter	Ratio of the energy in 3×7 cells to the energy in 7×7 cells centered at the electron cluster position
	Width of the shower in η
Hadronic leakage	Ratio of E_{T} in the first layer of the hadronic calorimeter to E_{T} of the EM cluster (used over the range $\lvert\eta\rvert < 0.8$ and $\lvert\eta\rvert > 1.37$)
	Ratio of E_{T} in the hadronic calorimeter to E_{T} of the EM cluster (used over the range $\lvert\eta\rvert > 0.8$ and $\lvert\eta\rvert < 1.37$)
Medium (in addition to Loose cuts)	
First layer of EM calorimeter	Total shower width
	Ratio of the energy difference between the largest and second largest energy deposits in the cluster over the sum of these energies
Track quality	Number of hits in the Pixel detector (≥ 1)
	Number of total hits in the Pixel detector/SCT (≥ 7)
	Transverse impact parameter ($\lvert d_0\rvert < 5$ mm)
Track-cluster matching	$\Delta\eta$ between the cluster position in the first layer of the EM calorimeter and the matching extrapolated track ($\lvert\eta\rvert < 0.01$)
Tight (in addition to Medium cuts)	
Track-cluster matching	$\Delta\phi$ between the cluster position in the middle layer and the matching extrapolated track ($\Delta\phi < 0.02$)
	Ratio of the cluster energy to the track momentum
	Tighter $\Delta\eta$ requirement ($\Delta\eta < 0.005$)
Track quality	Tighter transverse impact parameter cut ($\lvert d_0\rvert < 1$ mm)
TRT	Total number of hits in the TRT
	Ratio of the number of high-threshold hits to the total number of hits in the TRT
Against conversions	Number of hits in the first layer of the Pixel detector (≥ 1)
	Veto electron candidates matched to reconstructed photon conversions

Table 4.1: Description of the electron identification cuts [75, 34].

4.5 Electron isolation

In addition to the electron identification cuts, it is possible to require the tracks and/or the calorimeter cluster of the electron candidate to be isolated [75]. This allows for an enhanced rejection of QCD jets, which usually consist of a bundle of tracks and wide clusters. In the case of track isolation, a cut is applied on the sum of the scalar p_{T} of the tracks that fall into a cone with an opening angle R around the electron. For calorimeter isolation, the E_{T} deposited in the EM and hadronic calorimeters in a cone around the electron is summed up. Of course, the E_{T} of the electron cluster itself is subtracted. Corrections are applied to account for pile-up effects (see Sec. 5.3.4) and energy in the cone that actually belongs to the electron. As this leaked energy is E_{T} dependent, so are the corrections.

4.6 Performance of electrons with high E_{T}

The performance of electrons in ATLAS, i.e. the efficiency and quality of electron triggers, reconstruction and identification, has been studied very well. The focus of these studies has been on electrons with E_{T} up to around 100 GeV, due to feasibility and physics analyses' needs: Most electrons from low mass Higgs, $W$and Z bosons as well as top quark decays have energies below 100 GeV. However, in this analysis, we look for signatures with mass peaks up to 2 TeV. The electrons from these resonances can have transverse energies above 500 GeV and we need to understand their properties in order to detect them efficiently and correctly reconstruct their energies. Furthermore we have to make sure that we can control the background from QCD jets faking electron signatures.

Studies of the properties of high E_{T} electrons in ATLAS data are very challenging because

of low statistics and the difficulty of obtaining a clean electron sample in data without jet contamination. At lower energies, this is achieved using the characteristic decays of Z and W bosons (see App. A), but at high energies no such handle is available and most studies rely on calibration runs and simulations.

4.6.1 Energy reconstruction

The energy resolution at sampling calorimeters [78] can be parameterized as

$$\sigma(E)/E = a/\sqrt{E} \oplus b/E \oplus c, \tag{4.1}$$

where $\oplus$ represents addition in quadrature, and E is the energy in GeV. The first term is stochastic, the second one is due to pile-up and electronic noise and the third is the constant term. The constant term is the result of imperfect reconstruction of the cluster energies, which can happen because of unaccounted energy deposits in the Inner Detector or other calibration issues. At high energies, the constant term dominates the resolution, and a lot of work has been done to decrease it. For $|\eta| < 1.37$, the constant term (and therefore the resolution for highly energetic electrons) has been measured in data at transverse electron energies of ∼50 GeV to be 1.1%, while for $1.52 < |\eta| < 2.47$, it is 1.8%, a bit larger due to additional material in front of the calorimeter. Calibration runs, using electronic pulses, showed that high energy signals up to 2 TeV do not cause unexpected deterioration of the resolution [79]. Figure 4.2 shows the effect of the electron resolution on the dielectron invariant mass peaks of the Z'_{SSM} boson and the Z'_{χ} boson assuming a peak mass of 1.5 TeV. Thanks to the excellent electron resolution, after reconstruction, the two models can still be distinguished due to their shape.

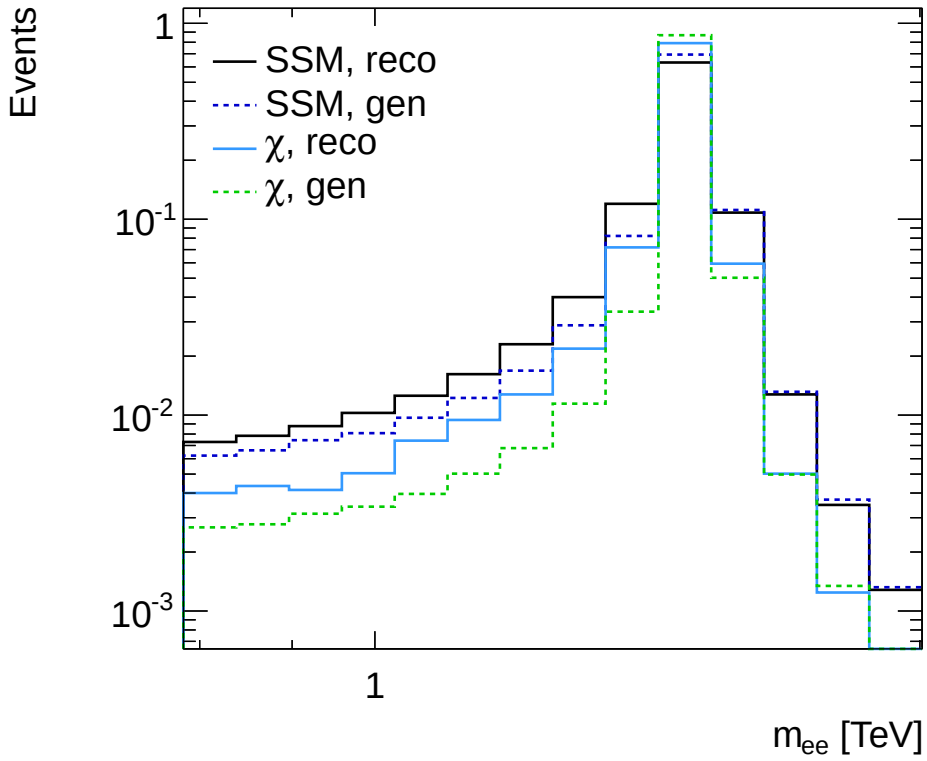

Figure 4.2: Simulated dielectron invariant mass distribution of the Z'_{SSM} boson and the Z'_{χ} boson for an assumed peak mass of 1.5 TeV. The distributions are normalized to unit area and shown before ("gen") and after electron reconstruction and application of event selection cuts ("reco", see Sec. 6.1 for a description of the selection cuts).

The uncertainty on the absolute energy scale in ATLAS ranges from 0.5-1.5%, depending on E_{T} and η [80]. Again, calibration runs using pulses with a wide variation of energies have been employed to determine the linearity of the electronic response and its effect on the energy reconstruction. Nothing problematic has been seen throughout the range of tested energies (up to 2 TeV) [79].

4.6.2 Bunch-crossing identification

The L1Calo trigger (Sec. 4.2) saturates if the transverse energy per trigger tower is larger than 255 GeV [73]. In principle, this is not a problem since every event with a saturated

L1Calo signal automatically passes the trigger. However, the identification of the correct LHC bunch-crossing depends on the shape of the analog pulse, so it could be impacted by the saturation [81]. If the saturated signal from a high E_{T} electron is associated with a bunch-crossing too early or too late, the wrong event will be triggered, and therefore the trigger efficiency will be decreased for events with highly energetic objects. Dedicated algorithms for saturated signals have been employed to deal with this issue [81]. Preliminary studies in 2011 show no inefficiency for energies up to 3 TeV in the barrel ($\eta < 1.37$), and up to 2.1 TeV in the calorimeter endcaps.

4.6.3 Trigger and identification efficiencies

Trigger and identification efficiencies for electrons with E_{T} below ∼100 GeV can be determined from data by applying the Tag-and-Probe method on Z boson decays (this is documented in detail for identification efficiencies in App. A). In this energy range, Tag-and-Probe studies show rising efficiencies in E_{T}. However, at higher energies, the Tag-and-Probe method suffers from low statistics and cannot be used reliably any more. One important alternative is to study efficiencies in simulated samples.

The identification criteria chosen for this analysis are the Medium set (see Table 4.1) and two additional cuts: the requirement of a hit in the innermost layer of the Pixel detector (B-layer) to reject electrons from photon conversions and a cut on the calorimeter isolation (see Sec. 4.5) to decrease the background due to QCD jets.

Fig. 4.3(a) shows the efficiency of these cuts with respect to reconstructed electron candidates in bins of E_{T}. A simulated sample of Z' events is used for this study. No efficiency decrease with E_{T} is expected for the selection according to the simulation. This can be

understood by looking at the details of the cuts: Since highly energetic electrons tend to have more focused showers (the momentum in the direction of flight dominates), the shower shape cuts are actually less stringent than at low E_{T} (for this reason the cuts are binned in E_{T}, though the highest E_{T} bin starts at 80 GeV). The energy leakage into the hadronic calorimeter is expected to be larger for high E_{T} electrons, but the applied cut (compare Table 4.1) is a ratio cut, thus no efficiency should be lost. The track cuts are not expected to cause problems with increased energy either. As can be seen in Fig. 4.3(b), the B-layer cut actually becomes more efficient with higher E_{T}. However, this efficiency gain is cancelled by the isolation requirement, whose efficiency drops slightly with rising E_{T}. This is due to imperfect leakage corrections (compare Sec. 4.5).

The trigger chain used in this analysis is L1_EM14 - L2_e20_medium - EF_e20_medium. Figure 4.4 shows that the efficiency for this trigger with respect to the electrons used in this analysis is very high ($\sim$99%), and flat in E_{T}.

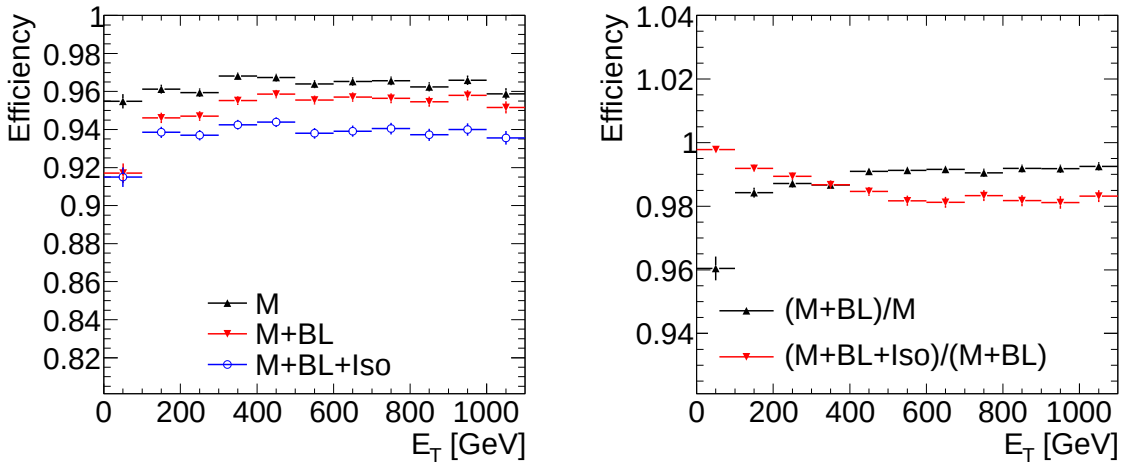

(a) (b)

Figure 4.3: Identification efficiency with respect to reconstructed electrons as a function of E_{T}. M = Medium, BL = B-layer and Iso = isolation requirements. (b) shows the effects of the B-layer and isolation cuts individually. Both plots are made with a simulated "flat" Z' sample (see Sec. 5.2.2) and integrated over η between -2.47 and 2.47, excluding the transition region between barrel and endcap calorimeters.

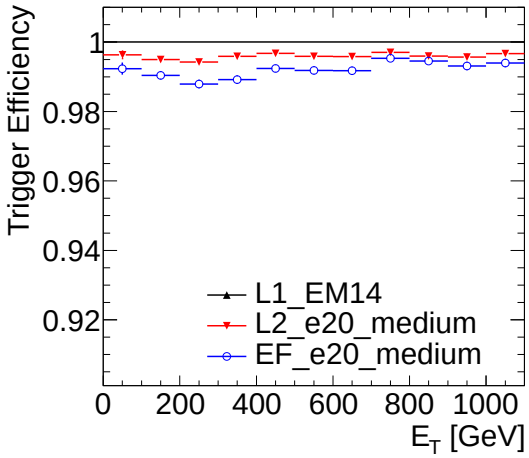

Figure 4.4: Trigger efficiency with respect to the electrons used in this analysis as a function of E_{T}. The plot is made with a simulated "flat" Z' sample (see Sec. 5.2.2) and integrated over η between -2.47 and 2.47, excluding the transition region between barrel and endcap calorimeters.

Chapter 5

Simulation of signal and background processes

In this analysis, we are looking for a resonance in high-mass electron pairs. In order to estimate the SM background, it is important to understand which SM processes can produce the same signature (two reconstructed electrons) in the detector. This chapter describes the simulated signal and background samples, as well as data-driven corrections, which need to be applied to them to increase the quality of the modeling.

5.1 Standard Model backgrounds

The largest, irreducible background in this analysis is the DY process, the production of a Z boson or an excited photon which then decays into an electron and a positron (compare Sec. 2.1.4, Fig. 2.1 and 2.4).

All other backgrounds are smaller than the DY process by at least a factor of ten:

- Diboson production, the production of two Z bosons, two W bosons or one Z and one W boson, can lead to a dielectron final state, if one (in case of a Z boson) or two (in case of WW production) bosons decay into electrons.

- The same is true for $t\bar{t}$ production, the simultaneous production of a top and an antitop quark. Both top quarks decay into a bottom quark and a W boson. If both W bosons decay into electrons (and neutrinos), the event has a dielectron final state.

A second class of backgrounds involves the misidentification of QCD jets as electrons:

- A W boson can be produced in association with one or more jets. The electron from the W boson and one of the jets could be misinterpreted as an electron pair.

- Because the LHC collides protons at very high energies, a large fraction of events contains multiple QCD jets. Two jets which are wrongly reconstructed and identified as electrons contribute to the SM background as well.

Dedicated electron identification and isolation requirements are applied (compare Sec. 4.4 and 6.1), which reduce the background from misidentified QCD jets very efficiently. However, a non-negligible fraction survives these cuts, since the cross-sections for W + jets and QCD multijet production are very large.

5.2 Samples

In this analysis, all SM backgrounds, except for the QCD multijet production, are taken from simulated samples. The background contribution from QCD multijets is estimated from data (see Chapter 6.2), as a huge number of QCD multijet events would have to be

simulated, given the small rate of jets misidentified as electrons. Furthermore, there is a large uncertainty on the simulation of the misidentification rate itself.

5.2.1 Event generators

Simulated samples are made with event generators, computer programs that produce final states of a chosen number of particle collisions for a variety of physics processes. These event generators receive probabilities as input: The PDFs, as well as the Feynman diagrams for given physics processes (see Sec. 2.1.3). They simulate the final state particles and their properties by integrating over the allowed phase space using a random number sampling (Monte Carlo).

A number of event generators have been developed with different strong and weak points. Pythia [46] and Herwig [82] are general purpose generators, starting from LO matrix elements. They include the decays of particles and apply corrections due to beam remnants, electroweak and QCD radiation. The latter is often described as showering, since one emitted parton can result in a large number of hadrons. Alpgen [83] does not solely rely on dressing up the LO process with showers, but calculates the matrix elements individually for different jet multiplicities. This is important for realistic modeling of hard parton radiation. MC@NLO [84] combines the additional processes in a more consistent way than Alpgen and includes matrix elements for all next-to-leading order (NLO) processes that contain real gluon or quark emissions and virtual particle loops.

In order to compare the simulated final states with real data, the detector response must be replicated as well. For this, ATLAS feeds the output of the event generators into a detector simulation program called Geant4 [85], which propagates the final state particles

through the detector. For example, electrons are translated into hits in the Inner Detector and energy deposits in the calorimeters.

5.2.2 Samples and cross-sections

Table 5.1 shows simulated samples of the SM processes used for the background estimates in this analysis. The table also contains the production cross-section σ times the branching ratio B which corresponds to the fraction of events decaying into two electrons.

In order to calculate the expected event yield N of a given process,

$$N = \sigma B A L_{int}, \tag{5.1}$$

the following ingredients are needed:

- The production cross-section σ.
- The branching fraction of events B decaying into the final state we are interested in, for example two electrons.
- The acceptance, which is the fraction of produced events recorded by the ATLAS detector. This is usually not one, due to kinematic cuts and inefficiencies in particle detection (see Sec. 4.6.3).
- The integrated luminosity L_{int} - the number of pp collisions, corresponding to the integral of the instantenous luminosity: $L_{int} = \int L dt$ (compare Sec. 3.1).

With the exception of the $t\bar{t}$ process, all samples are simulated at LO, using a PDF set called MRST2007lomod [19] (CTEQ6.1 [86] for W+jets). The $t\bar{t}$ sample is produced at NLO

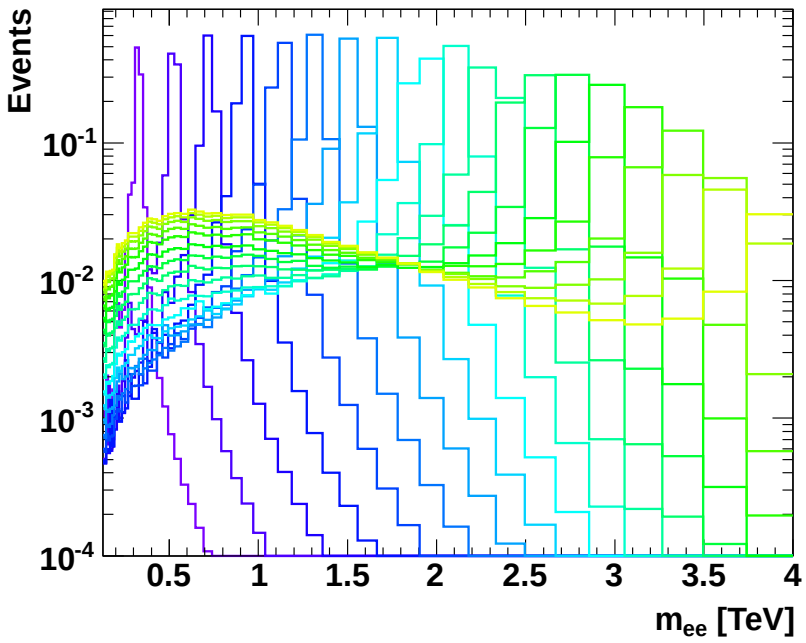

Figure 5.1: Reweighted invariant mass distributions for different masses of the Z'_{SSM} boson. The histograms are all normalized to unit area.

with the CTEQ6.6 PDF [87]. However, the overall cross-sections are scaled to the highest known order: NLO for dibosons, NNLO for $W+$jets and approximate NNLO for $t\bar{t}$ [88, 89]. The DY as the dominant background is corrected using mass-dependent correction factors (see below).

Table 5.2 and 5.3 show a representative selection of possible signal processes and their cross-sections. All signal samples are produced at LO with Pythia and interference between Z' production and the DY process is neglected. For the Z' process, instead of separate signal samples, we use a sample which is flat in bins of dielectron mass. To produce this sample, the Breit-Wigner resonance curve and exponential cross-section drop due to parton luminosities were removed. It can be reweighted to obtain the dielectron mass distribution for any given Z' mass (see Fig. 5.1).

In order to improve the LO estimate for the DY process as the dominant SM background,

Process	Generator	Order	Filter	Binning	Bins	σB [pb]
DY	PYTHIA	LO	2 electrons	m_{ee} [GeV]	> 60	856
					75-120	819.9145
					120-250	8.711065
					250-400	0.415835
					400-600	0.067136
					600-800	0.011168
					800-1000	$2.7277 \cdot 10^{-3}$
					1000-1250	$9.1646 \cdot 10^{-4}$
					1250-1500	$2.4942 \cdot 10^{-4}$
					1500-1750	$7.6876 \cdot 10^{-5}$
					1750-2000	$2.6003 \cdot 10^{-5}$
					> 2000	$1.5327 \cdot 10^{-5}$
Dibosons	HERWIG	LO	1 electron/ muon	process	WW	17.46
					WZ	5.543
					ZZ	1.261
$W +$ jets	ALPGEN	LO	1 electron	jets	1	1551.6
					2	452.5
					3	121.1
					4	30.4
					5	8.3
$t\bar{t}$	MC@NLO	NLO	2 electrons	m_{ee} [GeV]	30-150	3.0240
					150-300	0.34669
					300-450	0.028965
					> 450	$4.81 \cdot 10^{-3}$

Table 5.1: List of background samples. The DY cross-sections are shown at LO, while the cross-sections of the other background samples are scaled to the highest available order.

correction factors are calculated as a function of the dielectron invariant mass [90]. These k-factors are determined for NNLO QCD corrections (gluon loops and radiation) as well as for electroweak corrections. PYTHIA already includes photon emissions, thus the additional corrections that are accounted for are gauge boson loops. Gauge boson emissions are not included, which results in an underestimate of the DY cross-section of 2%. Since the electroweak k-factor depends on the coupling of W and Z bosons to the exchange particle, only the QCD k-factor can be applied to Z' production, assuming that slightly different couplings

Mass [GeV]	$\sigma B(Z'_{\mathrm{SSM}})$ [pb]	$\sigma B(Z'_{\chi})$ [pb]	$\sigma B(Z'_{\psi})$ [pb]
250	27.35	15.89	8.132
500	2.038	1.163	0.5968
750	0.3668	0.2101	0.1069
1000	0.09477	0.05183	0.02690
1250	0.02960	0.01556	$8.171 \cdot 10^{-3}$
1500	0.01033	$5.064 \cdot 10^{-3}$	$2.732 \cdot 10^{-3}$
1750	$3.876 \cdot 10^{-3}$	$1.747 \cdot 10^{-3}$	$9.833 \cdot 10^{-4}$
2000	$1.579 \cdot 10^{-3}$	$6.410 \cdot 10^{-4}$	$3.706 \cdot 10^{-4}$
2250	$6.935 \cdot 10^{-4}$	$2.493 \cdot 10^{-4}$	$1.422 \cdot 10^{-4}$
2500	$3.296 \cdot 10^{-4}$	$1.044 \cdot 10^{-4}$	$5.668 \cdot 10^{-5}$

Table 5.2: LO cross-sections for the Z'_{SSM} and some of the E_6 models [90]. The generator is Pythia, a dielectron filter is applied and interference between the Z' and DY is neglected.

Mass [GeV]	$\sigma B(k/\bar{M}_{Pl} = 0.01)$ [pb]	$\sigma B(k/\bar{M}_{Pl} = 0.1)$ [pb]
300	0.5216	-
500	0.04046	-
800	$2.996 \cdot 10^{-3}$	0.2982
1000	$0.7839 \cdot 10^{-3}$	0.07734
1250	-	0.01838
1500	-	$5.288 \cdot 10^{-3}$

Table 5.3: LO cross-sections for the RS graviton with different values of $k/\bar{M}_{Pl}$ [90]. The generator is Pythia and a dielectron filter is applied.

to the initial state quarks do not change the correction. No higher order correction factors are currently available for RS graviton production [91, 92]. Table 5.4 shows values of the correction factors for different invariant masses for samples produced with the MRST2007lomod PDF [19].

m_{ee} [GeV]	500	750	1000	1250	1500	1750	2000
k^*_{QCD}	1.131	1.109	1.080	1.041	0.990	0.929	0.860
k^*_{EW}	1.032	1.016	1.000	0.986	0.971	0.956	0.941

Table 5.4: Higher order QCD and electroweak (EW) correction factors [90] for DY samples produced with the MRST2007lomod PDF [19].

5.3 Corrections to the simulated samples

The simulation of electrons and their signatures in the ATLAS detector is in good agreement with results obtained from real data. The main reason for imperfect modeling of electron signatures is missing knowledge of the exact distribution of material in the ATLAS detector [93]. An example is the modeling of electron shower shapes. Discrepancies were found between data and simulation of electron shower widths. These differences are largely due to a simplified description of the absorber layers in the EM calorimeter: Instead of the actual sandwich structure iron-glue-lead-glue-iron, the simulation assumes a homogenous mixture of materials.

The difference in shower widths affects the efficiency of the identification cuts, as some of these cuts are applied on shower shape variables (compare Table 4.1). In order to do a fair comparison between data and simulation, this efficiency discrepancy needs to be corrected for using scale factors applied to simulated samples. A description of these and other necessary corrections to the simulated samples is described in the following sections.

5.3.1 Efficiencies

The imperfect description of the detector in the simulation causes small differences between data and simulated samples concerning electron trigger, reconstruction and identification efficiencies. In order to correct this and allow for an unbiased comparison between data and simulated signal and SM backgrounds, scale factors (SF) are calculated as the ratio between the efficiencies (ϵ) for true electrons in data and in the simulated samples:

$$\text{SF} = \frac{\epsilon \text{ in data}}{\epsilon \text{ in simulation}}. \tag{5.2}$$

To account for changes of the efficiency in different regions of the detector and for electrons with various energies, the SF are binned in η and E_{T}.

The biggest challenge in the efficiency measurement consists of getting a sample of electrons from data on which to perform the efficiency determination. This sample should consist of real electrons, not QCD jets, and no cuts should be applied to these electrons that could bias the efficiency measurement. The method of choice is the Tag-and-Probe method, which makes use of the characteristic signatures of the $Z \to ee$ and $W \to e\nu$ decays. In the case of $Z \to ee$ Tag-and-Probe, very strict cuts are applied on one of the two decay electrons (called "Tag"), and the second electron candidate ("Probe") is used for the measurements. Additional cuts, which ensure that the invariant mass of the two objects is close to the Z boson mass, and that the two electrons have opposite charge, greatly enhance the chance that the second, unbiased electron candidate is a real electron. The Tag-and-Probe method is described in detail in App. A.

5.3.2 Energy resolution

For electrons with high E_{T} the constant term dominates the energy resolution parametrization (see Eq. 4.1 in Sec. 4.6.1). The constant term used in the simulated samples is smaller than what can currently be achieved by detector calibration in data, which means the energy of each simulated electron needs to be varied according to a Gaussian distribution in order to artificially worsen its energy resolution. The parameters for this Gaussian smearing are obtained by comparing the mass peak of the Z boson as measured in data with the one obtained from a simulated $Z \to ee$ sample [34].

5.3.3 Calorimeter electronics

For a fraction of the data taking period, a small region (0.8%) of the EM calorimeter (Sec. 3.2.4) was not functioning. Since it is not possible to correctly reconstruct the energy of electrons falling into or close to the problematic region, these electrons are not considered in this analysis. The whole EM calorimeter is assumed to be working in the simulation, which means the detector acceptance is overestimated. In order to be able to compare kinematic distributions and achieve the same electron acceptance in the simulation as observed in data, electrons passing the problematic region must not be considered. This should happen only for a fraction of each simulated sample, which corresponds to the fraction of corrupted data.

5.3.4 Pile-up

The LHC collides protons at higher rates than any other accelerator before. Collision rates of 40 MHz can only be achieved if the protons are concentrated in dense bunches, and if these bunches cross each other at very high frequencies (compare Sec. 3.1.2). A side effect of high

proton densities in the beam is that multiple protons might collide in one bunch-crossing and that collisions from subsequent bunch-crossings can overlap in the detector. These effects are called in-time and out-of-time pile-up respectively. Over the whole data-taking period, in order to provide as much data to the experiments as possible, the LHC was continuously increasing the collision rates, and therefore also the pile-up.

The simulations include pile-up; however, the conditions are not exactly the same as in data since the increase of collision rates was not completely known at the time the simulated samples were made. Since the amount of pile-up can affect the electron reconstruction and identification efficiency, the simulated samples have to be reweighted to contain the same fraction of events with a given amount of pile-up as the data.

Chapter 6

Event selection and comparison with Standard Model expectations

This chapter describes how the data used in this analysis are selected. Selection cuts, filtering events with two reconstructed electrons that pass identification cuts, are applied to data as well as to simulated signal and SM background samples. The QCD multijet background is estimated from data by reversing electron identification cuts. The invariant mass distribution is calculated and the observed data counts are compared to the expected SM backgrounds. Other kinematic distributions are compared as well to ensure good modeling of the SM backgrounds.

6.1 Event selection

This analysis uses LHC collision data obtained by the ATLAS detector between March and June 2011. Only collisions are considered during which the LHC beam quality is good and the necessary parts of the ATLAS detector are functioning. This amount of data corre-

sponds to an integrated luminosity of 1.08 fb^{-1}, which can be translated into one event of a hypothetical process with a cross-section of 1.08 fb or ∼1 million Z bosons decaying into electrons. In order to find a dielectron resonance, events are selected that contain two electron candidates. This section describes the selection cuts that enhance the probability for the electron candidates to be real electrons. Unless noted otherwise, the same selection cuts are applied to data and the simulated signal and SM background samples.

6.1.1 Event selection

- Data quality

  Only collision data are used that have been recorded when the protons in the LHC beams are circulating in a stable orbit and are well focused, in order to avoid stray protons or other beam radiation faking collision events in the detector. For data used in an electron analysis, it is required that the calorimeters and the Inner Detector are functioning at the time of collisions, and that the solenoidal magnetic field is switched on, since it is needed for the momentum determination of the particles in the Inner Detector. Furthermore, no irregularities in the e/gamma trigger performance (like sudden rate drops) are allowed.

- Vertex

  Only events in which there is at least one reconstructed collision point with more than two tracks in the Inner Detector are used.

- Trigger

  Events are selected if they pass the trigger EF_e20_medium (compare Sec. 4.2). This means they were recorded because they have at least one electron candidate with

$E_{\mathrm{T}} > 20$ GeV.

- Two reconstructed electrons

  Since we are looking for dielectron resonances, we only want events with at least two electron candidates reconstructed by the standard e/gamma reconstruction algorithm, which is seeded by an energy cluster in the EM calorimeter (see Sec. 4.3).

The following selection cuts are applied to all electron candidates in the event; only electron candidates that pass the previous cuts are considered at each stage. Events which have less than two electron candidates fulfilling all requirements are discarded.

- η

  The Inner Detector can only detect tracks up to $|\eta| < 2.5$ (compare Sec. 3.2.3), therefore a selection cut of $|\eta| < 2.47$ is applied to the electron candidates. Furthermore, electrons are rejected which fall into the transition regions ($1.37 < |\eta| < 1.52$) between the barrel and the endcap of the EM calorimeter (Sec. 3.2.4), since the energy reconstruction in these areas is not very accurate.

- E_{T}

  A selection cut of $E_{\mathrm{T}} > 25$ GeV is applied to the electron candidates to be consistent with the trigger. Since we are looking for high-mass resonances, in principle the E_{T} cut could be far higher but the mass peak of the Z boson is used for normalization and as a sanity check, thus electrons coming from the Z boson decay (most of which fulfill $30 \lesssim E_{\mathrm{T}}\ [\mathrm{GeV}] \lesssim 60$) should be kept. Before the E_{T} cut is applied, the energy of the electron candidates in data is calibrated by corrections which are obtained comparing

the Z boson mass peak to the prediction [34]. Energy smearing in the simulated samples is described in Sec. 5.3.2.

- Electron quality

  Electron candidates are not considered if they fall into problematic regions of the EM calorimeter. Which regions are problematic changes with time, due to hardware problems like broken electronics as well as irregularities in the applied voltage [94]. The treatment of these time-dependent selection cuts in the simulated samples is described in Sec. 5.3.3.

  In addition, we reject events that contain corrupt event data or obvious electronic malfunctions, like noise bursts which illuminate a large fraction of the cells in the EM calorimeter.

- Identification

  In order to enhance the probability that electron candidates are real electrons, they are required to pass the Medium identification cuts (compare Sec. 4.4).

- B-layer

  To avoid electrons from photon conversions, we require that electrons have a tracking hit in the innermost layer of the Pixel detector (B-layer).

In events with more than two electrons at this stage of the selection cut flow, the two electrons with the highest E_{T} are chosen.

- Isolation

  In order to reduce the fraction of electron fakes from QCD multijet production, the energy cluster of the leading electron (the electron with the highest E_{T}) must be

isolated (compare Sec. 4.5). We require that the E_{T} in a cone of $\Delta\mathrm{R} < 0.2$ around the electron is less than 7 GeV. Corrections are applied accounting for pile-up effects and energy in the cone that actually belongs to the electron. Since the subleading electron often has less energy because it lost a fraction due to radiation, it usually is less isolated and we do not require it to pass the isolation cut.

- Invariant mass

  The invariant mass of the two electrons is calculated by taking the square root of the square of the sum of the two electron 4-momenta and is required to be above 70 GeV. The threshold is chosen to be below the Z boson mass peak ($\sim$91 GeV) as mentioned above.

6.1.2 Cutflows and acceptance

Table 6.1 shows the number of events passing the different selection cuts for data and for a simulated Z'_{SSM} sample ($\mathrm{m}_{Z'} = 1500$ GeV). The absolute efficiencies of the cuts as applied to the signal sample are shown as well. The event numbers for the simulated sample contain all corrections as described in Sec. 5.3, and they are weighted to an integrated luminosity of 1.08 fb^{-1}.

After applying the event selection cuts to the data, 266543 events are left, as shown in Table 6.1. Figure 6.1 illustrates the event with the highest dielectron invariant mass ($m_{ee} =$ 993 GeV). In this event, the E_{T} of the two electrons is 257 and 207 GeV respectively. The (η, ϕ) values for the leading electron are (-0.76, 1.14), for the subleading electron (2.05, -2.05).

Selection cuts	Data	Z'_{SSM} + DY ($m_{ee} > 750$ GeV)	eff(Z'_{SSM} + DY)
Before cuts	152750511	16.53	1.00
Data quality	132525884	16.53	1.00
Vertex	132399372	16.53	1.00
Trigger	61869726	16.29	0.99
Two reconstructed electrons	40238063	15.97	0.97
η	36465364	15.29	0.93
E_{T}	1747586	14.28	0.86
Electron quality	1710056	13.59	0.82
Identification	299073	11.60	0.70
B-layer	274997	11.25	0.68
Isolation	273929	10.98	0.66
Invariant mass	266543	10.98	0.66

Table 6.1: Event numbers after selection cuts for the data sample and a simulated Z'_{SSM} sample ($\mathrm{m}_{Z'} = 1500$ GeV, $m_{ee} > 750$ GeV). The numbers for the simulated sample include all corrections as described in Sec. 5.3, as well as the weighting to the data luminosity. Furthermore, DY events with invariant masses above 750 GeV are included in the count (they contribute ∼20%).

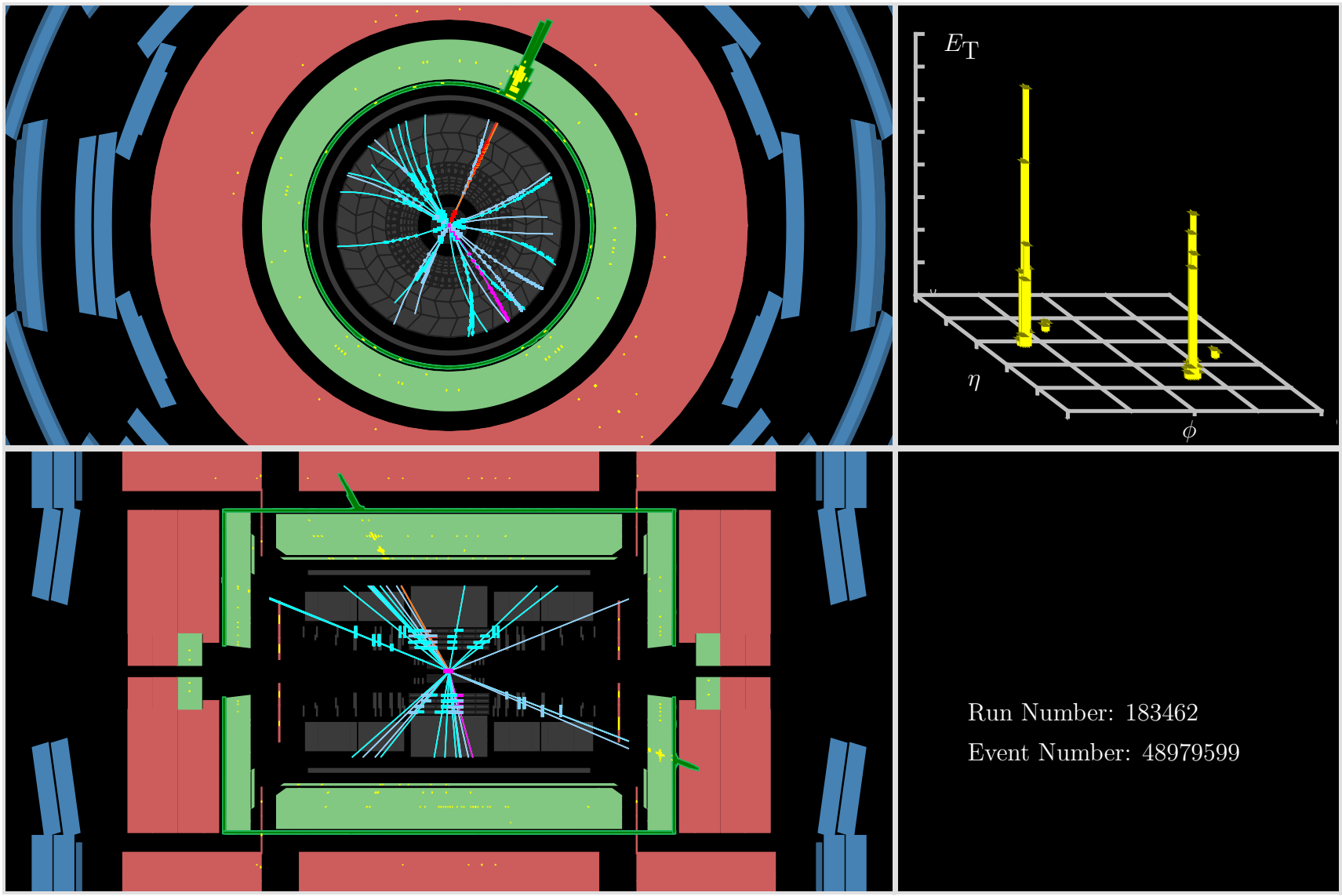

Figure 6.1: Event display of the dielectron event with the highest invariant mass (m_{ee} = 993 GeV) after full event selection [95].

Figure 6.2(a) shows the (η, ϕ)-map of all electrons in the data sample that pass the full selection. The region centered at (η, ϕ) = (0.7, -0.7) has less electrons than the surrounding areas. This is a part of the EM calorimeter that was not fully functioning during a fraction of the data taking. The cut on the electron quality ensures that electrons falling into this region are not considered, since their energy cannot be reconstructed reliably. To allow for a consistent comparison between data and the simulated backgrounds, as described in Sec. 5.3.3, this region is also excluded for a fraction of the simulated samples, which can be seen in Fig. 6.2(b).

The acceptance of the selection cuts can be seen in Fig. 6.3 for different $m_{Z'}$. The problematic region in the EM calorimeter reduces the acceptance by about 4% (absolute). The turn-on as well as the drop at high $m_{Z'}$ is mainly due to the invariant mass cut as well as the cuts on electron η: The increase in $m_{Z'}$ up to ~2 TeV produces more Z' bosons at rest, which causes the decay electrons to be more central, leading to more events passing the η cuts. However, above $m_{Z'}$ of ~2 TeV, it becomes less and less likely that the colliding quarks have enough energy to produce a Z' event at the peak mass, and a low mass tail develops (compare Fig. 5.1), whose decay electrons are again less central.

6.2 QCD background estimation from data

Applying the event selection cuts reduces the probability that events are chosen which contain one or two QCD jets instead of a real electron pair. However, due to the high production rates for QCD jets in *pp* colliders, the event sample still contains a non-negligible number of jets faking electrons.

The shape of the kinematic distribution of the QCD multijet background is estimated

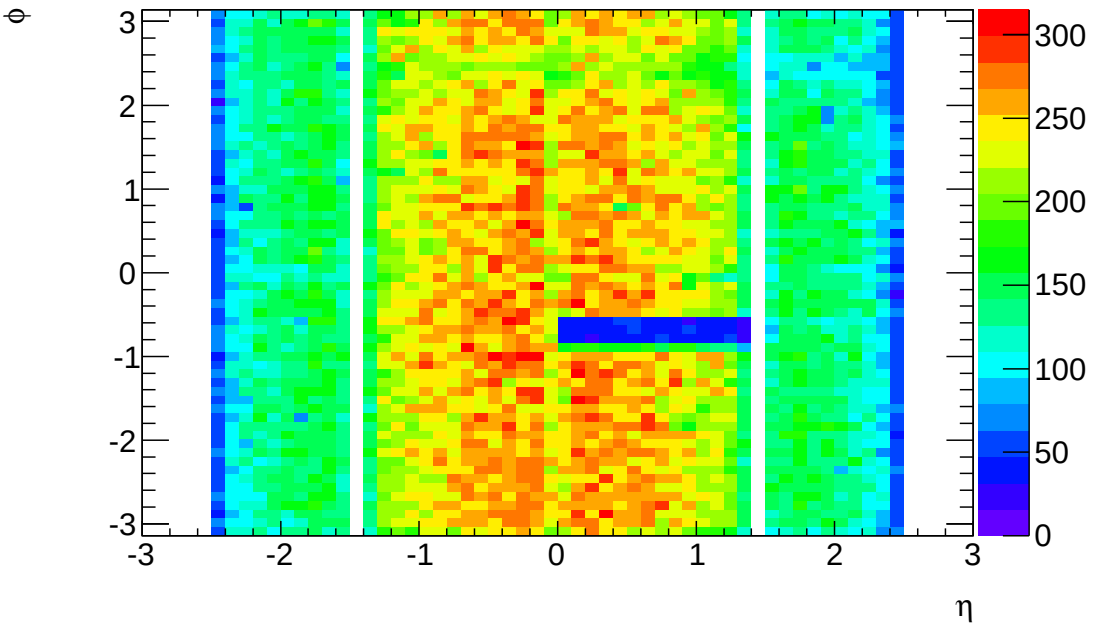

(a)

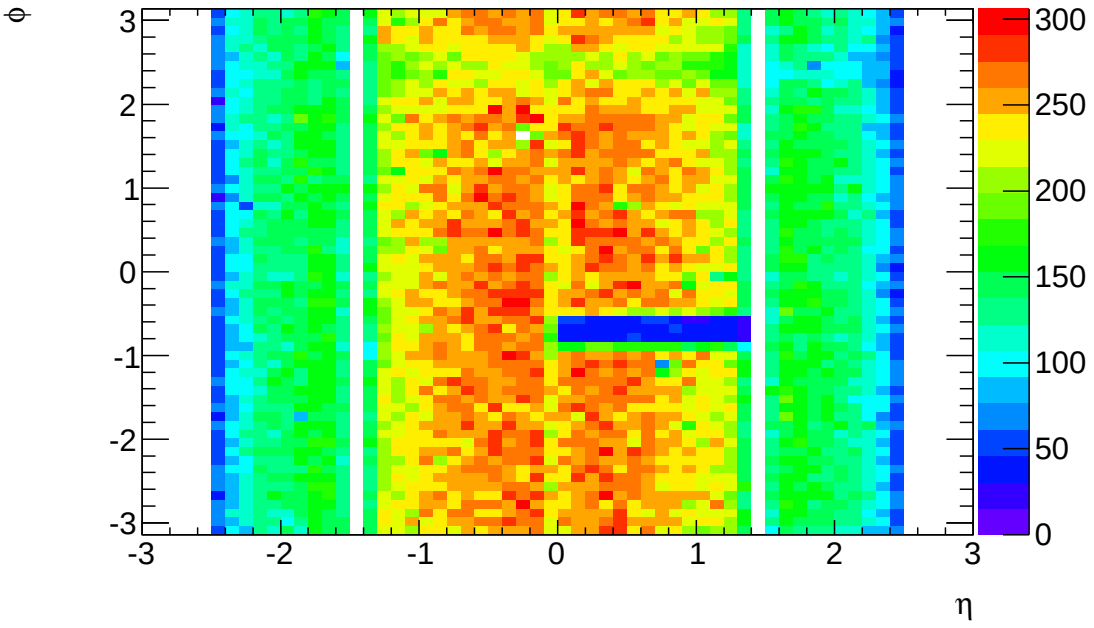

(b)

Figure 6.2: (η, ϕ)-map of all electrons passing the full selection in data (a) and in the simulated DY background sample (b). Regions colored in violet/blue have less events than regions colored in yellow/red.

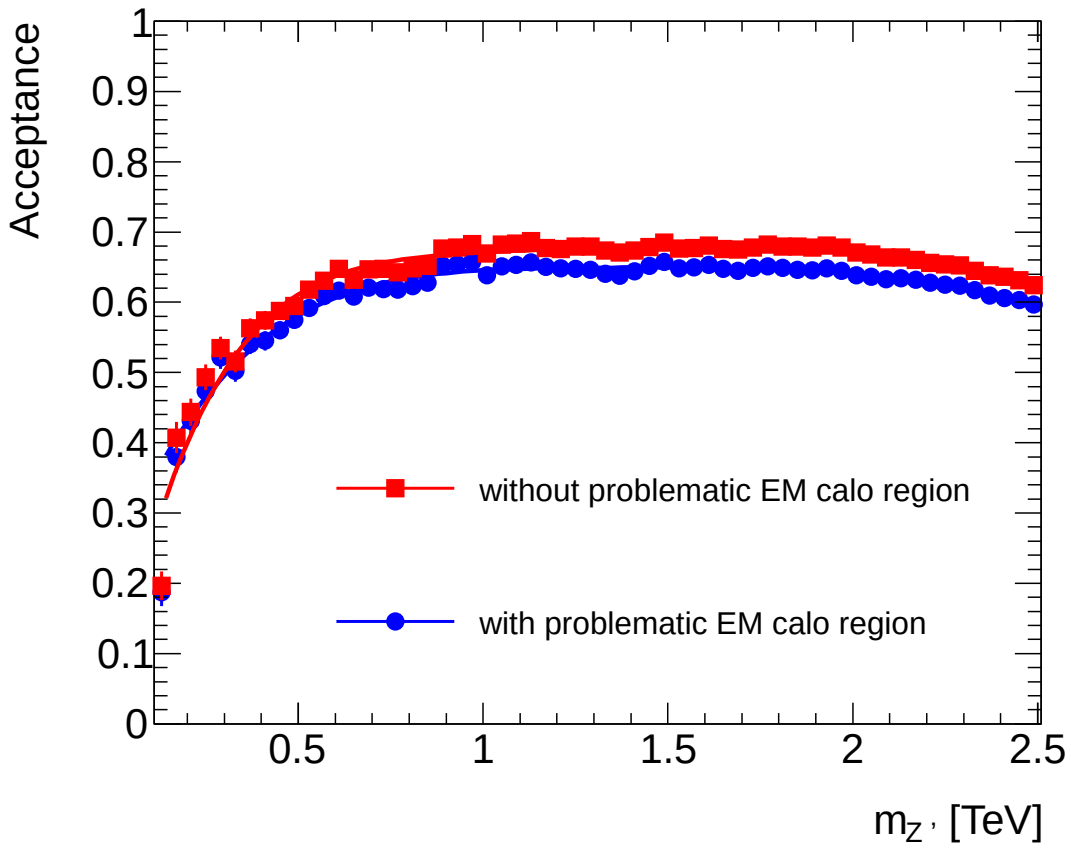

Figure 6.3: Efficiency of the selection cuts for different $m_{Z'}$.

from data by inverting some of the cuts on the electron identification. The normalization is determined in a two-component template fit of the QCD shape and the other backgrounds to the invariant mass distribution in data. Two additional estimation methods are used as a cross-check and to assign systematic uncertainties.

6.2.1 Multijet shape estimate

We request data events to pass all selection cuts of the standard cutflow (compare Sec. 6.1.1) except for the Medium identification cut (see Sec. 4.4). In order to select QCD jets that might be able to fake real electrons, we require the objects to pass the Loose identification.

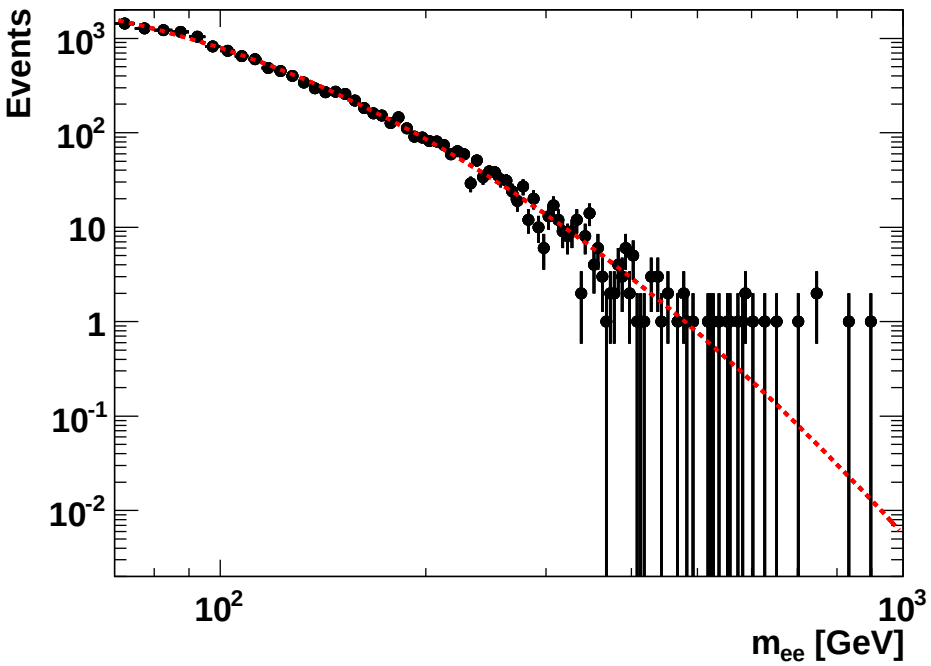

Figure 6.4: The invariant mass spectrum obtained by reversing the shower shape cuts in the first layer of the EM calorimeter is fitted with a dijet function [90]. The probability of this fit function to describe the reverse identification distribution correctly is 77%.

This ensures that the energy showers of the jets in the second layer of the EM calorimeter are similar to real electron showers. In order to avoid selecting real electrons, two cuts of the Medium identification (compare Table 4.1) are reversed which describe the shower shapes in the finely binned first layer of the EM calorimeter.

In order to smoothen the distribution and extrapolate it to high invariant masses, the resulting invariant mass distribution is fitted with an analytical function (see Fig. 6.4):

$$f(x) = p_0 x^{p1} x^{p2 \cdot Log x}. \tag{6.1}$$

This function describes the dijet invariant mass spectrum very well [96, 97] and Fig. 6.4 shows that it is also an appropriate model in this analysis.

6.2.2 Multijet background normalization

The dielectron invariant mass spectrum between 70 and 200 GeV is used as a discriminator to find the fraction of the QCD multijet background in data. Three samples are used: Data, the QCD shape obtained as described above, and the sum of the remaining backgrounds after event selection taken from simulated samples and weighted according to their corresponding theory cross-sections (compare Sec 5.2.2).

As shown in Fig. 6.5, a two component template fit of the two background histograms to the data distribution determines the normalization of the QCD multijet background. To avoid biases, the complete Z boson mass peak is covered by a single bin, since the simulated DY sample does not model the shape of the peak perfectly. The remaining shape differences between the QCD dijet distribution and the other backgrounds, dominated by DY, are large enough to constrain the fit.

To assign systematic uncertainties to this multijet estimation method, different electron cuts are inverted, and the QCD normalization uncertainty from the two-component template fit is propagated to the full mass range.

6.2.3 Cross-checks with alternative methods

In order to obtain systematic uncertainties on the estimated QCD multijet distribution and to cross-check the baseline method, the QCD multijet background is determined using two independent methods [90].

The "Isolation Fits method" uses the distribution of the isolation variable as a discriminating variable. This works because real electrons deposit far less energy in a cone around themselves than QCD jets which contain several particles. Templates for QCD multijets are

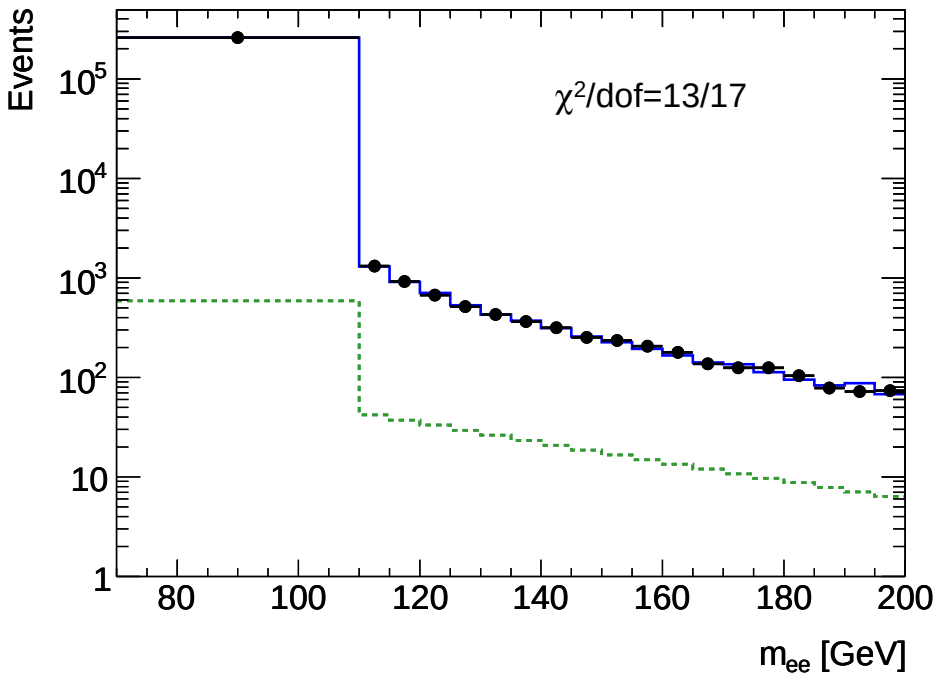

Figure 6.5: Template fit used to normalize the QCD multijet shape to data (black dots). The green, dotted line shows the QCD estimation as it results from the log likelihood fit, while the blue curve describes the full background estimation (QCD estimate plus all other backgrounds from simulated samples).

derived from data by requiring a maximum fraction of high-threshold hits in the TRT. This enriches the sample in QCD fakes, as pions are less relativistic than the lighter electrons and therefore produce less transition radiation (compare Sec. 4.4, 3.2.3). Templates for real electrons are obtained by applying cuts that select electrons from W boson decays. These isolation templates are fitted to data passing the full event selection (Sec. 6.1.1). The fits are performed separately for the leading and subleading electron in bins of E_{T} and m_{ee}, and the resulting QCD jet yields are combined to determine the amount of QCD multijet and W + jets background for each dielectron invariant mass bin. The systematic uncertainty is dominated by the uncertainty on the normalization from the fit.

An alternative QCD multijet estimation method, the "Fake Rates method", uses events

recorded with jet triggers. Jets faking electrons are obtained by requesting them to be reconstructed as electrons and to pass a subset of the Loose identification cuts (Sec. 4.4). Real electrons from Z boson and W boson decays are removed by applying cuts on the dielectron invariant mass and $E_{\mathrm{T}}^{\mathrm{miss}}$. The fake rate is calculated by determining the fraction of events in this sample passing the Z' electron selection criteria. This rate is obtained for different η and E_{T} bins and has a systematic uncertainty of ∼40%, obtained from the comparison of samples selected by different jet triggers. The fake rate is applied to a selection of electron-jet events, in which the jets are required to fail the Medium identification cuts, but otherwise pass the same cuts as the sample used to calculate the fake rates. This results in a combined estimate of QCD multijet and W + jets backgrounds.

Table 6.2 shows the resulting amount of QCD multijet and W + jets background in this analysis after full selection as obtained by the three methods. The W + jets yield from the simulated sample is normalized to the theory cross-section and luminosity and is added to the results of the baseline method to allow for a comparison between the methods. The predicted yields of the three methods agree within their large uncertainties, and the largest differences to the baseline estimate are used as an additional systematic uncertainty.

Mass range [GeV]	Baseline method	Isolation Fits	Fake Rates
$70 < m_{ee} < 110$	482.3 ± 85.2	-	-
$110 < m_{ee} < 130$	136.7 ± 24.2	107.0 ± 46.0	-
$130 < m_{ee} < 150$	90.4 ± 16.1	116.3 ± 45.1	72.8 ± 29.2
$150 < m_{ee} < 200$	113.7 ± 20.2	147.6 ± 58.3	104.9 ± 42.0
$200 < m_{ee} < 800$	85.2 ± 15.2	149.8 ± 52.4	106.4 ± 42.6
$800 < m_{ee} < 3000$	0.2 ± 0.2	-	-

Table 6.2: Comparison of the different QCD jet estimates [90]. As the Isolation Fits and the Fake Rate methods include W+jets, the W+jets number from simulation has been added to the results of the baseline method.

6.3 Comparison of data with Standard Model expectations

The full event selection (Sec. 6.1) is applied to the DY, Diboson, W + jets, and $t\bar{t}$ simulated samples. The resulting invariant mass distributions are weighted by the corresponding cross-sections (see Sec. 5.2.2) and added together. The estimated QCD background (see Sec. 6.2) is subtracted from the data distribution, and the sum of the other SM backgrounds is normalized to the remaining invariant mass distribution between 70 and 110 GeV. This normalization of the simulated samples to data simplifies the treatment of systematic uncertainties, since all systematic uncertainties on the SM background that are mass independent, like the luminosity uncertainty, cancel out.

6.3.1 Event yields

Table 6.3 shows the predicted SM background as well as the observed event counts in data after the selection cuts. The errors include both statistical and systematic uncertainties, except for the uncertainty on the total background in the normalization region (70-110 GeV) which corresponds to the square root of the number of observed events. For each bin in dielectron invariant mass, the observed number of data events agrees with the SM background within $\pm 1\sigma$.

6.3.2 Kinematic distributions

This section shows a comparison of kinematic distributions from data after full event selection with the estimated SM backgrounds.

m_{ee} [GeV]	70-110	110-130	130-150	150-170	170-200
DY	258481.5±413.9	3185.4±106.9	1182.9±46.4	607.9±28.0	473.0±23.6
$t\bar{t}$	218.1±23.0	86.9±10.5	64.1±7.6	50.9±5.2	51.2±5.2
Dibosons	368.2±18.8	30.9±2.3	23.8±2.0	14.9±1.4	15.7±1.5
W+jets	150.1±42.8	56.7±17.0	40.0±12.5	26.8±8.7	26.1±8.4
QCD	332.2±59.1	79.9±41.9	50.4±19.7	32.2±7.3	28.6±6.5
Total	259550.0±421.3	3439.9±116.6	1361.2±52.5	732.8±30.7	594.6±26.4
Data	259550	3419	1362	758	578
m_{ee} [GeV]	200-240	240-300	300-400	400-800	800-3000
DY	311.8±17.6	196.1±8.6	105.0±5.2	53.8±3.1	2.8±0.4
$t\bar{t}$	37.0±3.8	30.4±3.1	14.9±1.4	5.4±0.5	0.1±0.0
Dibosons	13.5±1.4	7.8±0.9	7.5±1.1	3.1±0.5	0.3±0.1
W+jets	19.5±6.4	14.2±5.0	9.0±3.5	4.6±2.0	0.2±0.4
QCD	19.0±15.2	11.6±9.3	5.5±4.4	1.8±1.4	0.0±0.0
Total	400.8±24.5	260.0±14.0	141.9±7.9	68.8±4.0	3.4±0.6
Data	405	256	147	65	3

Table 6.3: Expected and observed number of events after selection cuts. The errors quoted include both statistical and systematic uncertainties, except for the uncertainty on the total background in the normalization region (70-110 GeV) which corresponds to the square root of the number of observed events. Entries of 0.0 indicate a value < 0.05.

In the dielectron invariant mass spectrum (Fig. 6.6), the mass peak of the Z boson can clearly be seen. This is the distribution in which we look for an additional resonance peak. Three Z'_{SSM} distributions with different masses are overlayed for illustration. The η distribution of the leading and subleading electron is shown in Fig. 6.7. The gaps in the distribution are due to the selection cuts rejecting electrons that fall into the transition region between the barrel and endcap of the EM calorimeter ($1.37 < |\eta| < 1.52$). The asymmetry in η is due to the region of the calorimeter that was not fully functional during a fraction of the data taking. Other variations in the measured η rates, like the dip around 0, are in part due to detector properties. Only the DY background is shown, since the other background contributions are too small to be visible in linear scale. Figure 6.8 shows the E_{T} distributions of the leading and the subleading electron separately. Again, three Z'_{SSM}

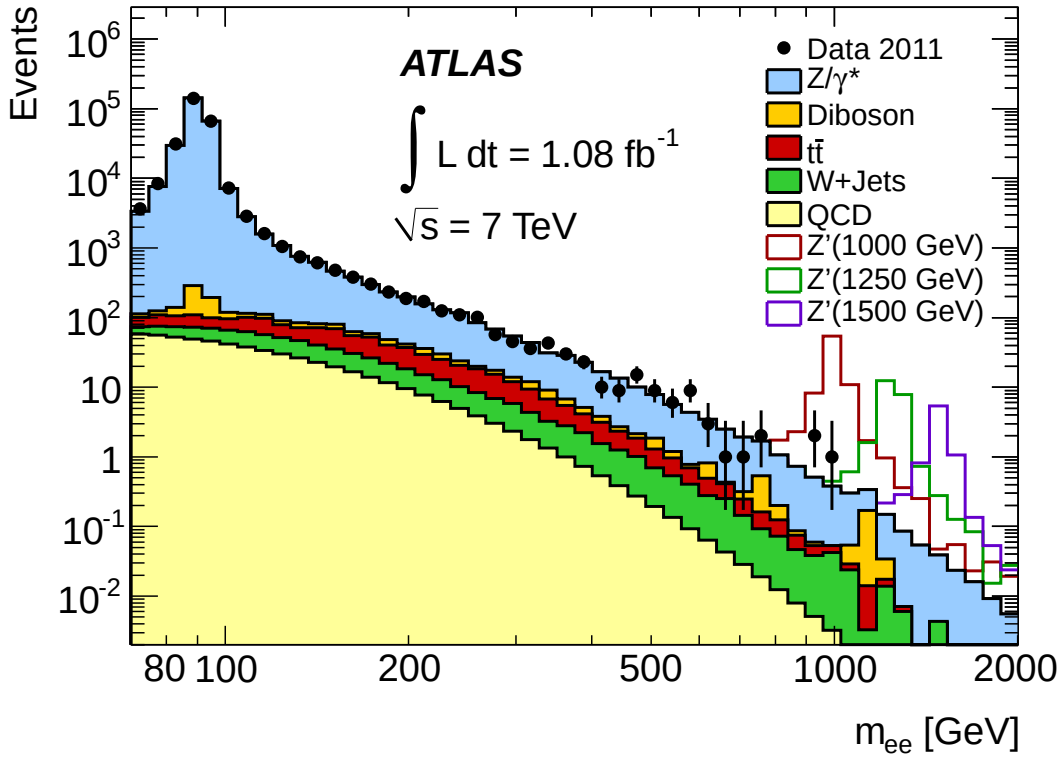

Figure 6.6: Dielectron invariant mass distribution after full event selection, comparing the SM backgrounds to data. Three Z'_{SSM} distributions are added for illustration.

distributions with different masses are overlayed for illustration. The dielectron rapidity and dielectron p_{T} can be seen in Fig. 6.9. The isolation distributions are shown in Fig. 6.10 for the full dataset and in Fig. 6.11 for events that have a dielectron invariant mass above 130 GeV. These distributions are important checks of the QCD multijet estimate, since this background dominates at the high end of the isolation spectrum. In all distributions the estimated SM background describes the data very well.

6.4 Muon channel

We also performed this analysis in the dimuon channel. This section gives a brief overview over the event selection and comparison between data and expected SM background. More

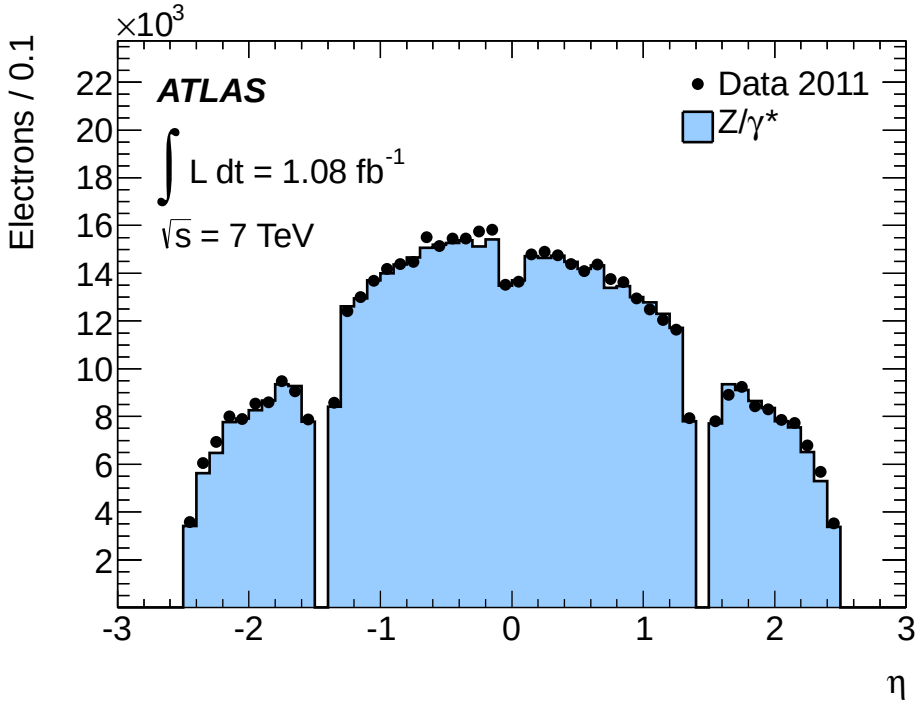

Figure 6.7: η distribution of the leading and subleading electrons after full event selection, comparing the SM backgrounds to data.

details can be found in [6] and [90].

6.4.1 Event selection

In order to obtain the dimuon mass spectrum, events with two muon candidates with opposite charge are selected. Both muons have to fulfill $p_{\mathrm{T}} > 25$ GeV and they have to pass quality cuts in the Inner Detector. Furthermore at least three hits are required in each of the inner, middle, and outer layers of the muon system. Muons are only considered if they have tracks close to the nominal interaction points in order to suppress cosmic rays. In order to reduce background from QCD multijet events, the muon tracks have to be isolated. The total signal acceptance in the muon channel is 40%, much lower than in the electron channel, which is mainly due to the need to improve the p_{T} resolution by only accepting muons that pass very

strict cuts.

6.4.2 Comparison of data with Standard Model expectations

$m_{\mu^+\mu^-}$ [GeV]	70-110	110-130	130-150	150-170	170-200
DY	236318.6±319.7	3132.1±87.5	1073.4±35.9	548.7±21.8	416.3±18.3
$t\bar{t}$	193.1±21.0	70.0±9.1	50.7±7.0	34.2±3.6	37.7±3.9
Diboson	306.7±15.9	24.9±2.2	19.4±2.0	13.3±1.6	11.7±1.5
W+jets	1.3±0.7	0.4±0.4	0.0±0.0	0.2±0.2	0.0±0.0
QCD	1.3±1.2	0.3±0.2	0.1±0.1	0.1±0.1	0.0±0.0
Total	236821.0±486.6	3227.8±88.0	1143.7±36.6	596.5±22.2	465.8±18.7
Data	236821	3210	1132	621	443
$m_{\mu^+\mu^-}$ [GeV]	200-240	240-300	300-400	400-800	800-3000
DY	249.4±13.0	152.9±7.1	80.8±3.9	40.3±2.5	2.0±0.3
$t\bar{t}$	30.5±3.2	20.6±2.2	11.7±1.2	4.2±0.4	0.1±0.0
Diboson	10.1±1.4	8.0±1.1	6.7±1.1	1.7±0.5	0.0±0.0
W+jets	0.0±0.0	0.0±0.1	0.0±0.0	0.0±0.0	0.0±0.0
QCD	0.0±0.0	0.0±0.0	0.0±0.0	0.0±0.0	0.0±0.0
Total	290.0±13.5	181.5±7.6	99.3±4.2	46.1±2.6	2.1±0.3
Data	279	195	83	51	5

Table 6.4: Expected and observed number of events in the dimuon channel [6]. The errors quoted include both statistical and systematic uncertainties, except the total background in the normalization region which corresponds to the square root of the number of observed events. Entries of 0.0 indicate a value < 0.05.

Table 6.4 shows the comparison between the predicted SM background and the observed event counts in data after the selection cuts. The errors include both statistical and systematic uncertainties, except for the uncertainty on the total background in the normalization region (70-110 GeV) which corresponds to the square root of the number of observed events.

The invariant mass distribution in data and for the SM backgrounds is shown in Fig. 6.12. Three Z'_{SSM} distributions with different masses are overlayed for illustration.

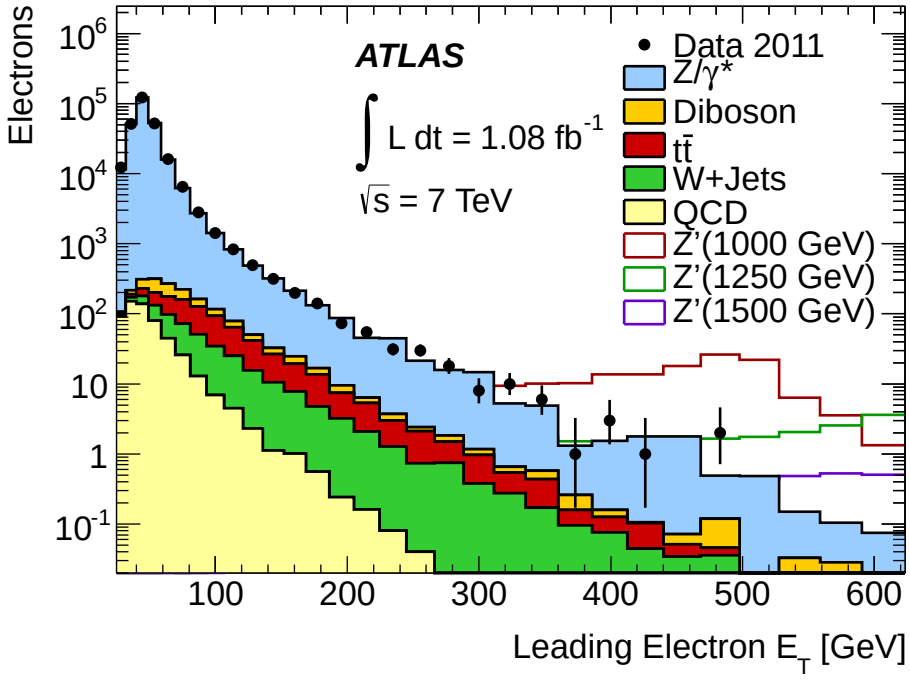

(a)

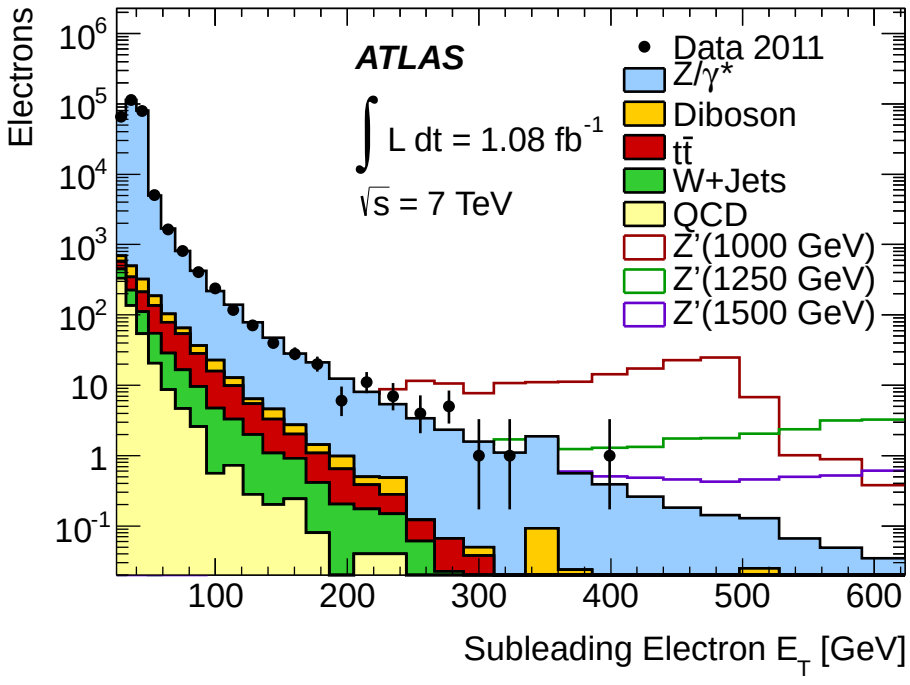

(b)

Figure 6.8: E_{T} distribution of the leading (a) and subleading electron (b) after full event selection, comparing the SM backgrounds to data. Three Z'_{SSM} distributions are added for illustration.

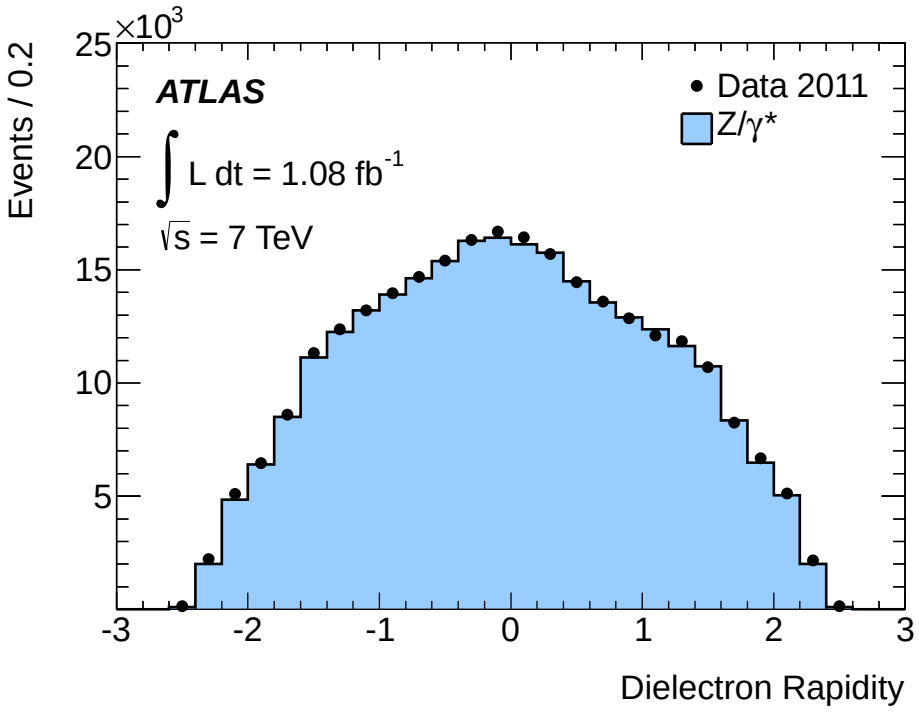

(a)

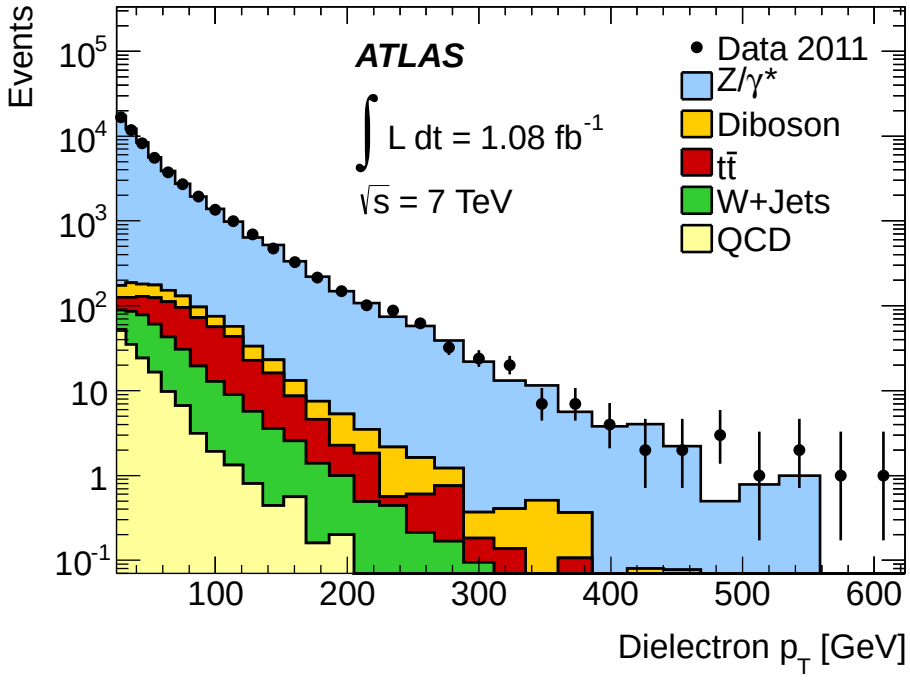

(b)

Figure 6.9: Dielectron rapidity (a) and dielectron p_{T} (b) after full event selection, comparing the SM backgrounds to data.

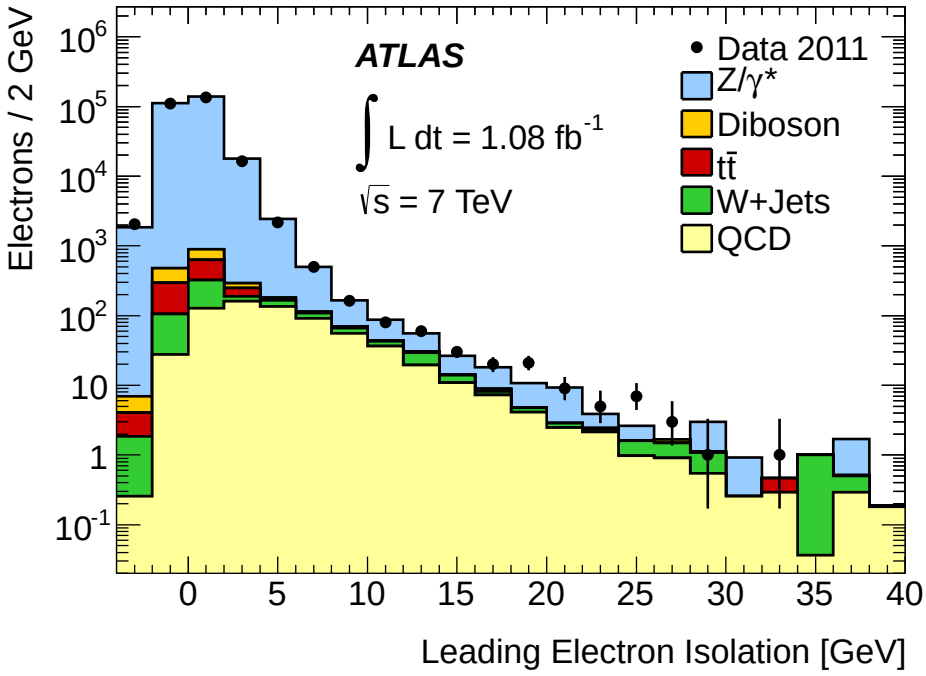

(a)

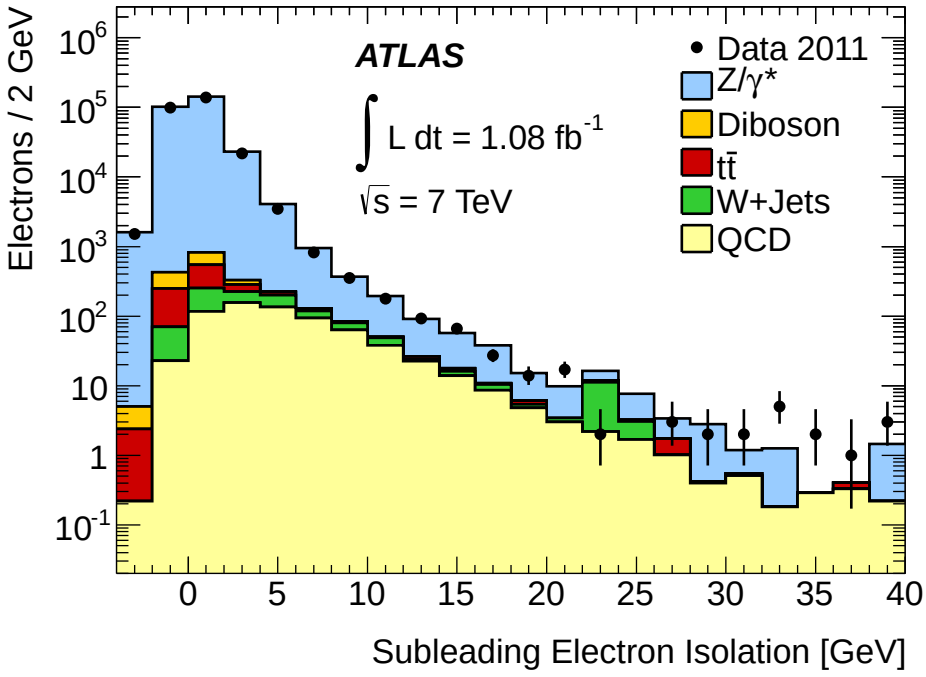

(b)

Figure 6.10: Calorimeter isolation distribution of the leading (a) and subleading electron (b) after full event selection, comparing the SM backgrounds to data.

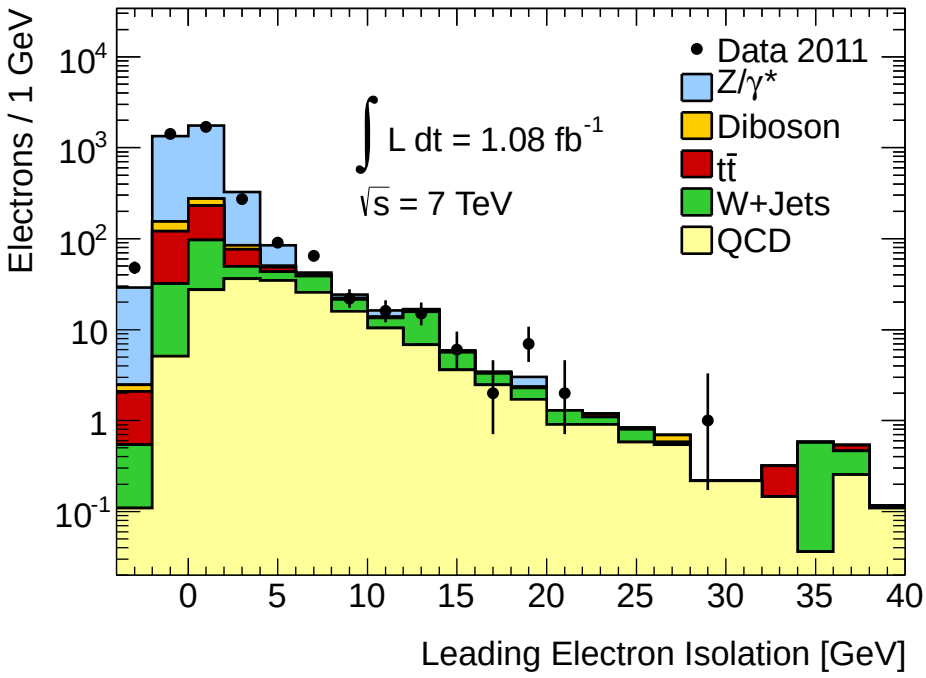

(a)

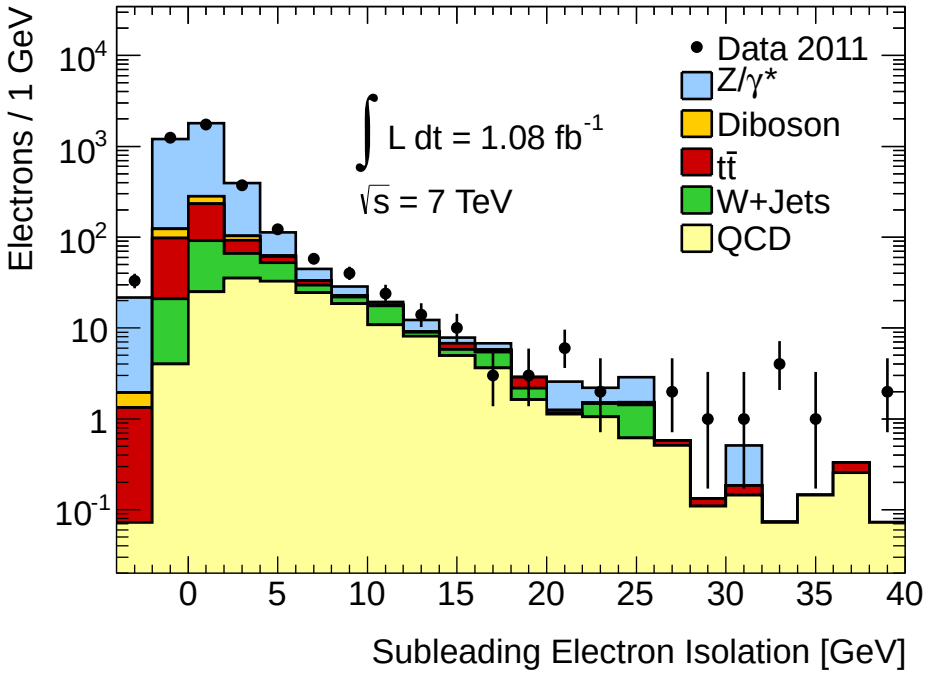

(b)

Figure 6.11: Calorimeter isolation distribution of the leading (a) and subleading electron (b) after full event selection, comparing the SM backgrounds to data. Only events with $m_{ee} >$ 130 GeV are shown.

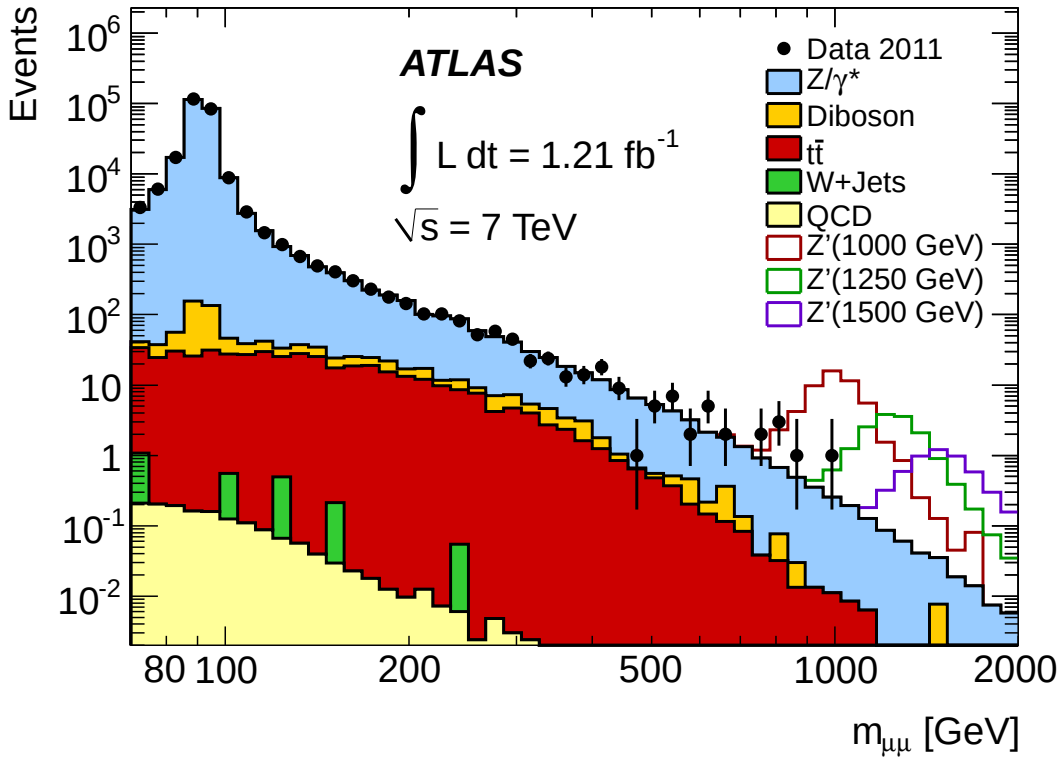

Figure 6.12: Dimuon invariant mass distribution after full event selection, comparing the SM backgrounds to data [90]. Three Z'_{SSM} distributions are added for illustration.

Chapter 7

Statistical treatment and results

This chapter starts with a description of the theoretical and experimental systematic uncertainties. The dielectron invariant mass spectrum in data is searched for peak-like deviations from the SM background. Since no statistically significant excess is found, 95% C.L. upper limits are set on the cross-section times branching ratio of Z' bosons and RS gravitons using a Bayesian approach [98, 99].

7.1 Systematic uncertainties

The treatment of systematic uncertainties is facilitated by normalizing all SM backgrounds to data between dielectron invariant masses of 70 and 110 GeV. As a result, mass-independent uncertainties, like the luminosity uncertainty, need not to be considered because they would result in an overall shift of the distribution which is however fixed by the normalization at the Z boson mass peak.

The largest systematic uncertainty on the cross-sections of simulated signal and background processes is due to incomplete knowledge of the PDFs (see Chapter 5 and Sec. 2.1.3)

and the strong coupling constant α_S. This uncertainty grows with invariant mass because the input values for the PDFs are measured at low energies. In order to determine the size of the uncertainty, DY, Z'_{SSM}, and G^* cross-sections produced with systematic PDF variations are compared to the nominal ones. For further comparison, cross-sections are produced with PDF sets which correspond to variations of α_S [90]. The resulting $Z'/G^*/DY$ cross-section uncertainty is 10% at an invariant mass of 1.5 TeV.

In order to improve the cross-section estimate of the simulated DY and Z' samples, which are produced at LO, k-factors are calculated (compare Sec. 5.2.2). The uncertainties on the mass-dependent QCD k-factors are determined by varying the normalization and factorization scales by a factor of two around the nominal values (compare Sec. 2.1.3). Furthermore, the k-factors are reevaluated for Z boson production only instead of Z/γ^* production and the difference, less than 1%, is included in the uncertainty. The total uncertainty of the QCD k-factor is 3% at an invariant mass of 1.5 TeV. The corresponding uncertainty on the electroweak k-factor is 4.5% to account for real boson emission and higher order corrections as well as differences between the generator used for calculating the electroweak corrections and PYTHIA, with which the DY samples are simulated.

The experimental uncertainties in this analysis are quite small:

- The uncertainty on the energy calibration of the EM calorimeter ranges from energy shifts of 0.5% to 1.5%, depending on transverse energy and η [80].
- For high energies, the energy resolution is dominated by the constant term (see Sec. 4.6.1), which has a negligible uncertainty.
- Uncertainties on trigger and identification efficiencies are independent of the invariant mass above ∼90 GeV.

- The isolation cut has been shown in the simulation to cause an efficiency drop of 1.5% for an invariant mass of 1.5 TeV. As illustrated in Fig. 4.3 in Sec. 4.6.1, this drop is cancelled by the rising efficiency of the B-layer cut, but in order to account for possible differences between the modeling and data, a conservative uncertainty of 1.5% is assigned.

- The largest contribution to the uncertainty on the estimation of the QCD multijet background is the comparison to alternative estimates (compare Sec. 6.2). This uncertainty is very large, however the QCD multijet background is only a small fraction of the total SM background (compare Table 6.3), so the overall uncertainty on the background yield is only 1.5% at an invariant mass of 1.5 TeV.

Table 7.1 lists the systematic uncertainties that are applied when searching for a signal and setting limits. The uncertainties are presented as the relative changes in the signal/background yields for variations of 1σ. Other systematic uncertainties below 3% are neglected in the analysis, since they do not change the results visibly. The uncertainty on the QCD estimate is considered nonetheless since it is the only uncertainty that can be larger at lower invariant masses. No theoretical uncertainties are applied on the signal. However, the luminosity normalization of the SM background to the data under the Z boson mass peak has a 5% uncertainty due to the Z boson cross-section uncertainty.

7.2 Statistical analysis

This section describes the likelihoods used for the signal search and for limit setting, as well as the treatment of systematic uncertainties.

Source	Dielectrons	
	Signal	Background
Normalization	5%	NA
PDFs/α_S	NA	10%
QCD k-factor	NA	3%
Weak k-factor	NA	4.5%
QCD estimate	NA	1.5%
Total	5%	11%

Table 7.1: Systematic uncertainties on the expected signal and background yields at $m_{ee} = 1.5$ TeV for the Z' and RS graviton analysis. NA means not applicable [90].

According to Poisson statistics, the likelihood to observe n events for a predicted yield of μ can be calculated as

$$\mathcal{L}(n|\mu) = \frac{\mu^n e^{-\mu}}{n!}. \tag{7.1}$$

The predicted yield is the sum of background and potential signal, while the observed events are the event counts in data:

$$\mu = \sum_j N_j = N_{sig} + N_{bkg} \quad , \quad n = N_{data}. \tag{7.2}$$

N_{bkg} is predicted and N_{data} is measured; the parameter of interest is N_{sig}.

Systematic uncertainties, like a change in the QCD k-factor, could change the predicted yield:

$$\mu = \sum_j N_j \prod_i (1 + G(\theta_{ij}, \delta_{ij})). \tag{7.3}$$

According to the Bayesian treatment of systematic uncertainties, G is the probability density function of the nuisance parameter θ_{ij} which is usually chosen to be Gaussian with a mean

of zero and a σ that corresponds to the relative uncertainty δ_{ij}.

In this analysis, the likelihood is calculated for every bin k in the search range of the invariant mass spectrum ($m_{ee} > 130$ GeV), and the results of all bins are multiplied to form an overall likelihood:

$$\mathcal{L}(n|N_j, \theta_{ij}) = \prod_k \frac{\mu_k^{n_k} e^{-\mu_k}}{n_k!}, \tag{7.4}$$

where μ is defined in Eq. 7.3 and n, N_j, and θ_{ij} are now vectors whose dimensions correspond to the number of mass bins.

Using a binned likelihood takes advantage of the peak-like shape of the signal, which makes the analysis more robust toward broad underestimates of the SM background and more sensitive to finding a peak than a single bin counting experiment. Eq. 7.4 takes into account possible correlations of systematic uncertainties not only between signal and background but also between different bins.

In order to obtain a reduced likelihood $\mathcal{L}'$ that is only a function of N_{sig}, a multidimensional integral over the probability functions of the nuisance parameters is performed. This is done by integrating numerically using the Bayesian Analysis Toolkit [98]:

$$\mathcal{L}'(n|N_{sig}) = \int \mathcal{L}(n|N_{sig}, N_{bkg}, \theta_0, \theta_1, \theta_2 ...) d\theta_0 d\theta_1 d\theta_2 ... \tag{7.5}$$

Instead of the number of signal events N_{sig}, the cross-section times branching fraction $\sigma_{sig}B$ is used when calculating the likelihood. The translation is done according to Eq. 5.1 by replacing the integrated luminosity L_{int} with the number of Z boson events N_Z, the Z

boson cross-section σ_Z and acceptance A_Z:

$$\sigma_{sig}B = \frac{N_{sig}}{A_{sig}}\frac{A_Z}{N_Z}\sigma_Z B. \tag{7.6}$$

This approach has the advantage that all mass-independent uncertainties cancel out; however, the uncertainty on σ_Z has to be included (compare Sec. 7.1). Mass-dependent uncertainties on N_Z and $\frac{A_Z}{A_{sig}}$ are small enough to be neglected. This thesis correctly includes higher order corrections to N_Z and σ_Z (compare Sec. 5.2.2). The resulting limits are slightly more stringent than in Ref. [6], where higher order effects were accounted for twice.

7.3 Signal search

The first part of the statistical analysis is to quantify possible excesses in the data invariant mass spectrum as compared to the SM background (see Fig. 6.6). The reduced likelihood over the mass spectrum, starting well above the normalization region at 130 GeV, is calculated using the Z'_{SSM} model as a reference (see Eq. 7.5).

Figure 7.1 shows the reduced likelihoods for different test masses and cross-sections. The red regions have higher likelihoods than the blue regions and correspond to local excesses in the dielectron spectrum in the data compared to the SM prediction (compare Fig. 6.6). The most likely values for $M_{Z'}$ and $\sigma_{Z'}$ are $M_{Z'} = 600$ GeV and $\sigma_{Z'} = 0.012$ pb.

The next step is to determine the statistical significance of the excess. For this, we compute the probability for the SM background to fluctuate to the observed data. The Neyman-Pearson lemma [100] states that the best discriminant between two hypotheses, in our case (signal+background) vs. (background only), is the log-likelihood ratio (LLR). The

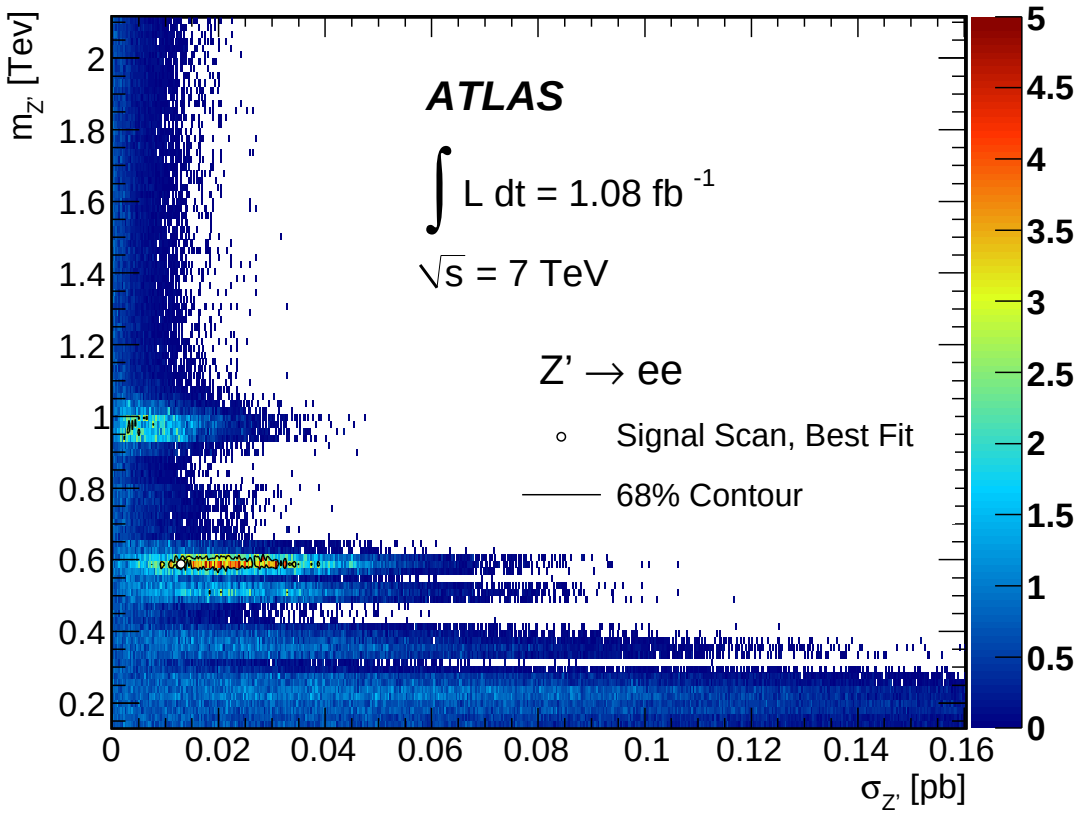

Figure 7.1: Reduced likelihoods to have an excess caused by new physics for different Z' test masses and cross-sections.

likelihood for the $\hat{M}_{Z'} = 600$ GeV and $\hat{\sigma}_{Z'} = 0.012$ pb as well as the background-only hypotheses are calculated. Then the LLR value is determined as:

$$LLR(\hat{\sigma}_{Z'}, \hat{M}_{Z'}, \hat{\theta}_i, \hat{\hat{\theta}}_i) = \ln \frac{\mathcal{L}(n|\hat{\sigma}_{Z'}, \hat{M}_{Z'}, \hat{\theta}_i)}{\mathcal{L}(n|\hat{\sigma}_{Z'} = 0, \hat{\hat{\theta}}_i)}. \tag{7.7}$$

Here, $\hat{\theta}_i$ and $\hat{\hat{\theta}}_i$ are the values of the nuisance parameters, determined by integrating over all other parameters and finding the maximum of the respective reduced likelihoods.

A large number of background-only pseudo-data distributions are produced: First, values of the nuisance parameters are chosen by sampling from their Gaussian distributions, then the

SM background distribution, shifted by the systematic uncertainties, is sampled according to a Poisson distribution. For each of the pseudo-data distributions, $\hat{M}_{Z'}$ and $\hat{\sigma}_{Z'}$ are determined, and the LLR is calculated. Since $\hat{M}_{Z'}$ and $\hat{\sigma}_{Z'}$ are free parameters and can be different for every pseudo-data distribution, the look-elsewhere effect is naturally taken into account. This effect describes the reduction of the significance of an excess when considering the probability that a statistical fluctuation might appear anywhere in the mass range. The fraction of pseudo-experiments in which an LLR value as large or larger than the one in data is found is called p-value,

$$p = p(LLR \geq LLR_{data}|\text{SM only}). \tag{7.8}$$

The common convention is that a p-value less than 1.35×10^{-3} constitutes evidence for a signal and a p-value less than 2.87×10^{-7} constitutes a discovery. (These are one-sided integrals of the tails of a unit Gaussian distribution beyond $+3\sigma$ and $+5\sigma$, respectively.)

In this analysis, the p-value from the LLR test is 0.54, which means more than half the background-only pseudo-data distributions show an excess at least as significant as the one found in data, thus the observed excess is not statistically significant.

The search for a significant excess is also performed in an alternative fashion, independent of the Z' mass shape. The BumpHunter algorithm [101] divides the invariant mass spectrum into ranges with varying widths, and determines the local p-value for each range. Only ranges are considered in which the data have a higher yield than the background, and for which there is an agreement between data and SM background in sidebands half as wide as the ranges themselves. The window with the smallest local p-value, and therefore the most significant excess is determined. This smallest local p-value is used as a test statistic

in a large number of background-only pseudo-data distributions. For each of the pseudo-experiments, the smallest local p-value could be in a different mass range, which accounts for the look-elsewhere effect. An overall p-value is calculated by determining the fraction of the pseudo-data distributions which have a smallest local p-value smaller or equal to the one determined from data. The overall p-value thus obtained is 0.79, thus both methods state that there is no significant excess in the dielectron invariant mass spectrum as obtained from data by our event selection.

7.4 Limits

Since no significant excess is found in the dielectron invariant mass spectrum, limits are set at the 95% C.L. on the cross-section times branching fraction of the Z'_{SSM} boson and the RS graviton model with $k/\bar{M}_{Pl} = 0.1$ (compare Sec. 2.2.6). These $\sigma_{sig}B$ limits are obtained for a range of signal pole masses and are translated into lower mass limits on the Z'_{SSM} boson, different E_6 Z' bosons (compare Sec. 2.2.3), and the RS graviton with various values of $k/\bar{M}_{Pl}$.

$\mathcal{L}'(n|\sigma_{sig}B)$ (see Eq. 7.5, 7.6) gives the likelihood to find n data events given a signal cross-section and branching ratio. In order to translate this into an equation which describes the likelihood that there is a signal with $\sigma_{sig}B$ given that we see n data events, Bayes' theorem [102] is employed:

$$\mathcal{L}'(\sigma_{sig}B|n) = \mathcal{L}'(n|\sigma_{sig}B)\frac{\pi(\sigma_{sig}B)}{\pi(n)} \propto \mathcal{L}'(n|\sigma_{sig}B), \tag{7.9}$$

where $\pi(n)$ is the prior for the number of observed events and $\pi(\sigma_{sig}B)$ is the prior for

$\sigma_{sig}B$. $\pi(n)$ is the same for all possible values of $\sigma_{sig}B$:

$$\pi(n) = \text{const.} \tag{7.10}$$

Since we do not have any information about $\sigma_{sig}B$, we set its prior to be flat as well, following the common convention:

$$\pi(\sigma_{sig}B) = \text{const.} \tag{7.11}$$

The value for $\sigma_{sig}B$, which includes 95% of the integral over the likelihood starting at zero, is called 95% C.L. limit:

$$0.95 = \frac{\int_0^{(\sigma_{sig}B)95} \mathcal{L}'(\sigma_{sig}B|n)d(\sigma_{sig}B)}{\int_0^{\infty} \mathcal{L}'(\sigma_{sig}B|n)d(\sigma_{sig}B)}. \tag{7.12}$$

The limits which are listed in Sec. 7.4.1 and 7.4.2 are all 95% C.L. limits, which means, we state with 95% C.L. that $\sigma_{sig}B$ is smaller than the quoted limit $(\sigma_{sig}B)_{95}$.

7.4.1 Electron results

Figure 7.2 shows the limits on $\sigma_{sig}B$ for different test masses of the Z'_{SSM} boson (spin-1, 7.2(a)) and the RS graviton with $k/\bar{M}_{Pl} = 0.1$ (spin-2, 7.2(b)) as well as theoretical cross-section curves for several models. The mass at which the theoretical cross-section line intersects the limit curve is the lower mass limits.

The red line shows the $\sigma_{sig}B$ limits as they are observed in data. It is not smooth due to local excesses and deficits in the dielectron invariant mass spectrum in data compared

to the SM background expectation (see Fig. 6.6). The cross-sections times branching ratios above the limit line are excluded at the 95% C.L..

The plots also show expected limits and their 1σ and 2σ envelopes. These are the limits expected in the absence of signal. They are obtained by using 1000 background-only pseudo-data distributions as input for the limit setting. As for the signal search, the SM background histogram is modified by sampling values of the nuisance parameters from their Gaussian distributions. Then pseudo-data distributions are sampled from these background histograms according to a Poisson distribution. Figure 7.3 shows the σB limits for $m_{Z'} =$ 810 GeV from 1000 pseudo-data distributions. The dashed line indicates the median of the distribution, while the green and yellow areas show the 68% (1σ) and 95% (2σ) envelopes.

The theoretical cross-sections (times branching fractions) for the Z'_{SSM}, the Z'_{χ} and the Z'_{ψ} boson are shown in Fig. 7.2. The same peak shape and acceptance is assumed for all Z' models, which is a valid approximation as interference is neglected and the widths of the Z' bosons in the E_6 models under consideration are smaller than the Z'_{SSM} boson width (compare Fig. 2.5), making the limits slightly more conservative. For the RS graviton, the cross-section curves for $k/\bar{M}_{Pl} = 0.1$, 0.05, 0.03, 0.01 are presented. Again, the signal template and acceptance curve is the one for $k/\bar{M}_{Pl} = 0.1$, which has the largest width. Uncertainties on the cross-sections due to the QCD k-factor (in the Z' case) and the PDF (compare Sec. 7.1) are illustrated representatively by the thickness of the curve with the highest cross-section values.

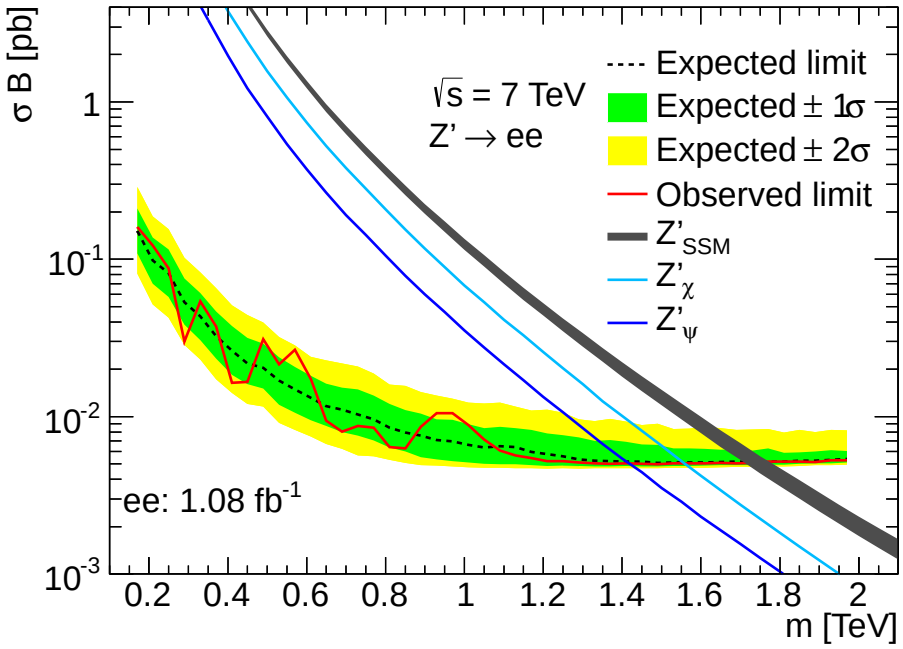

(a)

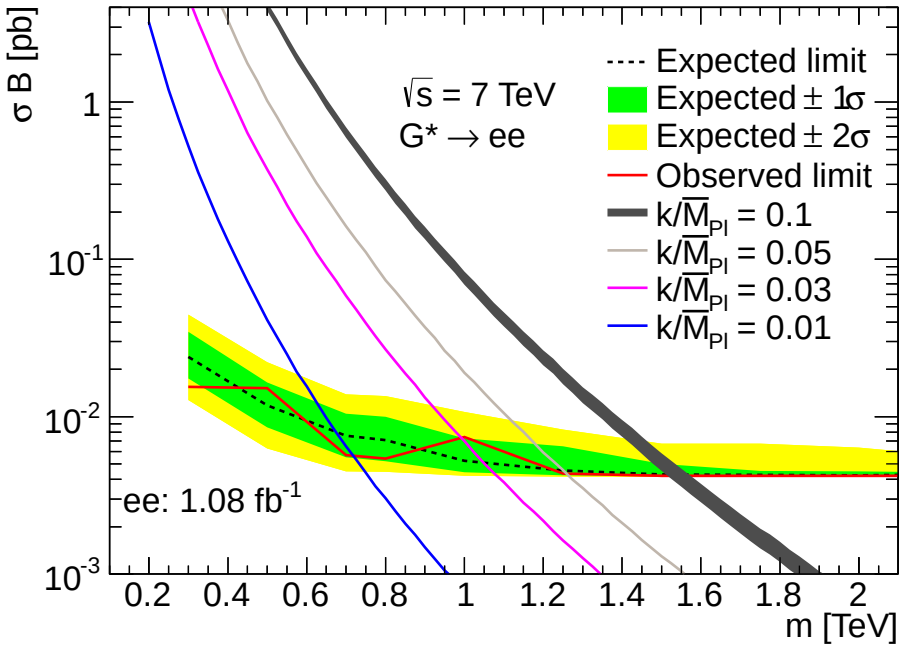

(b)

Figure 7.2: 95% C.L. limits on the cross-section times branching ratio for different Z' models (top) and the RS graviton with different values of $k/\bar{M}_{Pl}$ (bottom) as obtained from the dielectron invariant mass distribution.

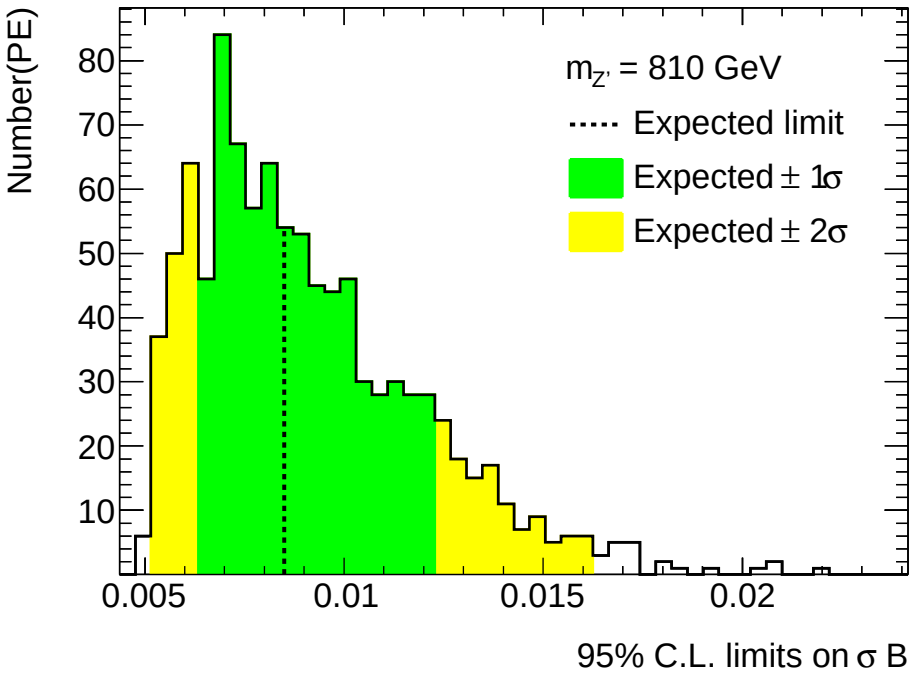

Figure 7.3: 95% C.L. limits from 1000 pseudo-data distributions for a test mass $m_{Z'} = 810$ GeV. The dashed line indicates the median of the distribution, which is quoted as expected limit, while the green and yellow areas show the 68% (1σ) and 95% (2σ) envelopes.

The lower mass limits for Z' bosons are listed in Table 7.2 and the limits on RS gravitons in Table 7.3. The expected and observed limits agree very well; small deviations are due to fluctuations in the data distribution.

	Observed mass limit [TeV]	Expected mass limit [TeV]
$Z'_{\rm SSM}$	1.74	1.74
Z'_{χ}	1.56	1.56
$Z'_{\rm S}$	1.52	1.52
Z'_{I}	1.49	1.49
Z'_{η}	1.46	1.45
$Z'_{\rm N}$	1.44	1.43
Z'_{ψ}	1.42	1.41

Table 7.2: Dielectron 95% C.L. mass limits on the $Z'_{\rm SSM}$ boson and the E_6 Z' bosons.

$k/\bar{M}_{Pl}$	Observed mass limit [TeV]	Expected mass limit [TeV]
0.1	1.55	1.54
0.05	1.26	1.25
0.03	0.99	1.05
0.01	0.72	0.67

Table 7.3: Dielectron 95% C.L. mass limits on the RS graviton with different values of $k/\bar{M}_{Pl}$.

7.4.2 Combination with muon channel

We also performed a search for resonances in the dimuon channel [6, 90]. No significant excess is found in the dimuon invariant mass spectrum (see Fig. 6.6): The p-value obtained by the LLR test is 24%. Electron-muon combined limits are obtained by extending the likelihood (Eq. 7.4) to also include the dimuon reconstructed invariant mass bins. By using $\sigma_{sig}B$ instead of N_{sig} (compare Eq. 7.6), different acceptances and integrated luminosities

are automatically taken into account. As before, statistical uncertainties are independent for each mass bin, but systematic uncertainties can be correlated between the bins, and therefore also between the different channels.

The expected and observed combined limits are shown in Fig. 7.4(a) for different Z' bosons and in Fig. 7.4(b) for RS gravitons with different values of $k/\bar{M}_{Pl}$. The theoretical curves are the same as for the dielectron limit (Fig. 7.2); the addition of the dimuon channel increases the dataset. The expected and observed limits on the pole masses of the Z'_{SSM} and different E_6 Z' bosons as well as RS gravitons with different values of $k/\bar{M}_{Pl}$ are shown in Tables 7.4 and 7.5. They differ slightly from the results in Ref. [6], as explained in Sec. 7.2.

	Observed mass limit [TeV]	Expected mass limit [TeV]
Z'_{SSM}	1.88	1.87
Z'_{χ}	1.68	1.67
Z'_{S}	1.64	1.63
Z'_{I}	1.60	1.59
Z'_{η}	1.58	1.57
Z'_{N}	1.56	1.55
Z'_{ψ}	1.54	1.53

Table 7.4: Combined dielectron and dimuon 95% C.L. mass limits on the Z'_{SSM} boson and the E_6 Z' bosons.

$k/\bar{M}_{Pl}$	Observed mass limit [TeV]	Expected mass limit [TeV]
0.1	1.67	1.66
0.05	1.37	1.35
0.03	1.09	1.12
0.01	0.72	0.72

Table 7.5: Combined dielectron and dimuon 95% C.L. mass limits on the RS graviton for different values of $k/\bar{M}_{Pl}$.

7.5 Discussion of results

The LHC collides protons with record CM energies, which allows us to probe the SM by searching for new physics in regions of phase-space that have never been tested before. The main result of this analysis is that using $\sim$1 fb^{-1} of ATLAS data we have not found any statistically significant peak-like excess over the SM background in the dielectron and dimuon invariant mass distributions.

7.5.1 Interpretation

The non-existence of any significant excess is quantified by limits on the cross-section times branching ratio for two representative models: The SSM, which predicts a spin-1 Z' boson, as well as the RS model, which predicts excitations with spin-2. Lower mass limits can be obtained from the respective σB limit curves for any spin-1/spin-2 model, as long as peak-shape and acceptance are similar.

In this analysis we use the Z'_{SSM} boson cross-section limit curve to set lower mass limits on the E_6 model for different choices of the mixing angle θ_{E_6}. We also set limits on the RS graviton mass for different couplings. These mass limits do not exclude either of the tested models, but significantly limit their allowed parameter space.

A reinterpretation of the spin-1 limits was done by ATLAS in the context of the Low Scale Technicolor model [39, 103] by setting mass limits on technimesons [104]. As can be seen in Fig. 7.5, the analysis excluded masses of 130-480 GeV for the techni-rho and techni-omega, dependent on the mass of the techni-pi. The limits just barely excluded the mass values ($\pi_T = 160$ GeV, $\rho_T = 290$ GeV) suggested in [105] as explanation of the Wjj excess seen by the CDF collaboration [106].

Other models predicting high-mass dielectron/dimuon resonances can also be restricted, for example little Higgs models [41, 107, 108].

7.5.2 Comparison to other analyses

The CMS collaboration also searched for dielectron/dimuon resonances in $\sim$1 fb^{-1} of LHC collision data [109]. The combined lower mass limits are shown in Tables 7.6 and 7.7. They are higher than the results of this analysis, mainly because of a larger acceptance in the muon channel due to a different muon detector design. Tables 7.6 and 7.7 also contain the limits set by the CDF and DØ collaborations at the Tevatron. Due to the higher CM energy at the LHC, ATLAS and CMS have a larger search range and obtain higher mass limits, even when less collision events are evaluated.

Looking at other ATLAS analyses, limits on the RS graviton were obtained in a diphoton resonance search using $\sim$2 fb^{-1} of LHC data [110]. The combination of dielectron, dimuon and diphoton channels yields a mass limit of 1.95 TeV for $k/\bar{M}_{Pl} = 0.1$.

Furthermore, both the ATLAS and CMS collaborations released preliminary updates to the dielectron/dimuon search using the full 2011 dataset ($\sim$5 fb^{-1}) [111, 112]. No significant excess was found and the results are shown in Tables 7.6 and 7.7.

Experiment	Channel	Luminosity [fb^{-1}]	Mass [TeV]	Reference
DØ	ee	5	1.023	[62]
CDF	$\mu\mu$	5	1.071	[61]
ATLAS (2011)	$ee + \mu\mu$	1	1.88	this analysis
CMS (2011)	$ee + \mu\mu$	1	1.940	[109]
ATLAS (2012)	$ee + \mu\mu$	5	2.21	[111]
CMS (2012)	$ee + \mu\mu$	5	2.320	[112]

Table 7.6: Observed limits on the lower mass of the Z'_{SSM} boson as obtained by different experiments.

Experiment	Channel	Luminosity [fb^{-1}]	Mass [TeV]	Reference
DØ	$ee + \gamma\gamma$	5	1.050	[53]
CDF	$ee + \gamma\gamma$	6 + 5	1.058	[113]
ATLAS (2011)	$ee + \mu\mu$	1	1.67	this analysis
CMS (2011)	$ee + \mu\mu$	1	1.780	[109]
ATLAS (2011)	$(ee + \mu\mu) + \gamma\gamma$	1 + 2	1.95	[6], [110]
CMS (2011)	$\gamma\gamma$	2	1.84	[114]
ATLAS (2012)	$ee + \mu\mu$	5	2.16	[111]
CMS (2012)	$ee + \mu\mu$	5	2.135	[112]

Table 7.7: Observed limits on the lower mass of the RS graviton with $k/\bar{M}_{Pl}$ =0.1, as obtained by different experiments.

Z' bosons and RS gravitons are also searched for by the ATLAS collaboration in the ditau and top-antitop channels [115].

7.5.3 Outlook

The sensitivity of the search for high-mass dilepton resonances towards lower cross-sections and higher pole masses increases with the number of recorded events and the CM energy. In 2012, the LHC will collide protons at $\sqrt{s}$ = 8 TeV, extending the accessible combined dielectron and dimuon signal range in 10 fb^{-1} of data to ∼2.7 TeV for a Z'_{SSM} boson [116]. This could vary depending on the achieved acceptance, of course.

Possible improvements to this analysis would be the consideration of interference between the Z' bosons and the DY background as well as variations of the width of the resonance for different models and different coupling values. Furthermore, angular distributions could be used to increase the sensitivity of the signal search, as done by the CDF collaboration in 2006 [117].

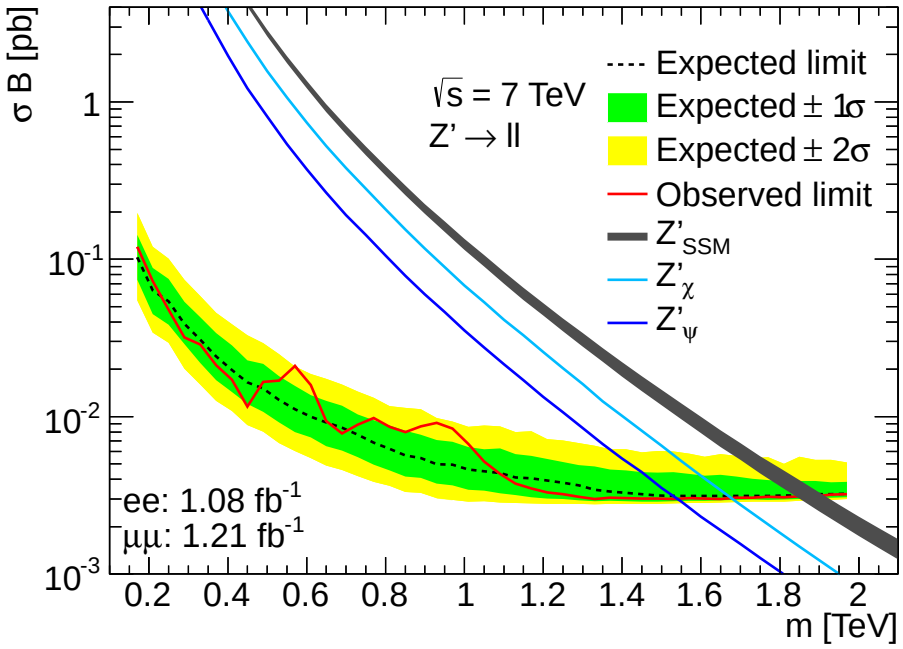

(a)

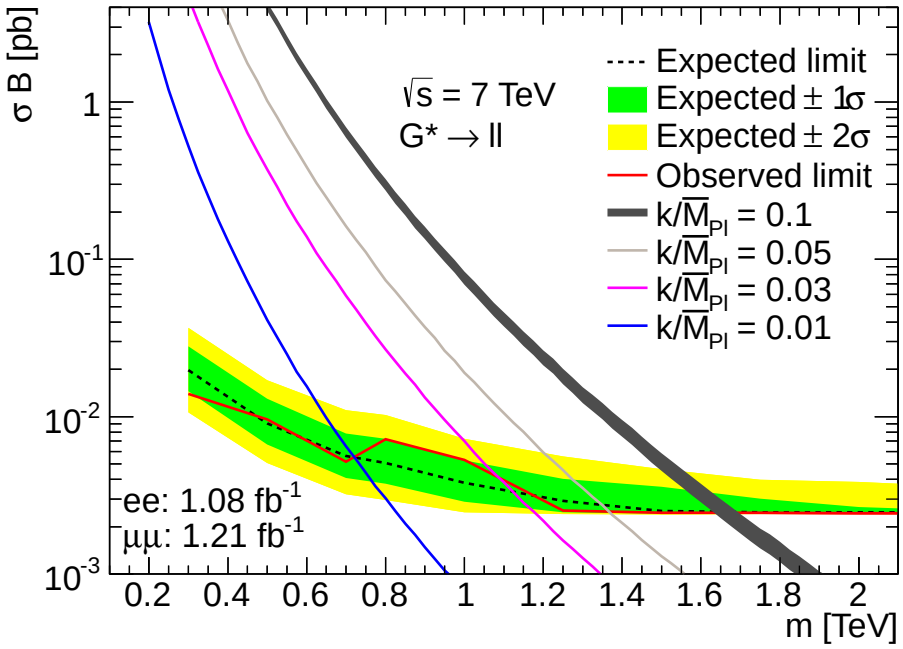

(b)

Figure 7.4: 95% C.L. limits on the cross-section times branching ratio for different Z' models (a) and the RS graviton with different values of $k/\bar{M}_{Pl}$ (b) as obtained from the dielectron and dimuon invariant mass distributions.

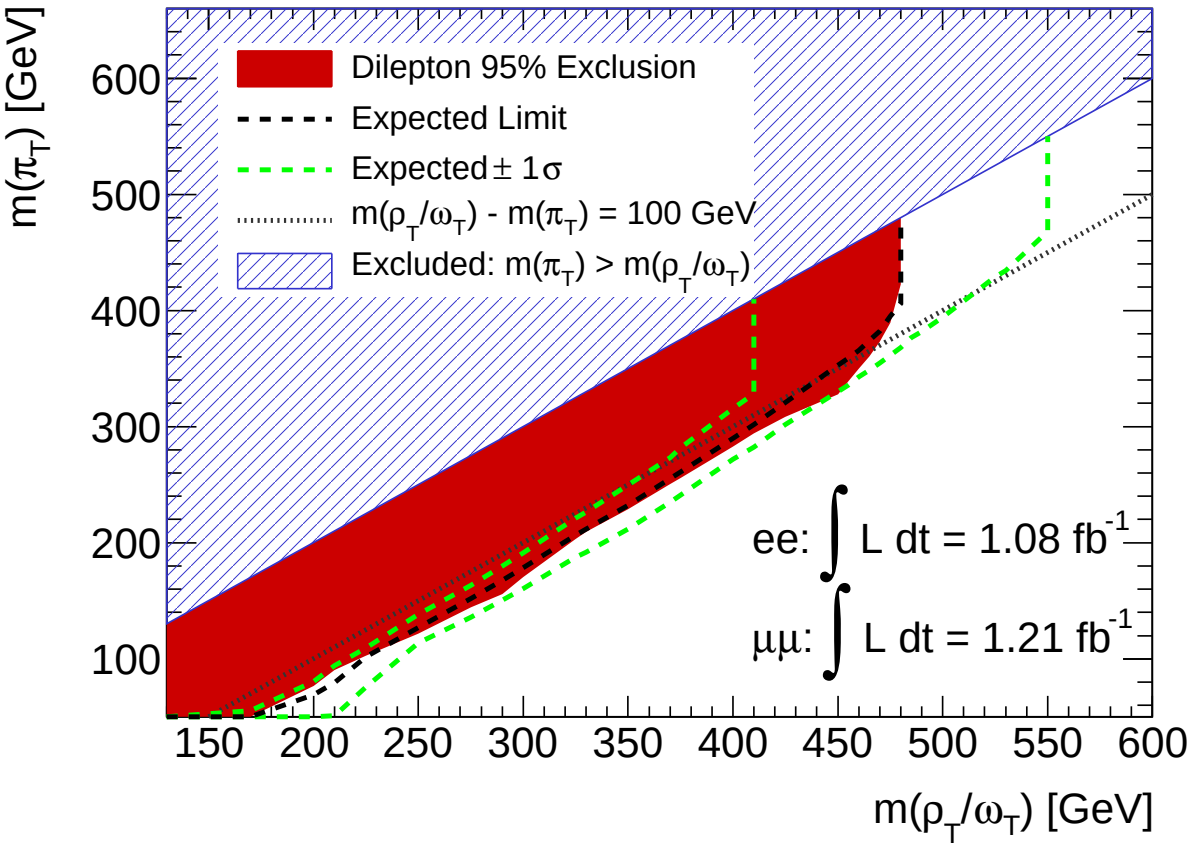

Figure 7.5: 2D limits on the masses of technimesons in the context of the Low Scale Technicolor model [39, 103]. The red area is the 95% CL excluded region depending on the assumed π_T and ρ_T/ω_T masses. The dashed line shows the expected limit with the green dashed lines showing the $\pm 1\sigma$ bands. The hashed region where $m(\pi_T) > m(\rho_T/\omega_T)$ is excluded by theory. This plot is taken from Ref. [104].

Chapter 8

Conclusion

We have performed a search for high-mass dielectron resonances in $\sim$1 fb^{-1} of proton-proton collision data. The collisions were produced at a center-of-mass energy of $\sqrt{s} = 7$ TeV by the Large Hadron Collider, CERN, Switzerland, between March and June 2011 and recorded with the ATLAS detector. The dielectron invariant mass spectrum from data is compared to Standard Model expectations which are predicted using simulated samples and estimates from data in control regions. No statistically significant excess is found: The dielectron invariant mass spectrum contains no evidence for a high-mass resonance due to new physics.

We know that the Standard Model cannot describe all aspects of the fundamental particles and interactions that make up our universe. The LHC with its record collision energies gives us the unique opportunity to look for additional particles and forces, allowing us to probe the Standard Model's validity in so-far untested regions of phase-space. There are possible reasons why we have not seen any indication of physics beyond the Standard Model in this analysis:

- The so-far unknown additional particles are too heavy to produce a dielectron resonance

peak at the current CM energy. This year, the LHC will run with energies of $\sqrt{s} =$ 8 TeV, and in a couple of years with $\sqrt{s} = 14$ TeV, increasing our search region considerably.

- The rate of interactions not included in the Standard Model is even lower than we assume. More collisions, as planned to be produced in the following years by the LHC, will allow us to test for even rarer processes.

- There are many proposed extensions to the Standard Model and not all of them contain dielectron or dimuon resonances within our reach, instead predicting different event signatures. A large number of analyses at the LHC and other research facilities look for different ways new physics could manifest itself.

Since no significant excess is found, in combination with the dimuon analysis, 95% confidence level lower limits are set on the masses of the Sequential Standard Model Z' boson (1.88 TeV), E_6 Z' bosons (1.54 - 1.68 TeV) as well as the Randall-Sundrum graviton (0.72 - 1.67 TeV) for couplings ranging from $k/\bar{M}_{Pl} = 0.01$ to 0.1.

These limits restrict the allowed parameter space for the models under consideration and other proposed extensions to the Standard Model, constituting an important step in our quest for understanding elementary particles and forces.

APPENDIX

Appendix A

Determination of identification efficiency correction factors with Tag-and-Probe

The differences between electron signatures in data and simulated samples (compare Sec. 5.3) make it necessary to correct the simulation for an unbiased comparison between data and SM backgrounds. This section shows how the factors for correcting identification efficiencies of electrons are obtained using the Tag-and-Probe method.

A.1 Definitions

The efficiency for true electrons passing a cut Y to also pass a cut X is defined as

$$\epsilon_X = \frac{\text{\#electrons passing Y and X}}{\text{\#electrons passing Y}}. \tag{A.1}$$

Efficiency scale factors (SF) are the ratio between the efficiencies (ϵ) for true electrons in data and in simulated samples (see Eq. 5.2).

Identification efficiencies are calculated with respect to reconstructed electron candidates and are binned in η and E_{T} (compare Sec. 4.4).

A.2 Method

The biggest challenge in the efficiency measurement consists of getting a sample of electrons from data on which to perform the efficiency determination. This sample should consist of real electrons, not QCD jets, and no cuts should be applied to these electrons that could bias the efficiency measurement. The method of choice is the Tag-and-Probe method, which makes use of the characteristic signatures of the $Z \to ee$ and $W \to e\nu$ decays. In the case of Z Tag-and-Probe, very strict cuts are applied on one of the two decay electrons (called "tag"), and the second electron candidate ("probe") is used for the measurements. See Fig. 2.1 for an illustration of Z boson production and decay. Additional cuts which ensure that the invariant mass of the two objects is close to the Z boson mass, and that the two electrons have opposite charge, greatly enhance the chance that the second electron candidate is a real electron while remaining unbiased. A simulated $Z \to ee$ sample, on which the same tag and probe selection is applied as in data, is used for the denominator of the SF. The W Tag-and-Probe method, which is not discussed here, uses the $E_{\mathrm{T}}^{\mathrm{miss}}$ from the neutrino as the tag, and the single electron in the event as the probe.

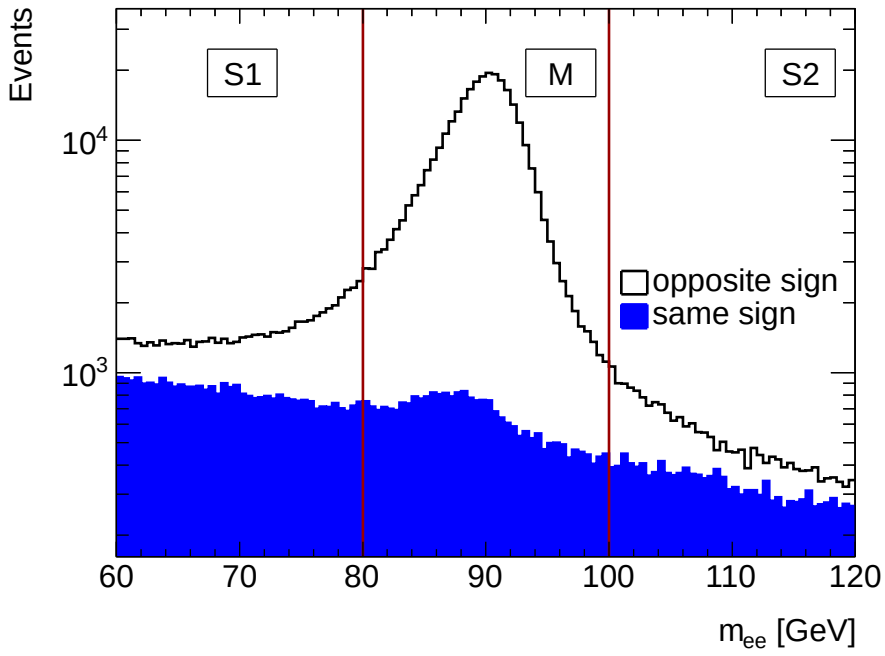

(a)

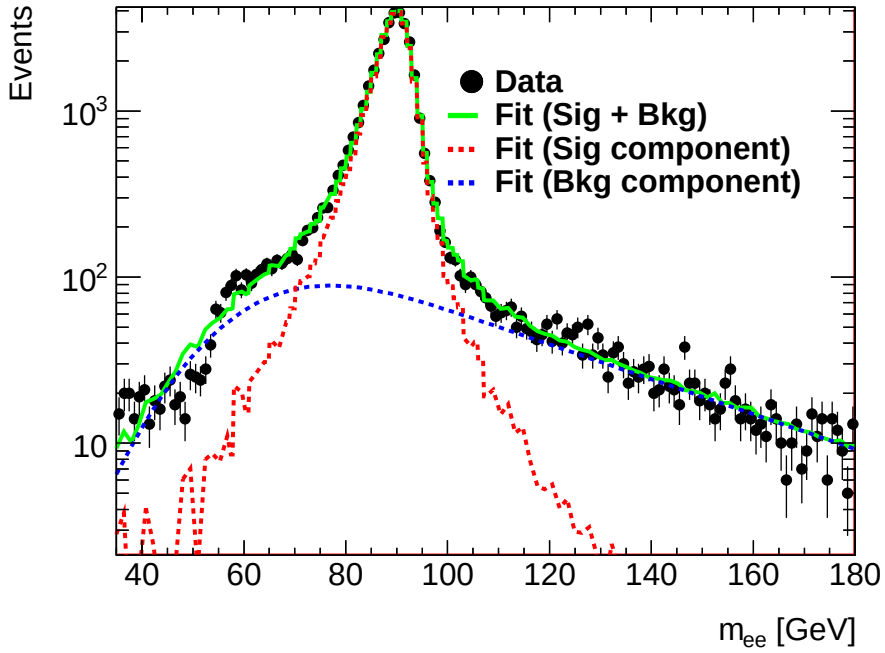

(b)

Figure A.1: Illustration of the QCD jet background estimation under the Z peak. Both plots show tag and probe pairs in which the tag is a Tight electron and the probe is a reconstructed electron candidate. (a) shows the sideband method applied for the efficiency determination in η bins, (b) shows as an example a 2-component fit applied to pairs in which the probe fulfills 35 GeV $\leq E_{\mathrm{T}} \leq$ 40 GeV.

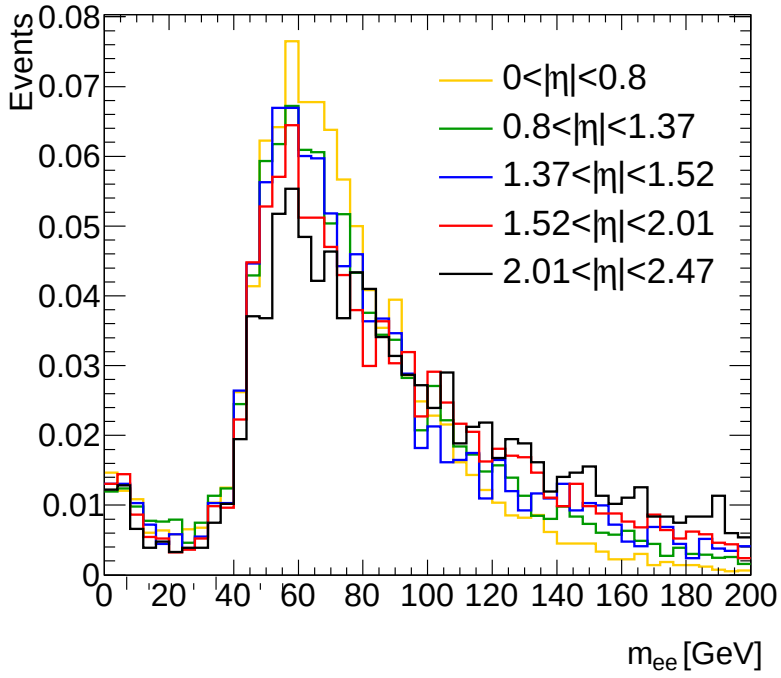

(a)

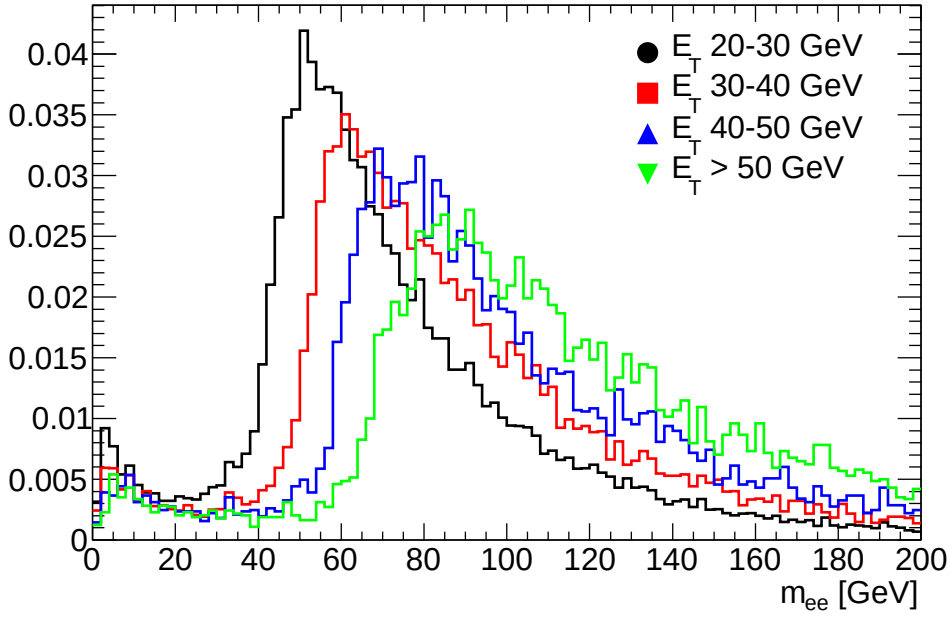

(b)

Figure A.2: Invariant mass distribution of tag and probe pairs for QCD jet background from a simulated sample, (a) for bins in η, (b) for bins in E_{T} [118]. The distributions are normalized to unit area.

A.3 Background estimation

Identification efficiencies are determined with respect to reconstructed electron candidates. In spite of the strict cuts on the tag electron and additional event cuts, there is a non-negligible background of QCD jets in the probe sample, coming from QCD multijet production as well as the W + jets process. Since we are interested in the identification efficiency of real electrons and not jets, this background needs to be accounted for.

In order to subtract the jet background for the identification efficiency measurements, two data-driven methods are employed, depending on whether the efficiencies are binned in η or E_{T}. These methods are chosen because they perform best in closure studies where the background is known [118]. In both cases, the discriminating variable is the tag and probe invariant mass coming from the characteristic shape of the Z peak (compare Fig. A.1).

Figure A.2(a) shows the jet background taken from simulation for bins in η. Although the statistics are low, this figure demonstrates that the background shape between 60 and 120 GeV does not change very much for bins in η. We assume a linear shape in this window and subtract it using a sideband method as illustrated in Fig. A.1(a): For each η bin, the number of oppositely charged pairs (M) is counted in the signal window around the Z pole, and the number of same-sign pairs is determined in the two sidebands ($S1$, $S2$). The number of real electron pairs N_{sig} in the signal region is then calculated as

$$N_{sig} = M - \frac{S1 + S2}{2}, \tag{A.2}$$

if the windows have the same width, and otherwise as

$$N_{sig} = M - \left[\left(\frac{S2}{w_2} - \frac{S1}{w_1} \right) \frac{w_M^2 + w_1 w_2}{w_1 + w_M + w_2} + \frac{S1\ w_M}{w_1} \right], \tag{A.3}$$

where $w_{1(2)}$ is the width of sideband 1(2) and w_M is the width of the middle band. It is assumed that for QCD jets the number of events in which tag and probe pairs have the same charge is equal to the number of events in which tag and probe pairs have opposite charges. This is in contrast to electron pairs from the decay of the Z boson which should always have opposite charges. It is not possible to simply subtract the same-signed pairs under the Z peak because of the small same-sign peak (compare Fig. A.1(a)), which is due to a very low ($< 2\%$) rate of charge misidentification affecting electrons from the Z boson decay.

The background subtraction for efficiencies in E_{T} bins is more complicated due to the more complex shape of the QCD jet background (see Fig. A.2(b)). Figure A.1(b) shows the invariant mass distribution for tag and probe pairs where the probe is a reconstructed electron candidate with 35 GeV $\leq E_{\mathrm{T}} \leq$ 40 GeV and the tag is a Tight electron. The number of real electrons in the signal region is estimated by a 2-component fit, with the QCD jet background modeled by a function (a convolution of a Gaussian and an exponential). The Z peak shape is estimated in two ways: by a function (Breit-Wigner convoluted with Crystal-Ball) as well as by a simulated $Z \to ee$ template, as shown in Fig. A.1(b).

The QCD jet background is subtracted independently for every η/E_{T} bin as well as for the numerator and denominator of the efficiency calculation. For the numerator, where the probe is requested to be an identified electron, the background contamination is much lower than in the denominator, where the probe is only a reconstructed electron candidate.

Since a $Z \to ee$ sample is used, no QCD multijet background is subtracted in the simu-

lation. However, in order to reject jets produced in association with the Z boson, the probe is required to be a true electron from the Z boson decay (this includes electrons that are converted from photons radiated by the decay electrons).

A.4 Systematic uncertainty

The dominant source of systematic uncertainty in the efficiency determination is the QCD jet background estimate. The uncertainty has two components. The first part is determined by a closure test, performed on a simulated signal and background sample, showing the overall bias of the two background estimation methods. For the sideband method this bias is $\sim$2% in each η bin, while for E_{T} bins it varies between $\sim$3% in the low mass bins to $< 1\%$ for the highest E_{T} bins where the QCD jet background is much lower. The second part of the systematic uncertainty is obtained by varying the background estimation method itself. For both the sideband and the fit method, the requirement on the tag is varied, changing the QCD jet background yield. Furthermore, the signal window around the Z peak is changed. In addition, the ranges of the sidebands are modified for the sideband method. In the fit method, the fit range is varied, and the signal shape is estimated by different fit functions and templates. The systematic uncertainty from these variations is 1-2% in η and 4-1% in E_{T}.

A.5 Results

The identification efficiencies obtained from data and a simulated $Z \to ee$ sample, as well as the SF for electrons fulfilling the Medium requirement (compare Sec. 4.4) are shown in

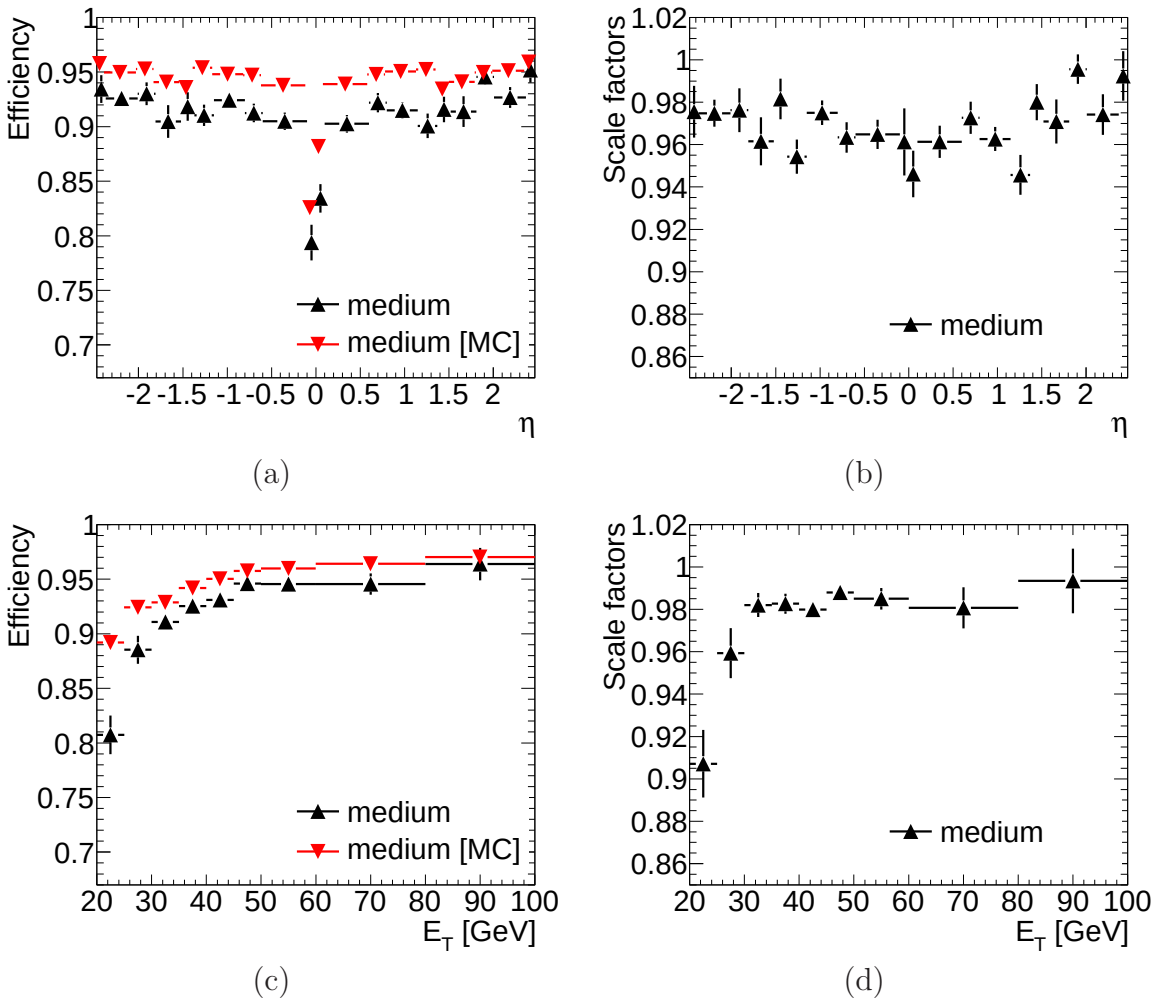

Figure A.3: Identification efficiencies obtained from data and a simulated $Z \to ee$ sample, as well as calculated SF for electrons fulfilling the Medium requirements (compare Sec. 4.4). The uncertainties are statistical and systematic, but the closure test bias is not included.

Fig. A.3. The uncertainties include statistical and systematic components with the exception of the closure test bias. The identification efficiency measured in data is lower than in the simulated $Z \to ee$ sample, which results in correction factors lower than 1. For physics analyses, these numbers are combined with SF obtained from W Tag-and-Probe and are factorized into SF in η with E_{T} corrections.

Figure A.4 shows efficiencies and SF for the additional requirements in this analysis (B-layer cut as well as calorimeter isolation), calculated with respect to Medium electrons. The

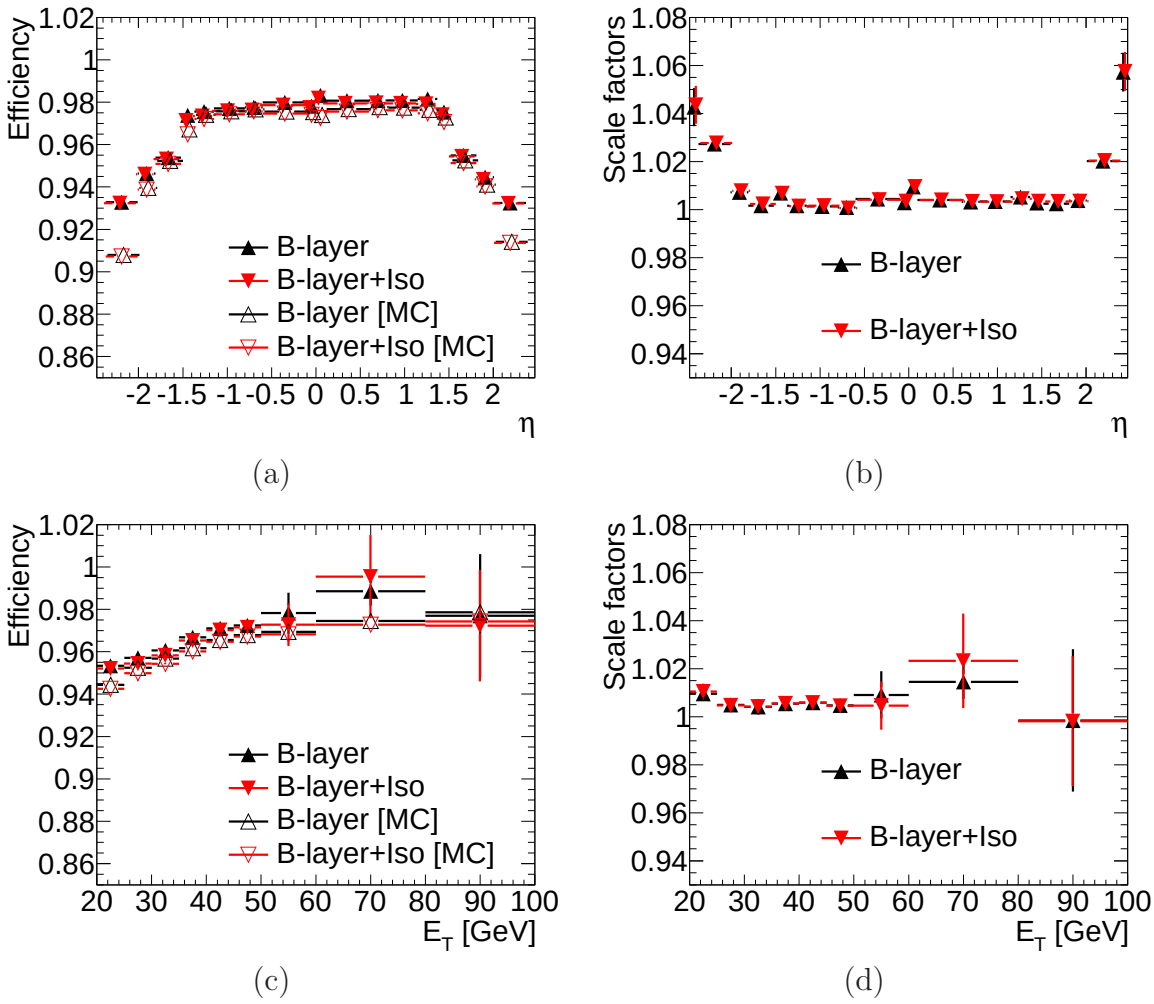

Figure A.4: Efficiencies and SF for the B-layer cut as well as calorimeter isolation, calculated with respect to Medium electrons. The uncertainties are statistical only.

uncertainties are statistical only. The B-layer efficiency drop for high $|\eta|$ is larger in the simulation than in data, which is reflected in the SF. The additional SF are almost flat in E_{T}.

A.6 Limitations and improvements

The efficiencies and SF were obtained with a fraction of the dataset available in 2011. More statistics will allow an extension of the E_{T} range, reducing the uncertainty on efficiencies at

high invariant masses. The E_{T} range can also be extended by using high invariant mass DY events, however, for this an alternative way of subtracting the background is needed since the characteristic Z peak cannot be used. In W Tag-and-Probe, the calorimeter isolation has already been shown to have enough discriminating power [34].

More data will also enable us to produce 2D SF binned in (η, E_{T}), which yield values with smaller uncertainties, as the current factorization into η and E_{T} bins is only an approximation. With higher statistics, and 2D bins, the current approximation of a linear QCD background shape is no longer valid.

Another method to improve the efficiency determination is to reduce the QCD jet background by applying stricter tag requirements and additional cuts to the events, for example a maximum $E_{\mathrm{T}}^{\mathrm{miss}}$ cut to reduce the $W+\mathrm{jets}$ contribution. These additional cuts must not bias the probe sample, though.

BIBLIOGRAPHY

BIBLIOGRAPHY

[1] UA1 Collaboration, *Experimental observation of lepton pairs of invariant mass around 95 GeV/c^2 at the CERN SPS Collider*, Phys. Lett. **B126** (1983) 398–410.

[2] UA2 Collaboration, *Evidence for Z0 $\rightarrow$ e+ e- at the CERN anti-p p Collider*, Phys. Lett. **B129** (1983) 130–140.

[3] D. London and J. L. Rosner, *Extra Gauge Bosons in E(6)*, Phys. Rev. **D34** (1986) 1530.

[4] P. Langacker, *The Physics of Heavy Z' Gauge Bosons*, Rev. Mod. Phys. **81** (2009) 1199–1228.

[5] L. Randall and R. Sundrum, *A large mass hierarchy from a small extra dimension*, Phys. Rev. Lett. **83** (1999) 3370–3373.

[6] ATLAS Collaboration, *Search for dilepton resonances in pp collisions at $\sqrt{s}$ = 7 TeV with the ATLAS detector*, Phys. Rev. Lett. **107** (2011) 272002.

[7] UA1 Collaboration, *Experimental Observation of Isolated Large Transverse Energy Electrons with Associated Missing Energy at $s^{1/2}$ = 540 GeV*, Phys. Lett. **B122** (1983) 103–116.

[8] UA2 Collaboration, *Observation of Single Isolated Electrons of High Transverse Momentum in Events with Missing Transverse Energy at the CERN anti-p p Collider*, Phys. Lett. **B122** (1983) 476–485.

[9] S. Glashow, *Partial-symmetries of weak interactions*, Nucl. Phys. (1961) 579–588.

[10] S. Weinberg, *A Model of Leptons*, Phys. Rev. Lett. **19** (1967) 1264–1266.

[11] A. Salam, *Weak and Electromagnetic Interactions*. Proceedings of the Eighth Nobel Symposium. Almquist & Wiksell, 1968.

[12] P. Langacker, *The standard model and beyond*. Series in high energy physics, cosmology, and gravitation. CRC Press/Taylor & Francis, 2010.

[13] E. Noether, *Invariant variational problems (Invariante Variationsprobleme)*, Nachr. v. d. Ges. d. Wiss. zu Göttingen (1918) 235–257.

[14] Particle Data Group, *The Review of Particle Physics*, J. Phys. **G37** (2010) 075021 and 2011 partial update for the 2012 edition.

[15] J. C. Collins, D. E. Soper, and G. F. Sterman, *Factorization of Hard Processes in QCD*, Adv. Ser. Direct. High Energy Phys. **5** (1988) 1–91.

[16] J. Griffiths, *Introduction to Elementary Particle Physics*. Wiley VCH, 2008.

[17] H.-L. Lai et al., *New parton distributions for collider physics*, Phys. Rev. **D82** (2010) 074024.

[18] A. Martin et al., *Parton distributions for the LHC*, Eur. Phys. J. **C63** (2009) 189–285.

[19] A. Sherstnev and R. Thorne, *Parton Distributions for LO Generators*, Eur. Phys. J. **C55** (2008) 553–575.

[20] T. G. Rizzo, *Z' phenomenology and the LHC*, SLAC-PUB-12129 (2006).

[21] S. Dittmaier and M. Huber, *Radiative corrections to the neutral-current Drell-Yan process in the Standard Model and its minimal supersymmetric extension*, JHEP **01** (2010) 060.

[22] B. Cleveland et al., *Measurement of the solar electron neutrino flux with the Homestake chlorine detector*, Astrophys. J. **496** (1998) 505–526.

[23] SNO Collaboration, *Measurement of the rate of $\nu_e + d \to p + p + e^-$ interactions produced by B-8 solar neutrinos at the Sudbury Neutrino Observatory*, Phys. Rev. Lett. **87** (2001) 071301.

[24] KamLAND Collaboration, *First results from KamLAND: Evidence for reactor anti-neutrino disappearance*, Phys. Rev. Lett. **90** (2003) 021802.

[25] J. N. Bahcall and H. Bethe, *A Solution of the solar neutrino problem*, Phys. Rev. Lett. **65** (1990) 2233–2235.

[26] S. Weinberg, *The cosmological constant problem*, Rev. Mod. Phys. **61** (1989) 1–23.

[27] Supernova Search Team, *Observational evidence from supernovae for an accelerating universe and a cosmological constant*, Astron. J. **116** (1998) 1009–1038.

[28] Supernova Cosmology Project, *Measurements of Omega and Lambda from 42 high redshift supernovae*, Astrophys. J. **517** (1999) 565–586.

[29] J. Aubert et al., *Experimental Observation of a Heavy Particle J*, Phys. Rev. Lett. **33** (1974) 1404–1406.

[30] SLAC-SP-017 Collaboration, *Discovery of a Narrow Resonance in e+ e- Annihilation*, Phys. Rev. Lett. **33** (1974) 1406–1408.

[31] E. Cazzoli et al., *Evidence for ΔS=-ΔQ Currents or Charmed-Baryon production by Neutrinos*, Phys. Rev. Lett. **34** (1975) 1125–1128.

[32] G. Goldhaber et al., *Observation in e^+e^- Annihilation of a Narrow State at 1865 MeV/c^2 decaying to $K\pi$ and $K\pi\pi\pi$*, Phys. Rev. Lett. **37** (1976) 255–259.

[33] I. Peruzzi et al., *Observation of a Narrow Charged State at 1876 MeV/c^2 decaying to an Exotic Combination of $K\pi\pi$*, Phys. Rev. Lett. **37** (1976) 569–571.

[34] ATLAS Collaboration, *Electron performance measurements with the ATLAS detector using the 2010 LHC proton-proton collision data*, Eur. Phys. J. **C72** (2012) 1909.

[35] J. Wess and B. Zumino, *Supergauge Transformations in Four-Dimensions*, Nucl. Phys. **B70** (1974) 39–50.

[36] A. Salam and J. Strathdee, *Supergauge Transformations*, Nucl. Phys. **B76** (1974) 477–482.

[37] P. Fayet, *Supergauge Invariant Extension of the Higgs Mechanism and a Model for the electron and Its Neutrino*, Nucl. Phys. **B90** (1975) 104–124.

[38] K. D. Lane and E. Eichten, *Two Scale Technicolor*, Phys. Lett. **B222** (1989) 274.

[39] K. D. Lane and S. Mrenna, *Collider phenomenology of technihadrons in the technicolor straw man model*, Phys. Rev. **D67** (2003) 115011.

[40] A. Belyaev et al., *Technicolor Walks at the LHC*, Phys. Rev. **D79** (2009) 035006.

[41] N. Arkani-Hamed, A. G. Cohen, and H. Georgi, *Electroweak symmetry breaking from dimensional deconstruction*, Phys. Lett. **B513** (2001) 232–240.

[42] E. C. G. Stueckelberg, *Interaction forces in electrodynamics and in the field theory of nuclear forces*, Helv. Phys. Acta **11** (1938) 299–328.

[43] R. Mohapatra, *Unification and Supersymmetry. The Frontiers of Quark-Lepton Physics*. Springer, 1986.

[44] P. Langacker, *Grand Unified Theories and Proton Decay*, Phys. Rept. **72** (1981) 185.

[45] J. L. Hewett and T. G. Rizzo, *Low-Energy Phenomenology of Superstring Inspired E(6) Models*, Phys. Rept. **183** (1989) 193.

[46] T. Sjöstrand, S. Mrenna, and P. Skands, *PYTHIA 6.4 physics and manual*, JHEP **0605** (2006) 026.

[47] I. Antoniadis, *A Possible new dimension at a few TeV*, Phys. Lett. **B246** (1990) 377–384.

[48] A. Einstein, *The foundation of the general theory of relativity*, Annalen Phys. **49** (1916) 769–822.

[49] N. Arkani-Hamed, S. Dimopoulos, and G. Dvali, *The Hierarchy problem and new dimensions at a millimeter*, Phys. Lett. **B429** (1998) 263–272.

[50] P. Traczyk and G. Wrochna, *Search for Randall-Sundrum graviton excitations in the CMS experiment*, `arXiv:hep-ex/0207061 (2002)`.

[51] H. Davoudiasl, J. L. Hewett, and T. G. Rizzo, *Phenomenology of the Randall-Sundrum Gauge Hierarchy Model*, Phys. Rev. Lett. **84** (2000) 2080–2083.

[52] H. Davoudiasl, J. L. Hewett, and T. G. Rizzo, *Experimental probes of localized gravity: On and off the wall*, Phys. Rev. **D63** (2001) 075004.

[53] D0 Collaboration, *Search for Randall-Sundrum gravitons in the dielectron and diphoton final states with 5.4 fb-1 of data from ppbar collisions at* $\sqrt{s}$*=1.96 TeV*, Phys. Rev. Lett. **104** (2010) 241802.

[54] OPAL Collaboration, *Tests of the standard model and constraints on new physics from measurements of fermion pair production at 189 GeV to 209 GeV at LEP*, Eur. Phys. J. **C33** (2004) 173–212.

[55] DELPHI Collaboration, *Measurement and interpretation of fermion-pair production at LEP energies above the Z resonance*, Eur. Phys. J. **C45** (2006) 589–632.

[56] L3 Collaboration, *Measurement of hadron and lepton-pair production in* e^+e^- *collisions at* $\sqrt{s} = 192$ *GeV to 208 GeV at LEP*, Eur. Phys. J. **C47** (2006) 1–19.

[57] ALEPH Collaboration, *Fermion pair production in* e^+e^- *collisions at 189-209 GeV and constraints on physics beyond the standard model*, Eur. Phys. J. **C49** (2007) 411–437.

[58] P. Langacker, *Z' Physics at the LHC*, `arXiv:hep-ph/0911.4294 (2009)`.

[59] ATLAS Collaboration, *Search for high mass dilepton resonances in pp collisions at* $\sqrt{s}$*=7 TeV with the ATLAS experiment*, Phys. Lett. **B700** (2011) 163–180.

[60] CMS Collaboration, *Search for Resonances in the Dilepton Mass Distribution in pp Collisions at* $\sqrt{s}$ *= 7 TeV*, JHEP **05** (2011) 093.

[61] CDF Collaboration, *Search for High Mass Resonances Decaying to Muon Pairs in* $\sqrt{s} = 1.96$ *TeV* $p\bar{p}$ *Collisions*, Phys. Rev. Lett. **106** (2011) 121801.

[62] D0 Collaboration, *Search for a heavy neutral gauge boson in the dielectron channel with 5.4* fb^{-1} *of* $p\bar{p}$ *collisions at* $\sqrt{s} = 1.96$ *TeV*, Phys. Lett. **B695** (2011) 88–94.

[63] C. Hays, A. V. Kotwal, and O. Stelzer-Chilton, *New Techniques in the Search for* Z' *Bosons and Other Neutral Resonances*, Modern Physics Letters **A24** (2009) 2387, and references therein.

[64] O. S. Brüning et al., *LHC Design Report. 1. The LHC Main Ring.* CERN, Geneva, 2004.

[65] O. S. Brüning et al., *LHC Design Report. 2. The LHC infrastructure and general services*. CERN, Geneva, 2004.

[66] M. Benedikt et al., *LHC Design Report. 3. The LHC injector chain*. CERN, Geneva, 2004.

[67] LHC facts. `http://www.lhc-facts.ch`. Accessed: 10/06/2011.

[68] ATLAS Collaboration, *The ATLAS Experiment at the Large Hadron Collider*, JINST **3** (2008) S08003.

[69] ATLAS media. `http://www.atlas.ch/photos/index.html`. Accessed: 10/06/2011.

[70] S. Ballestrero, W. Vandelli, and G. Avolio, *ATLAS TDAQ system: current status and performance*, ATL-DAQ-PROC-2011-020 (2011).

[71] ATLAS Collaboration, *Readiness of the ATLAS Liquid Argon Calorimeter for LHC Collisions*, Eur. Phys. J. **C70** (2010) 723–753.

[72] P. Pralavorio, *The ATLAS liquid argon electromagnetic calorimeter*, AIP Conf. Proc. **549** (2002) 872–874.

[73] R. Achenbach et al., *The ATLAS level-1 calorimeter trigger*, JINST **3** (2008) P03001.

[74] T. Fonseca-Martin et al., *Event reconstruction algorithms for the ATLAS trigger*, J. Phys. Conf. Ser. **119** (2008) 022022.

[75] ATLAS Collaboration, *Expected electron performance in the ATLAS experiment*, ATL-PHYS-PUB-2011-006 (2011).

[76] W. Lampl et al., *Calorimeter Clustering Algorithms: Description and Performance*, ATL-LARG-PUB-2008-002, ATL-COM-LARG-2008-003 (*unpublished*) (2008).

[77] T. Cornelissen et al., *The new ATLAS track reconstruction (NEWT)*, J. Phys. Conf. Ser. **119** (2008) 032014.

[78] ATLAS Collaboration, *Expected Performance of the ATLAS Experiment - Detector, Trigger and Physics*, `arXiv:0901.0512 (2009) [hep-ex]`.

[79] H. Abreu et al., *Performance of the electronic readout of the ATLAS liquid argon calorimeters*, JINST **5** (2010) P09003.

[80] ATLAS E/gamma group, *Energy Scale and Resolution recommendations*, `https://twiki.cern.ch/twiki/bin/view/AtlasProtected/EnergyScaleResolutionRecommendations`. *ATLAS internal*, accessed: 07/01/2011.

[81] N. Morange et al., *Study and validation of the BCID of the L1Calo at very high transverse energies*, ATL-DAQ-INT-2011-001, *unpublished* (2011).

[82] G. Corcella et al., *HERWIG6: an event generator for hadron emission reactions with interfering gluons (including supersymmetric processes)*, JHEP **0101** (2001) 010.

[83] M. L. Mangano et al., *ALPGEN, a generator for hard multiparton processes in hadronic collisions*, JHEP **07** (2003) 001.

[84] S. Frixione and B. Webber, *Matching NLO QCD computations and parton shower simulations*, JHEP **0206** (2002) 029.

[85] GEANT4 Collaboration, *GEANT4: A simulation toolkit*, Nucl. Instrum. Meth. **A506** (2003) 250.

[86] J. Pumplin et al., *New generation of parton distributions with uncertainties from global QCD analysis*, JHEP **0207** (2002) 012.

[87] P. M. Nadolsky et al., *Implications of CTEQ global analysis for collider observables*, Phys. Rev. **D78** (2008) 013004.

[88] S. Moch and P. Uwer, *Theoretical status and prospects for top-quark pair production at hadron colliders*, Phys. Rev. **D78** (2008) 034003.

[89] U. Langenfeld, S. Moch, and P. Uwer, *New results for $t\bar{t}$ production at hadron colliders*, `arXiv:0907.2527 (2009) [hep-ph]`.

[90] A. Abdelaim et al., *Search for high-mass dilepton resonances in pp collisions at $\sqrt{s}$ = 7 TeV (2011 update for the EPS conference)*, ATL-COM-PHYS-2011-770, *unpublished* (2011).

[91] M. C. Kumar et al., *Direct photon pair production at the LHC to $\mathcal{O}\alpha_S$ in TeV scale gravity models*, Nucl. Phys. **B818** (2009) 28.

[92] M. C. Kumar, P. Mathews, and V. Ravindran, *PDF and scale uncertainties of various DY distributions in ADD and RS models at hadron colliders*, Eur. Phys. J. **C49** (2007) 599.

[93] O. Arnaez, *Talk at LPCC Meeting, ATLAS: Data and MC comparisons for EM calorimeter, electrons and photons*, `https://indico.cern.ch/getFile.py/access?contribId=1&sessionId=0&resId=0&materialId=slides&confId=144956`. Accessed: 09/01/2011.

[94] *Electron object quality*, `https://twiki.cern.ch/twiki/bin/view/AtlasProtected/LArCleaningAndObjectQuality`. *ATLAS internal*, accessed: 01/07/2012.

[95] Public Plots for Phys. Rev. Lett. 107. `https://atlas.web.cern.ch/Atlas/GROUPS/PHYSICS/PAPERS/EXOT-2011-06/`. Accessed: 01/09/2012.

[96] CDF Collaboration, *Search for new particles decaying into dijets in proton-antiproton collisions at* $s^{1/2} = 1.96$ *TeV*, Phys. Rev. **D79** (2009) 112002.

[97] ATLAS Collaboration, *Search for New Particles in Two-Jet Final States in 7 TeV Proton-Proton Collisions with the ATLAS Detector at the LHC*, Phys. Rev. Lett. **105** (2010) 161801.

[98] A. Caldwell, D. Kollar, and K. Kröninger, *BAT - The Bayesian Analysis Toolkit*, Comput. Phys. Commun. **180** (2009) 2197.

[99] A. Abdelamin et al., *Limit Setting and Signal Extraction Procedures in the Search for Narrow Resonances Decaying into Leptons at ATLAS*, ATL-COM-PHYS-2011-085, *unpublished* (2010).

[100] J. Neyman and E. Pearson, *On the problem of the most efficient tests of statistical hypotheses*, Phil. Trans. Roy. Soc., London, Series A **231** (1933) 289–337.

[101] G. Choudalakis, *On hypothesis testing, trials factor, hypertests and the BumpHunter*, `arXiv:1101.0390v2 (2011) [physics.data-an]`.

[102] T. Bayes and R. Price, *An essay towards solving a problem in the doctrine of chances*, Phil. Trans. of the Royal Soc. of London **53** (1763) 370–418.

[103] K. D. Lane, *Technihadron production and decay in low-scale technicolor*, Phys. Rev. **D60** (1999) 075007.

[104] ATLAS Collaboration, *Search for technihadrons in pp collisions at $\sqrt{s}$=7 TeV with the ATLAS detector*, ATLAS-CONF-2011-125 (2011).

[105] E. J. Eichten, K. Lane, and A. Martin, *Technicolor Explanation for the CDF W_{jj} Excess*, Phys. Rev. Lett. **106** (2011) 251803.

[106] CDF Collaboration, *Invariant Mass Distribution of Jet Pairs Produced in Association with a W boson in $p\bar{p}$ Collisions at $\sqrt{s} = 1.96$ TeV*, Phys. Rev. Lett. **106** (2011) 171801.

[107] G. Azuelos et al., *Exploring little Higgs models with ATLAS at the LHC*, Eur. Phys. J. **C39S2** (2005) 13–24.

[108] J. Boersma, *Direct search limits on the Littlest Higgs model*, Phys. Rev. **D74** (2006) 115008.

[109] CMS Collaboration, *Search for Resonances in the Dilepton Mass Distribution in pp Collisions at $\sqrt{s}$ = 7 TeV*, CMS-PAS-EXO-11-019 (2011).

[110] ATLAS Collaboration, *Search for Extra Dimensions using diphoton events in 7 TeV proton-proton collisions with the ATLAS detector*, Phys. Lett. **B710** (2012) 538–556.

[111] ATLAS Collaboration, *Search for high-mass dilepton resonances with 5 fb-1 of pp collisions at $\sqrt{s}$ = 7 TeV with the ATLAS experiment*, ATLAS-CONF-2012-007 (2012).

[112] CMS Collaboration, *Search for Resonances in the Dilepton Mass Distribution in pp Collisions at $\sqrt{s}$ = 7 TeV* , EXO-11-019 (2012).

[113] CDF Collaboration, *Search for New Dielectron Resonances and Randall-Sundrum Gravitons at the Collider Detector at Fermilab*, Phys. Rev. Lett. **107** (2011) 051801.

[114] CMS Collaboration, *Search for Signatures of Extra Dimensions in the Diphoton Mass Spectrum at the Large Hadron Collider*, Phys. Rev. Lett. **108** (2012) 111801.

[115] ATLAS Collaboration, *A Search for ttbar Resonances in the Dilepton Channel in 1.04/fb of pp Collisions at $\sqrt{s}$ = 7 TeV*, ATLAS-CONF-2011-123 (2011).

[116] ATLAS Collaboration, *Physics potential of Z' and W' searches with the ATLAS Detector as a function of the LHC center-of-mass energy*, ATL-PHYS-PUB-2011-002 (2011).

[117] CDF Collaboration, *Search for $Z' \to e^+e^-$ using dielectron mass and angular distribution*, Phys. Rev. Lett. **96** (2006) 211801.

[118] J. Alison et al., *Electron efficiency measurements using ATLAS 2010 data at $\sqrt{s} = 7$ TeV: Supporting note for the 2010 egamma paper*, ATL-COM-PHYS-2011-322, *unpublished* (2011).